ADVANCEMENT ON DESIGN AND CONTROL OF ELECTRIC MOTORS

LIU MING

PhD

The Hong Kong Polytechnic University

2020

The Hong Kong Polytechnic University

Department of Electrical Engineering

ADVANCEMENT ON DESIGN AND CONTROL OF ELECTRIC MOTORS

LIU MING

A thesis submitted in partial fulfilment of the requirements

for the degree of Doctor of Philosophy

December 2019

CERTIFICATE OF ORIGINALITY

I hereby declare that this thesis is my own work and that, to the best of my knowledge and belief, it reproduces no material previously published or written, nor material that has been accepted for the award of any other degree or diploma, except where due acknowledgement has been made in the text.

_____(Signed)

LIU MING (Name of student)

Abstract

Electric motors are electromagnetic devices to convert electrical energy into mechanical energy. The first electric motor was invented by William Sturgeon in 1832. Since then, electric motors have been playing an increasing important role in human society. Various sizes and types of electric motors have been developed and implemented in diverse applications, such as automotive, subway systems, dishwashers, computer printers, fans, refrigerators, pumps, machine tools and even toys. It is no doubt that electric motors have been one of the foundations of human daily life. It is still promising to continuously improve existing electric motors, and propose new ones by employing novel operation principles, to obtain better performance on power density, power factor and efficiency, etc.

As an effort to configure a new electric motor, this thesis firstly presents a novel magnetic resonant coupling motor (MRCM) constructed without any iron or permanent-magnet core, i.e. a novel coreless and magnetless electric motor. Different from the conventional operation principle of existing electric motors, the application of the wireless power transfer (WPT) system using magnetic resonant coupling (MRC) technology is the key feature of the proposed MRCM. By adjusting the excitation frequency in accordance with the trajectory of resonant frequency splitting, a large electromagnetic force in different direction can be developed. From the perspective of an elementary pole pair, the selection of resonant topology, the force magnitude and direction, and the frequency splitting phenomenon are analyzed elaborately, and the underlying operation principle is developed completely. Based on the proposed design procedures, computer simulations in MATLAB, PSIM and ANSYS Maxwell are presented to verify the feasibility of the proposed MRCM, and a control algorithm to regulate

torque ripple for the proposed MRCM is designed. Simulation results obtained so far are promising, and the proposed new design could well be a promising start for a new generation of future electric motor.

Meanwhile electric motors much rely on suitable and effective control algorithms to operate properly and robustly with satisfactory control performance. In recent decades, emerging faster and more sophisticated microprocessors, like TMS320F28335-based DSP controllers, enable the utilization of more precise and complicated control algorithms, to boost the control performance of electric motors. Among various electric motors, permanent magnet synchronous motors (PMSMs) are widely used due to its advantages of high efficiency, high torque density, and low volume. Better steady and dynamic responses on speed and torque control are always demanded for PMSMs, and various control algorithms for PMSMs have proposed over the years. With the chronological order, control algorithms for PMSMs have been developing from field oriented control (FOC), to direct torque control (DTC), and further to model predictive control (MPC). The existing control algorithms perform satisfactory steady and dynamic response on torque. However, the steady and dynamic response on speed are still requiring further enhancement.

By combining the advantages of MPC and direct speed control, model predictive direct speed control (MPDSC) is of great interest to realize an excellent speed control performance with satisfactory torque response. A single-vector-based MPDSC with compensation factors is thus devised in this thesis. An excellent speed tracking capability with very small speed offset and ripple is achieved by using the proposed single-vector-based MPDSC algorithm. Moreover, some compensation factors, such as torque suppression factor and stability factor, are proposed and integrated into the cost function to suppress large torque oscillations, and to improve the steady and dynamic state response. The simulation and hardware-in-the-loop (HIL) results confirmed that, compared to conventional DTC, model predictive torque control (MPTC) and FOC, the

proposed single-vector-based MPDSC strategy performs better control performance in terms of speed ripple, torque ripple, current THD.

To further enhance the speed response of MPDSC, more than one voltage vector can be used in every single control period, and a duty-ratio-based MPDSC with two cost functions for PMSM drives is therefore devised. To reduce the speed and torque ripples, one active vector and one zero vector are applied within every control period. More specifically, eight duty ratios are firstly deduced to form eight combinations of voltage vectors. Two cost functions acting sequentially are then employed to refine the combinations of voltage vectors. Three combinations of voltage vectors, which result in better dynamic torque response, are preselected from the first cost function. After that, the optimal combination of voltage vector is finally determined by the second cost function to minimize the steady-state offset and the ripple of rotor speed. The proposed duty-ratio-based MPDSC performs an overall superior performance than the single-vector-based MPDSC. The effectiveness of the proposed duty-ratio-based MPDSC has been well validated by both Simulink simulations and HIL tests.

Acknowledgements

First and foremost, I would like to express my heartfelt gratitude to my chief supervisor, Dr. Kevin K. W. Chan, for his trust, support and encouragement throughout my PhD study and research. He never gave up on me when I get stuck with my research. He tried his best to offer me financial and knowledge support to help me overcome life and research difficulties. To me, Dr. Chan is an admirable supervisor, but also a trustable and respectable friend. It is my great honor and fortune to conduct research as his student.

I also would like to give special thanks to Dr. Jiefeng Hu for his stimulating guidance on my research. He helped to extent my research scope. I have learnt a lot of valuable research skills from him. He gave me a lot of professional suggestions and constructive comments to my research.

Furthermore, I would like to appreciate critical comments from my paper reviewers and thesis examiners on my research. I also appreciate all staffs in the Department of Electrical Engineering for their assistances and support. I am grateful for the financial support from the Teaching Postgraduate Studentship Scheme and Research Studentship of The Hong Kong Polytechnic University to allow me to accomplish my Ph.D. study and academic research.

Moreover, I would like to express my unparalleled thanks to my dear parents Jinrong Gao and Xiaotong Liu. During the whole period of pursuing PhD degree, their encouragement and support have kept me moving forward. Without their unconditional and selfless love, I would never have been able to complete my PhD study.

Last but not least, I would like to show my special thanks to my fiancée, Zhuoxi LI, for her appearance in my life, and her spiritual support for the completeness of my PhD.

Table of Contents

Lists of Figures, Tables and Abbreviations

List of Figures

List of Tables

List of Abbreviations

ω_0 (or f_0)	Natural frequency
ω (or f)	Excitation frequency
Z	Impedance matrix.
L_1 *and* L_2	Inductances of the transmitter resonant circuit and receiver resonant circuit resp.
C_1 *and* C_2	Capacitances of the transmitter resonant circuit and receiver resonant circuit resp.
R_1 *and* R_2	Internal resistance of stator and rotor resonant circuit resp.
$\dot{I}_1$ *and* $\dot{I}_2$	Fundament current phasor of transmitter resonant circuit and receiver resonant circuit resp.
Z_1 *and* Z_2	Impedance of the transmitter resonant circuit and receiver resonant circuit resp.
M	Mutual inductance.
R_L	Equivalent resistance of the load.
δ	Phase difference between $\dot{I}_1$ and $\dot{I}_2$.
$\dot{U}$	Fundamental voltage phasor.
Z_{2S}	Impedance of receiver resonant circuit in series resonant topology.
k	Coupling coefficient.
γ	Attenuation coefficient.
k_c	Critical coupling coefficient.
f_L *and* f_H	Lower resonant splitting frequency and higher resonant splitting frequency resp.
φ	Phase difference φ between V and $\dot{I}_1$.
θ	Angular displacement.
$\boldsymbol{u}_s$	Voltage vector.

u_d, u_q	Stator voltage (d, q axis, resp.).
$\boldsymbol{\varphi}$	Stator flux vector.
φ_d, φ_q	Stator flux (d, q axis, resp.).
L_d, L_q	Stator inductance (d, q axis, resp.).
i_d, i_q	Stator current (d, q axis, resp.).
I_r	Rated current.
T	Electromagnetic torque.
p	Number of pole pairs.
R_s	Stator resistance.
ω	Rotor speed.
ω_r	Rated rotor speed.
φ_f	Permanent magnet flux.
J	Moment of inertia.
T_L	Load torque.
B_m	Vicious friction.
s_T	Slope of torque.
s_ω	Slope of rotor speed.
T_s	Sampling time.
U_{DC}	DC bus voltage.
T_r	Rated electromagnetic torque.
$\tilde{T}$	Estimated load torque.
v	Observer desired pole.

Chapter I

Introduction

1.1 Background and Literature Review

1.1.1 Machine Design and Wireless Power Transfer

Electric motors, which lay the foundation of the modern industry, have a wide range of applications in automotive, machine tools, fans, refrigerators, pumps, industrial equipment and even toys. The underlying principles of electric motor are the interaction between the magnetic field and electric current in windings. Various electric motors have been developed over the past century [1], such as induction motors (IMs) [2], permanent magnet synchronous motors (PMSMs) [3] and switched reluctance motors (SRMs) [4]. IMs take advantage of the electromagnetic induction to obtain the rotor current from the magnetic field of the stator winding. Iron cores are always utilized on stators or rotors to enhance the output torque as IMs without any iron cores would theoretically perform poorly due to the rather limited magnetic field density. For PMSMs, the usage of permanent magnets offers an independent magnetic field source. More advanced PMSMs have been continuously developing in the past decades, like doubly-salient PMSMs [5, 6], flux-reversal PMSMs [7] and flux-switching PMSMs [8]. The electromagnetic torque can be developed through the interaction of magnetic field generated by permanent magnets and the stator winding. However, permanent magnets are expensive and suffer from the demagnetization issue at high temperature [9]. Without permanent magnets and irons cores, PMSMs cannot work anymore. With regard to the SRMs, the stator windings are powered to generate the magnetic field. A force on rotor is created due to the magnetic reluctance, and no slip rings are required for SRMs. SRMs

have advantages including simple configuration, low cost and rigid design, However, the iron cores are necessary to develop the reluctance force, and torque ripple is relatively high owing to the variation of reluctance force [10].

Different from past research work on electric motors, an attempt using the wireless power transfer (WPT) principle to configure an electric motor without any iron core or permanent magnet is proposed in this thesis. The main application of WPT is to transfer power in stationary state. Due to the merits like space-saving, convenient, reliable and safe, WPT has become a promising alternative to the conventional cable-based power delivery scheme [11-13]. Nikola Tesla initially proposed the concept of WPT, and employed the magnetic resonant coupling (MRC) technology in WPT in the early 20^{th} century [14]. Since Kurs et al. presented a mid-range WPT in 2007 [15], the WPT system using the MRC technology has drawn much attention in recent research. On-going research hotspots of WPT can be concluded as advance control methods [16, 17], compensation schemes/topologies [18, 19], efficiency improvement [20-22], power capacity enhancement [23, 24], and data transmission methods [25, 26]. A large number of researchers have devoted themselves to study and improve the WPT system using MRC technology for different applications, such as biomedical implants [27-29], mining applications [30], underwater applications [31], and electric vehicles (EVs) [13, 32, 33]. For these research hotspots and applications, WPT method is employed to perform the task of power delivery, in which the transferred power is mainly to charge batteries.

For a safe and effective battery charging, the charging state should be able to change from constant current (CC) to constant voltage (CV) depending on the state of charge (SOC) of the battery. Besides, different SOC of battery corresponds to different equivalent resistance of the battery. Consequently, it is necessary to develop a load-independent WPT system with the capability of CC and CV charging, and many methods have been proposed [34-38]. By varying the operation frequency, it is effective to obtain both CC and CV outputs [34].

However, the frequency splitting phenomenon in frequency control may result in an unstable WPT system [39]. By using a constant operating frequency, [35] presents a load-independent WPT system with CV output, but this WPT system cannot operate at CC charging state. A load-independent WPT system with CC and CV outputs can be achieved through the adjustment of series to parallel compensation at the transmitter side [36, 37]. These schemes require more inductors, capacitors and switches, and hence increase the manufactory cost and installation space. A reconfigurable intermediate resonant circuit is employed in [38] to configure a load-independent WPT system with CC and CV outputs. Less components are required in the proposed WPT system. However, there are essential requirements on fixed values of mutual inductances and self-inductances. More advanced topology or control methods would be proposed to develop compact and robust load-independent WPT system with CC and CV outputs.

In a WPT system, frequency splitting phenomenon happens when the transmitter and receiver are in strong coupling condition. A great deal of research work has been conducted to investigate the frequency splitting phenomenon ranging from two-coil WPT system [40, 41], to three-coil WPT system [42], and further to four-coil WPT system [43, 44]. The frequency splitting phenomenon concerns the frequency characteristics of transfer power, while the maximum system efficiency is always at the natural resonant frequency. Most studies of frequency splitting phenomenon refer to the perspective of transferring power. Some researchers employ the frequency tracking methodology, in which the excitation frequency is varying with different coupling coefficient, to maintain the optimal power transfer [45, 46]. Other researchers have also proposed frequency splitting suppression methods, such as adjusting the load resistor [47] and using non-identical resonant coils [48], to obtain uniform power on the receiver side.

Nevertheless, the frequency splitting phenomenon can be utilized on some particular applications. For instance, a near field inductive multiple-input and multiple-output (MIMO) communication scheme has been developed by manipulating the frequency splitting phenomenon [49]. A high-performance power and information transfer is realized by using splitting frequencies [50]. Three coils at the transmitter side, which operate at frequency splitting state, are configured to offer independent power transfer for three robots in [51]. Besides above applications, when frequency splitting phenomenon happens, the characteristic of phase angle could be utilized to develop an innovative electric motor, which is referred as the first contribution of this thesis. More detailed descriptions and analysis about wireless power transfer will be presented in Chapter II and III.

1.1.2 Machine Control

In last few decades, servo drive has found a wide variety of applications in industry. Servo drives require high performance in terms of accuracy and dynamics, especially on torque and speed control. A great deal of on-going research concerns the motor structure optimization and control methods. Among different motor types, the permanent magnetic synchronous motors (PMSMs) have been widely used in electric drives due to their merits including high torque-to-inertia ratio, high power density and high efficiency. For a large variety of applications, suitable control schemes are highly desired to meet different operating conditions for PMSM drives.

To enhance the control performance, not limiting to the reduction of torque and stator flux ripples, one simple and straightforward method is to increase the sampling frequency, and in other words, to decrease the control period. For the same control algorithm, the control performance with smaller control period is usually better owing to the increased switching frequency. However, it should be ensured that there is a sufficient time to completely execute the control algorithm,

and therefore the sampling frequency cannot be increased unrestrictedly. With the same control period length, advanced control algorithms contributes to better control performance. Various advanced control methods have been continuously proposed over the past decades. With the chronological order, the most popular control methods are field-oriented control (FOC), direct torque control (DTC), and model predictive control (MPC).

FOC is one of the most popular control methods over the past decades [52]. Up to now, many engineers prefer to improve and use FOC in various types of electric motors [53-55]. In a typical double-loop structure based FOC scheme, the outer speed loop determines the speed and torque response, while the inner current loop influences the dynamic and steady performance of the whole drive system. However, several interactive PI adaptors have to be tuned carefully to achieve a satisfactory control performance. Moreover, cascaded linear controllers in FOC have a limited bandwidth to avoid large overshoots, leading to slow dynamics.

In order to improve the dynamics, DTC was proposed by Takahashi and Noguchi [56] and Depenbrock [57]. The key component of DTC is a user switching table, which is developed with the consideration of the variation of the torque slop and the flux slop. The main difference between FOC and DTC is the way to select or develop the voltage vector. FOC develops the desired voltage vector through several PI adaptors, while DTC selects a voltage vector from a predefined switching table. Compared to FOC, DTC has merits including simplicity, robustness and fast dynamic response [58], due to the simple mechanism that DTC selects the suitable voltage vector from the pre-defined switching table directly without using cascade structure and complicated coordinate transformation [59, 60]. Nevertheless, it is widely acknowledged that the conventional DTC presents the drawbacks of high ripples on torque and stator flux.

To tackle existing problems in conventional DTC, numerous improved DTC strategies have been developed. Conventional space vector modulation (SVM) was adopted in DTC to manipulate the stator flux and torque more moderately [61, 62]. SVM-DTC can synthesize an arbitrary desired voltage vector by using two active voltage vectors and one zero voltage vector, rather than selecting one from a pre-defined switching table consisting of limited number of voltage vectors. For SVM-DTC, it is essential to determine the suitable commanding voltage vector, and possible criterions have been presented like indirect torque control [63, 64], deadbeat control [65, 66], stator flux-oriented control [67], and sliding mode control [68, 69]. By employing SVM-DTC, lower ripples on stator flux and torque can be obtained. However, coordinate transformation, accurate machine parameters and powerful digital controllers are required to achieve a robust and decent control performance.

Besides the use of SVM, it is widely accepted that the steady state performance of conventional DTC can be enhanced by inserting more voltage vectors in one control period, i.e. duty ratio modulation (DRM). In references [70-74] , one active voltage vector and one zero voltage vector are applied in one control cycle. Specifically, an optimal active voltage vector is firstly selected from the switching table, and the zero voltage vector is then inserted into the same control cycle with a duty ratio. The duty ratio can be calculated by certain criterions, such as deadbeat control [74], direct mean torque control [75, 76], minimized torque ripple [72, 73, 77], considering both torque and flux error [78-80] and fuzzy logic adaptation [81]. [78] presents a new DTC with a unified switching table, and each control period will apply two active voltage vectors and one zero voltage vector. The method in [71] will be adopted later on in this thesis to calculate the duration of the zero voltage vector. Although the proposed method in [78] is effective to reduce ripples on stator flux and torque, it is rather complicated with heavy computational burden.

To sum up, conventional DTC is a popular and effective machine control method, while it has intrinsic drawback of high torque ripple. In this thesis, conventional DTC is regarded as a benchmark for the comparison to proposed control methods. In subsection 2.2.2, detailed discuss and analysis of conventional DTC are presented, with simulation results obtained from MATLAB Simulink.

In recent years, several modern control algorithms, like fuzzy logic control [82, 83], artificial neural network [84, 85], sliding mode control [86-89] and MPC [90-96], have been proposed and applied in the area of power electronics and electric drives to improve the control performance. Among these control methods, MPC, which was initially designed to control the power converters [97], has attracted significant attention worldwide. With several years of rapid development, MPC has penetrated into many research fields. Two popular research orientations are grid-connected converters [98-100] and machine drives [98-124].

MPC is intrinsically capable to handle different control objectives with nonlinearity, multiple constraints and multiple variables. By considering the inherent discrete nature of power converter, the influence of each possible voltage vector on the concerned variables is firstly predicted. The optimal voltage vector is then selected by minimizing a user-defined cost function, which is usually formulated with the differences between the controlled variables and their references. Various MPC-based methods have been reported in recent years, such as model predictive torque control (MPTC), model predictive current control (MPCC). The underlying operating principles of different MPC strategies are similar, but with various cost functions.

MPTC employs electromagnetic torque and stator flux to constitute the cost function [101-107]. Owing to the different magnitudes and units of electromagnetic torque and stator flux, a well-tuned weighting factor is essential to achieve a satisfactory control performance. A possible method to select the

weighting factor is based on the normalization of electromagnetic torque and flux [108]. Other methods, such as multi-objective genetic algorithm [109], and flux-dependent method [110], can be employed to deduce the optimal weighting factor. To eliminate the time-consuming and annoying tuning process, some MPTCs without the involvement of weighting factor are proposed [111-116]. [111] evaluates the electromagnetic torque and stator flux separately, and select the optimal voltage vector based on a ranking approach. A voltage vector is derived to replace the electromagnetic torque and stator flux in [112] to eliminate the weighting factor. In [114-116], the torque and stator flux are converted to an equivalent vector of the stator flux to avoid the use of weighting factor. As only the stator flux is required to be regulated in the cost function, this method can be classified as model predictive flux control (MPFC). With a suitable weighting factor, MTPC can achieve a good control performance on torque. However, since the main control objective of MPTC is to regulate torque rather than speed while the speed is indirectly controlled through a PI adapter, speed control performance is inferior with large speed ripple and offset. More detailed illustration and analysis of MPTC will be presented in subsection 2.2.3.

Drawing on the notion of FOC, MPCC merely uses the d,q-axis or α, β-axis stator current to develop the cost function [94, 117-121]. Compared to MPTC, which requires the tuning of weighting factor, and the estimation or measurement of electromagnetic torque and flux, MPCC is much simpler since the control variables (d,q-axis or α, β-axis stator currents) can be directly measured through current sensors. In particular, a predicted current locus is used as reference frame in MPCC to select the optimal voltage vector [120]. Nevertheless, MPCC can be regarded as a special application.

DRM has been successfully employed in DTC to reduce the torque ripple. Enlightened by such practice, it is also effective to use DRM in MPC to enhance the control performance. It is not restricted to use one nonzero voltage vector and one zero voltage vector during one control period [94, 122, 123]. It is possible to

use two nonzero voltage vectors during one control period when the machine operates at high speed [124], and even to use two nonzero voltage vectors and one zero voltage vector during one control period [125]. Compared to FOC and DTC, MPC intrinsically has heavy computation burden. If a long prediction horizon is implemented to compensate the one step delay, and more voltage vectors in one control period are used in one control period, it is inevitable to increase the control complexity significantly, which poses a challenge to the computational capability of digital controllers.

Conventional MPC is based on the accurate system model to predict the future performance, and to select the optimal voltage vector through the cost function. Due to the different operating conditions of PMSM, such as temperature variation, and wear and tear, machine parameters will change, like the perturbation of resistance and inductance, as well as the demagnetization of permanent magnet. It is necessary to enhance the robustness against the parameter variations. Possible solutions include the compensation the errors resulting from the inaccurate parameters, the estimation of machine parameters, or the elimination of the usage of machine parameters. An observer is used in [126] to compensate the errors resulting from the inaccurate parameters, and a compensated voltage value is applied to PMSM through SVM. Besides, [118] adopts the manipulation of current equations to eliminate the usage of flux linkage. Besides, a sliding-mode disturbance observer is developed to compensate the inductance disturbances. It can be summarized that, the employment of observers is a widely accepted method to enhance the robustness against parameter variations. However, some parameters have to be included to develop the observer model, which may bring some parameter observation errors. Besides, the observer gain and poles should be carefully designed and assigned to guarantee the stability.

1.2 Incentives of Thesis

Electric motors are the essential element to constitute the electric devices of the modern industry and daily living. The existing electric motor, i.e. IMs, PMSMs and SRMs, have their own intrinsic disadvantages, such as heavy, frequent maintenance, expensive permanent magnet materials and large torque ripple. In a WPT system with strong-coupling state, frequency splitting phenomenon happens, and the characteristic of phase angle could be utilized to develop an innovative electric motor. Drawing on the characteristic of WPT system using MRC technology, the first objective of this thesis is to configure an electric motor without any iron core or permanent magnet, named magnetic resonant coupling motor (MRCM).

Different from paper [127], where an electric motor is powered by WPT system using MRC technology, the proposed MRCM would develop the output torque by the WPT system using MRC technology, in which the frequency splitting phenomenon would not be suppressed, but be utilized. The specific application of WPT system using MRC technology in rotating state has been reported in [128-132], but these applications do not concern the force generation in electric motors. By manipulating the phase characteristics of frequency splitting phenomenon, large torque in different direction is achievable through the manipulation of excitation frequency. The underlying operation principle of the proposed electric motor is based on the frequency splitting phenomenon. The stator and rotor are wounded by closed loop windings, and resonant capacitors are installed to configure stator and rotor resonant circuits. When two resonant circuits are under strong coupling region, the frequency splitting phenomenon happens. By manipulating the phase characteristics of frequency splitting phenomenon, large torque in different direction is achievable through the manipulation of excitation frequency. The proposed MRCM is a promising start for a new generation of future electric motor.

With various types of electric motors, suitable and effective control methods are required to meet different operation conditions and achieve satisfactory control performance. Control methods have been developing for several decades, and the developing route can be simply concluded as: from FOC, to DTC, and to MPC. MPC is the most popular research hotspot in recent years, and a large number of MPC-related control algorithms have been published, like MPTC [101-107] and MPCC [94, 117, 118]. Most MPC strategies proposed in previous papers focus either on current or torque/flux control, in which a cascade speed loop is required. Most existing MPC methods consist of a cascaded speed-to-torque loop [133-135] or speed-to-current loop [118, 136, 137], where a proportional-integral (PI) is usually included as a linear adapter. However, as PMSM system is a typical nonlinear system, MPC with PI may result in a compromised control performance. Specifically, improper PI parameters in speed loop would contribute to inferior control performance, such as large speed offset, high ripples of speed and torque. Complicated and time-consuming tuning methods are therefore required to achieve satisfactory performance. In this thesis, model predictive direct speed control (MPDSC) is proposed to deal with above issues, performing better speed response.

MPDSC integrates the merits of MPC and direct speed control, and overcomes the limitations of cascaded loops to achieve high control dynamics in speed. However, only limited work in this field has been reported so far. In [138], the MPDSC controller predicts the future current and speed in discrete steps. It selects the plant inputs which mainly depend on the predicted speed error, but large fluctuations in stator flux and torque in both transient and steady-state would in turn influence the speed performance. More recently, an improved MPDSC using state-dependent Riccati equation by explicit constraints on the current and the field-weakening curve was proposed [139]. However, it fails to tightly regulate the torque. In addition, it is complicated to tune the PI controller for matching the load response, and PI controller generates larger overshoots on

the speed. A MPDSC with short prediction horizon was developed in [140]. It eliminates the PI controller, but stability issues arise. A proper weighting for balancing the speed error and current error is involved in the cost function to improve the system behavior. Nevertheless, the torque ripple is not considered in this control strategy.

The second objective of this thesis is thus to devise a single-vector-based model predictive speed control (MPDSC). The proposed single-vector-based MPDSC strategy is a PI-free control strategy, and has a superior speed tracking capability with very small speed offset. Besides, the torque ripple is regulated and minimized effectively by introducing compensation factors.

A simple but effective method to enhance the control performance is to employ DRM method, where a zero voltage vector will be used together with the selected active voltage vector in a sampling period. When more than one voltage vector is applied in one sampling period, it is crucial to select an appropriate duty ratio. Otherwise, the system performance will be compromised. Many methods have been proposed to determine the duty ratio [72-81, 141-147]. Therein, deadbeat control is extensively employed to calculate the duty ratio [112, 119, 143, 147]. Specifically, the duty ratio is calculated by the deadbeat criterion after the selection of the optimal voltage vector. Nevertheless, such step-by-step calculation cannot obtain the optimal duty ratio to combine the zero and active voltage vectors. Improved approaches are still required to achieve the maximum benefit of DRM.

Moreover, there is only one cost function in existing MPC methods, which is integrated by a few control variables, like toque and flux for model predictive torque control (MPTC) [113, 148]. However, a weighting factor is essential to cope with the problem that control variables have different magnitude. With an improper weighting factor, the tacking performance of electromagnetic torque is quite unsatisfactory. Two cost functions can be employed to address this issue. [111] uses two individual cost function to choose two optimal voltage vectors for

torque and flux control respectively from eight voltage vectors. The optimal voltage vector is determined based on the average ranking approach. Moreover, an MPC method in [149] uses one cost function for the torque to preselect two voltage vectors, and uses a separate cost function for the flux to select the optimal voltage vector from the preselected two voltage vectors. Such cascaded two cost functions contribute to a very fast dynamic behavior. Although two cost functions are involved, only one voltage vector is applied in a control period, and the torque ripple is still very high.

Therefore, the third objective of this thesis is to develop the duty-ratio-based MPDSC with two cost functions. The proposed duty-ratio-based MPDSC is also a PI free approach, which contributes to achieve better control dynamics in speed. To fulfill an optimal DRM, eight duty ratios are first deduced by the criterion of deadbeat speed control to form eight combinations of voltage vectors. Then, the optimal combination of voltage vector is selected using two cascaded cost functions acting sequentially. The proposed duty-ratio-based MPDSC strategy can minimize speed and torque ripple significantly, and the speed offset is extremely small. The control performance of duty-ratio-based MPDSC is rather better than the single-vector-based MPDSC.

1.3 Primary Contribution

This thesis presents the advancement on design and control of electric motors. More specifically, the primary contributions include MRCM, single-vector-based MPDSC and duty-ratio-based MPDSC, which are summarized as follows.

Foremost, a novel electric motor, i.e., MRCM, is proposed. MRCM is a new design concept, which could well be a promising start for a new generation of future electric motor. The application of the WPT system using MRC technology is the key feature of the proposed MRCM. The basic operation principle of the proposed MPCM is introduced based an elementary pole pair. The magnitude

and direction of the force in a pole pair, frequency splitting phenomenon, and the trajectory of resonant splitting frequency are studied to present an in-depth investigation of the proposed MRCM. Using MAXWELL, PSIM and ANSYS Maxwell, the effectiveness is validated by numerical simulation results and comparisons with conventional electric motors.

Secondly, a single-vector-based MPDSC with compensation factors is proposed for PMSM drives. As improper PI parameters in speed loop of conventional DTC and MPTC would result in inferior control performance, such as high ripples of speed and torque and large speed offset, no PI unit is included in the proposed single-vector-based MPDSC. To design a robust control, a torque suppression factor is introduced to limit the torque to be smaller than the rated value. Besides, stability factors are employed to deal with the issue of myopic prediction. While the steady and transient response of speed is quite satisfactory with the speed and flux control in the cost function, the dynamic response of speed is better than the conventional DTC and MPDSC, where the speed can reach the reference value with a rather smaller offset in a very short time. The superior control performance of the proposed MPDSC is validated by numerical simulations with comparisons to conventional DTC, MPDSC and FOC, and by HIL test.

Thirdly, a duty-ratio-based MPDSC with two cost functions is proposed for PMSM drives. This is a continuous work for the single-vector-based MPDSC. The proposed duty-ratio-based MPDSC is also a PI-free control algorithm. In this MPDSC, duty ratios are involved to further enhance the control performance. With the consideration of the speed slop at $(k+2)th$ time instant, eight duty ratios, which corresponds to eight voltage vectors, are deduced by deadbeat speed criterion to develop eight combinations of voltage vectors. Two cost functions will then refine these eight combinations of voltage vectors sequentially, where the first cost function is to conduct torque control, and the second cost function is to realize speed and flux control. The effectiveness of the

proposed duty-ratio-based MPDSC is affirmed by numerical simulations and HIL test with a better control performance than the single-vector-based MPDSC.

1.4 Thesis Layout

Four chapters constitute the rest of this thesis. Chapter II shows the basic knowledge on machine design and control. Chapter III proposes MRCM with elaborate analysis and validations. Chapter IV presents the single-vector-based MPDSC with compensation factors. Chapter V investigates the duty-ratio-based finite-control-set MPDSC with two cost functions. Finally, the conclusions of the thesis are drawn with suggestions on the future work in Chapter VI.

1.5 List of Publications

Transaction Papers

1. **M. Liu**, K. W. Chan, J. Hu, Q. Lin, J. Liu, and W. Xu, "Design and realization of a coreless and magnetless electric motor using magnetic resonant coupling technology," *IEEE Trans. Energy Convers.*, vol. 34, no. 3, pp. 1200-1212, Sep 2019. DOI: 10.1109/TEC.2019.2894865
2. **M. Liu**, K. W. Chan, J. Hu, W. Xu, and J. Rodriguez, "Model predictive direct speed control with torque oscillation reduction for PMSM drives," *IEEE Trans. Ind. Informat.*, vol. 15, no. 9, pp. 4944-4956, Sep 2019. DOI: 10.1109/TII.2019.2898004
3. **M. Liu**, K. W. Chan, J. Hu, "Dual Cost Function Model Predictive Direct Speed Control with Duty Ratio Optimization for PMSM Drives," submitted to *IEEE Trans. Energy Convers.*, Jan. 2020, under review.
4. W. Xu, **M. Liu**, J. Liu, K. W. Chan, and K. W. E. Cheng, "A Series of New Control Methods for Single-phase Z-source Inverters and the Optimized Operation," IEEE Access, vol. 7, pp. 113786-113800, Aug 2019. DOI: 10.1109/ACCESS.2019.2935023
5. Y. Li, J. Hu, **M. Liu**, Y. Chen, K. W. Chan, Z. He, et al., "Reconfigurable intermediate resonant circuit based WPT system with load-independent constant output current and voltage for charging battery," *IEEE Trans. Power Electron.*, vol. 34, no. 3, pp. 1988-1992, Mar 2019. DOI: 10.1109/TPEL.2018.2858566
6. Y. Shan, J. Hu, **M. Liu**, J. Zhu, and J. M. Guerrero, "Model predictive voltage and power control of islanded PV-battery microgrids with washout filter based power sharing strategy," *IEEE Trans. Power Electron.*, vol. 35, no. 2, pp. 1227-1238, Feb. 2020. DOI: 10.1109/TPEL.2019.2930182

7. J. Liu, W. Xu, K. W. Chan, **M. Liu**, X. Zhang, and N. H. L. Chan, "A three-phase single-stage AC-DC wireless-power-transfer converter with power factor correction and bus voltage control," *IEEE Trans. Emerg. Sel. Topics Power Electron.*, Early Access, May 2019. DOI: 10.1109/JESTPE. 2019.2916258
8. X. Zhang, P. Li, J. Hu, **M. Liu**, G. Wang, J. Qiu, et al., "Yen's Algorithm Based Charging Facility Planning Considering Congestion in Coupled Transportation and Power Systems," IEEE Trans. Transport. Electrific., Early Access, Dec. 2019. DOI: 10.1109/TTE.2019.2959716.
9. J. Liu, K. W. Chan, C. Y. Chung, N. H. L. Chan, **M. Liu**, and W. Xu, "Single-stage wireless-power-transfer resonant converter with boost bridgeless power-factor-correction rectifier," *IEEE Trans. Ind. Electron.*, vol. 65, no. 3, pp. 2145-2155, Mar 2018. DOI: 10.1109/TIE.2017.2745471
10. X. Li, J. Hu, Y. Li, H. Wang, **M. Liu**, and P. Deng, "A decoupled power and data parallel transmission method with four-quadrant misalignment tolerance for wireless power transfer systems," *IEEE Trans. Power Electron.*, vol. 34, no. 12, Dec 2019. DOI: 10.1109/TPEL.2019.2920441
11. Y. Li, J. Hu, X. Li, R. Mai, Z. Li, **M. Liu**, et al., "Efficiency analysis and optimization control for input-parallel output-series wireless power transfer systems," *IEEE Trans. Power Electron.*, vol. 35, no. 1, Jan 2020. DOI: 10.1109/TPEL.2019.2914299

Conference papers

12. **M. Liu**, J. Hu, and K. W. Chan, "Improved model predictive control of permanent magnet synchronous motor with duty ratio optimization and cost function correction," in *Int. Conf. Electr. Mach. Syst. (ICEMS)*, Oct. 2017, pp. 1-5.

13. Y. Shan, J. Hu, K. W. Cheng, and **M. Liu**, "A universal model predictive control for practical AC microgrids with PVs and battery energy storage systems," in *IEEE Energy Conversion Congress & Expo(ECCE)*, 2018, pp. 6257-6262.
14. Y. Li, J. Hu, K. W. Chan, K. W. E. Cheng, and **M. Liu**, "A flexible load-independent multi-output wireless power transfer system based on double-t resonant circuit technique," in *IEEE Energy Conversion Congress & Expo(ECCE)*, 2018, pp. 3593-3596.

Chapter II

Basic Knowledge on Machine Design and Control

2.1 Machine Design and Wireless Power Transfer

In this section, the resonant topology is investigated with the consideration of the phase characteristic, which makes it possible to configure a promising electric motor.

Recently, most research literatures are focused to enhance the performance of existing electric motors, like torque/power density, fault tolerance and torque ripple. For example, electric motors designed with more phases can enhance not only the torque/power density for PMSM [150, 151], but also the fault tolerance [152, 153]. To enhance demagnetization withstand capability and flux-weakening ability of conventional PMSMs, a spoke-type hybrid permanent magnet brushless motor has been designed for electric vehicles (EVs) [154]. Some enhanced switched reluctance motors are presented in [155-157] to reduce the torque ripple and increase the torque density. A dual-rotor electric motor, consisting of a PM-type outer rotor and a cage-type inner rotor, is presented in [158] as a possible direction to improve the overall performance of electric motors.

For rotary applications, the employment of WPT system is a promising solution to provide safe and reliable power transfer with low maintenance. Some rotary WPT systems have been developed in [128-132] to avoid the use of mechanical slip-rings. These papers have investigated and enhanced the power transfer capability for single phase and three phase applications. However, these applications do not concern the force generation in electric motors.

2.1.1 Resonant topology of Wireless Power Transfer

The magnetic resonant coupling WPT system was initially published in *Science* and analyzed using coupled mode theory by Kurs *etc.* in 2007 [159] . His team realized a 60 watts power transfer with ~40% efficiency over distances over 2 meters. After his inspiring study, a large number of researches sprang up. In this subsection, the four resonant topologies for two-resonant-circuit WPT system are introduced and formulated.

For the convenience of analysis, there are the notations and assumptions of the magnetic resonant coupling WPT system. From now on, suffix '1' means the parameters in the transmitter coil and suffix '2' means the parameters in the receiver coil. Coil inductance of transmitter coil and receiver coil are expressed as L_1 and L_2 respectively. Similarly, capacitances are expressed as C_1 and C_2, respectively.

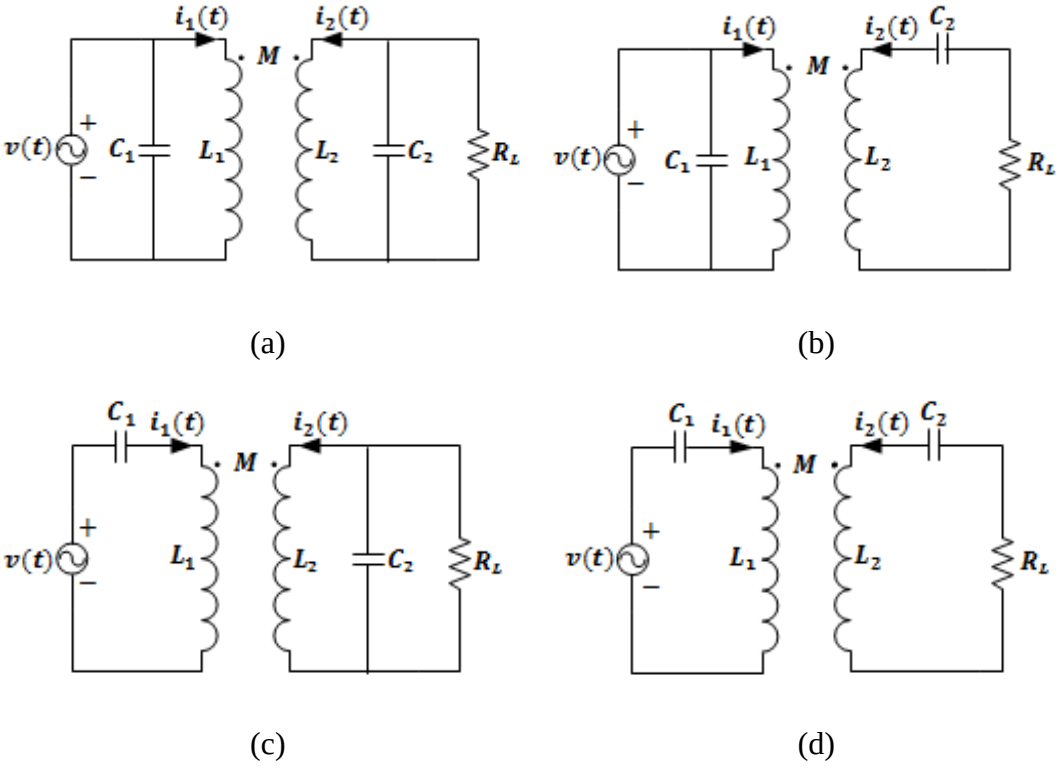

Fig. 2.1. Resonant topologies for two-resonant-circuit WPT system. (a) parallel-parallel (PP) resonant topology. (b) parallel-series (PS) resonant topology. (c) series-parallel (SP) resonant topology. (d) series-series (SS) resonant topology.

Considering two-resonant-circuit WPT system with one transmitter resonant circuit and one receiver resonant circuit, each resonant circuit could be either in series *LC* resonant topology or parallel *LC* resonant topology. Neglecting internal resistances, four different *LC* resonant topologies are depicted in Fig. 2.1, where i_1(t) and i_2(t) are the current flowing in the transmitter and receiver coil respectively.

To transfer power efficiently, transmitter resonant circuit and receiver resonant circuit are tuned to be resonant at a same natural frequency ω_0 (or f_0), which merely depends on the inductance *L* and capacitance *C*,

$$\omega_0 = \frac{1}{\sqrt{LC}} \tag{2.1}$$

$$f_0 = \frac{\omega_0}{2\pi} = \frac{1}{2\pi\sqrt{LC}} \tag{2.2}$$

Using a general expression, the equivalent equation for four resonant topologies can be written as:

$$Z\begin{bmatrix}\dot{I}_1\\ \dot{I}_2\end{bmatrix} = \begin{bmatrix}V\\ 0\end{bmatrix} \tag{2.3}$$

where $\dot{I}_1$ and $\dot{I}_2$ are the fundament current phasor of transmitter resonant circuit and receiver resonant circuit respectively. *V* is the RMS (Root Mean Square) value of the input sin-wave voltage. *Z* is the impedance matrix, which has four different forms (2.4)-(2.7) corresponding to four resonant topologies as are shown in Fig. 2.1. (a), (b), (c) and (d).

$$Z_{PP} = \begin{bmatrix}j\omega L_1 & j\omega M\\ j\omega M & j\omega L_2 + R_L\end{bmatrix} \tag{2.4}$$

$$Z_{PS} = \begin{bmatrix}j\omega L_1 & j\omega M\\ j\omega M & j\omega L_2 + \dfrac{1}{j\omega C_2} + R_L\end{bmatrix} \tag{2.5}$$

$$Z_{SP} = \begin{bmatrix}j\omega L_1 + \dfrac{1}{j\omega C_1} & j\omega M\\ j\omega M & j\omega L_2 + R_L\end{bmatrix} \tag{2.6}$$

$$Z_{SS} = \begin{bmatrix}j\omega L_1 + \dfrac{1}{j\omega C_1} & j\omega M\\ j\omega M & j\omega L_2 + \dfrac{1}{j\omega C_2} + R_L\end{bmatrix} \tag{2.7}$$

where R_L are the equivalent resistance of the load. L_1 and L_2 are the inductances of the transmitter resonant circuit and receiver resonant circuit respective. C_1 and C_2 are the capacitances of the transmitter resonant circuit and receiver resonant circuit respective. ω is the excitation frequency in rad/s. M is the mutual inductance which represents the interlink degree of the magnetic field between the transmitter resonant circuit and receiver resonant circuit. Based on the general analysis presented above, an investigation on resonant topology is conducted in next subsection.

2.1.2 Investigation on Resonant Topology

The generalized equivalent circuits at the transmitter side and receiver side are depicted in Fig. 2.2.

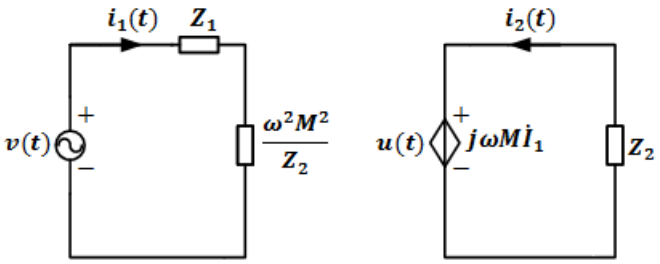

(a) (b)

Fig. 2.2. Equivalent circuits. (a) at transmitter side. (b) at receiver side.

Using the equivalent circuit as is shown in Fig. 2.2 (a), the fundamental current phasor can be derived as:

$$\dot{I}_1 = \frac{V}{Z_1 + \frac{\omega^2 M^2}{Z_2}} \tag{2.8}$$

The magnitude of $\dot{I}_1$ is not only determined by the transmitter impedance Z_1, but the reflected impedance $\frac{\omega^2 M^2}{Z_2}$.

At the receiver side as is shown in Fig. 2.2 (b), the fundamental voltage phasor $\dot{U}$ of the controlled voltage source is

$$\dot{U} = j\omega M\dot{I}_1 \tag{2.9}$$

Comparing the expressions of $\dot{U}$ and $\dot{I}_1$, there is a complex angle j which indicates that the phase difference between $\dot{U}$ and $\dot{I}_1$ is 90° ($\dot{U}$ is 90° ahead of $\dot{I}_1$). In other words, the phase difference between $\dot{U}$ and $\dot{I}_1$ is independent of the resonant topology of transmitter resonant circuit. At the transmitter side, both series and parallel resonant topologies always result in a 90° phase difference between $\dot{U}$ and $\dot{I}_1$.

The fundamental phasor current $\dot{I}_2$ at the receiver side is derived as

$$\dot{I}_2 = \frac{\dot{U}}{Z_2} \tag{2.10}$$

The phase angle of $\dot{I}_2$ is determined by Z_2. Assuming no resistance in Z_2, an inductive Z_2 indicates that $\dot{I}_2$ is 90° ahead of $\dot{U}$, while a capacitive Z_2 indicates that $\dot{I}_2$ lags 90° behind of $\dot{U}$. As the phase difference between $\dot{U}$ and $\dot{I}_1$is always 90°, the former case results in that the phase difference δ between $\dot{I}_1$ and $\dot{I}_2$ is 180°, while the latter case results in that the phase difference δ between $\dot{I}_1$ and $\dot{I}_2$ is 0°. To sum up, the inductive or capacitive characteristic of Z_2 determines the phase difference δ between $\dot{I}_1$ and $\dot{I}_2$, but the transmitter side has no effect on the phase difference δ between $\dot{I}_1$ and $\dot{I}_2$.

The proposed MRCM would be composed of many paired transmitter and receiver resonant circuits, and the force is generated by the paired resonant circuits. Based on Ampere's Law, if the direction of the current flowing in two current carrying wires is the same, two wires attracts each other; on the contrary, if the direction of the current flowing in two current carrying wires is opposite, two wires repels each other. Hence, when transmitter and receiver resonant circuits have the same corresponding terminals to define the current direction, an attraction force would be generated when phase difference δ between $\dot{I}_1$ and $\dot{I}_2$ is 0°, while an repulsion force would be generated when phase difference δ between $\dot{I}_1$ and $\dot{I}_2$ is 180°. It is preferable to select a suitable resonant topology to develop both attraction force and repulsion force to enhance the capability of force generation.

Fig. 2.3 shows the simulation results of the phase difference δ between $\dot{I}_1$ and $\dot{I}_2$ for different excitation frequency for four resonant topologies. In Fig. 2.3 (a), P-P and S-P resonant topologies present a consistent 0° phase difference δ for different excitation frequency, which means that parallel resonant topology of the receiver resonant circuit always presents a Z_2 in capacitive characteristic irrespective of the different excitation frequency. For P-S and S-S resonant topologies, Fig. 2.3 (b) demonstrates that both 0° and 180° phase difference δ between $\dot{I}_1$ and $\dot{I}_2$ are achievable. For the receiver resonant circuit in series resonant topology, the impedance Z_{2S} is

$$Z_{2S} = j\omega L_2 + \frac{1}{j\omega C_2} \tag{2.11}$$

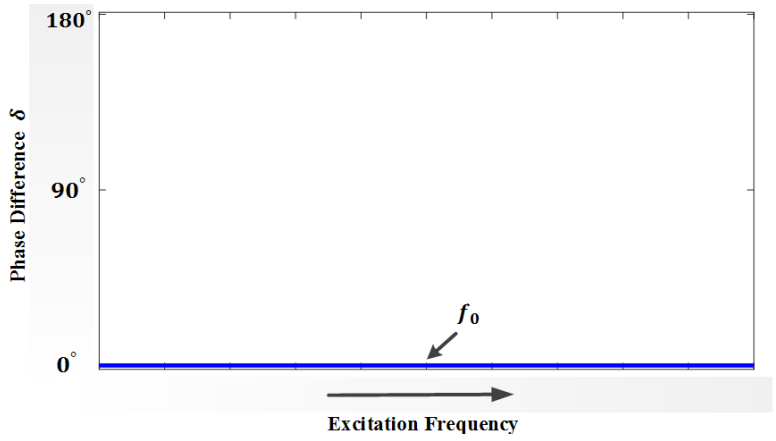

(a)

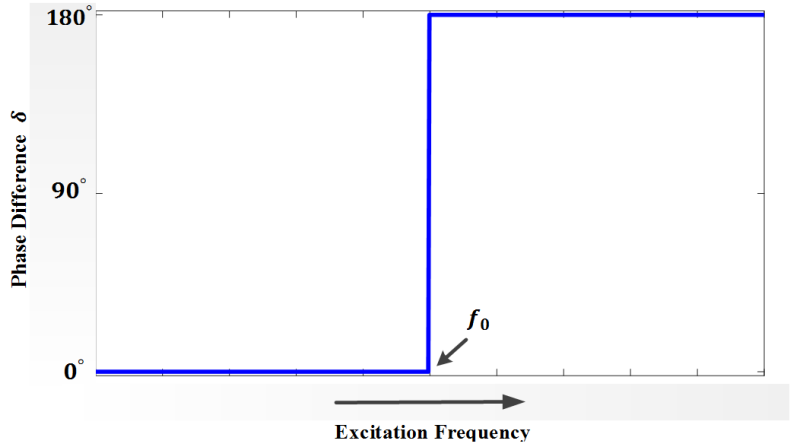

(b)

Fig. 2.3. Phase difference δ between $\dot{I}_1$ and $\dot{I}_2$ for different excitation frequency. (a) P-P and S-P resonant topologies. (b) P-S and S-S resonant topologies.

As both inductive Z_{2S} (when $f > f_0$) and capacitive Z_{2S} (when $f < f_0$) are achievable, receiver resonant circuit in series resonant topology is selected to generate both repulsion force and attraction force.

Regarding to the topology in transmitter side, the series resonant topology presents the minimum impedance value when the circuit is in resonant state, and a large current would be developed. When the receiver side is of series resonant topology, the reflected impedance on the transmitter side is of its maximum value, which indicates a maximum power transfer. Besides, the series resonant method has better response to the fluctuations of the coupling coefficient [160]. A series resonant topology is therefore employed to configure the transmitter resonant circuit in order to maximize the current magnitude. Consequently, both transmitter resonant circuit and receiver resonant circuit should be configured as series resonant topology to achieve maximum attraction or repulsion force. From the perspective of an elementary pole pair, the underlying operation principle, as well as the simulation validation of the proposed MRCM will be demonstrated in Chapter III.

2.2 Machine Control

In this section, the mathematical model of PMSM is first presented. Two machine control algorithms, i.e., DTC and MPTC, are then introduced and analyzed. The development of load torque observer and the utilization of maximum torque per Ampere criterion are demonstrated as the foundations of the primary contributions in this thesis.

2.2.1 Mathematical Model of PMSM

In last few decades, servo drive has found a wide variety of applications in industry. Servo drives require high performance in terms of accuracy and dynamics, especially on speed control. A great deal of on-going research

concerns the motor structure optimization and control methods. Among different motor types, the permanent magnetic synchronous motors (PMSMs) have been widely used due to their high torque-to-inertia ratio, high power density and high efficiency.

Due to the convenience of derivation, the generalized machine model of PMSM is commonly expressed in the dq synchronous coordinate. After the coordinate transformation from abc to dq reference frame, stator voltages u_d and u_q, and stator currents i_d and i_q are obtained as fundamental parameters for the formation of the machine model. The machine mathematical equations are well known, but for completeness they are quoted as follows

$$\boldsymbol{u}_s = u_d + ju_q \tag{2.12}$$

$$\boldsymbol{u}_s = u_d + ju_q \tag{2.13}$$

$$T = \frac{3}{2}p(\varphi_d i_q - \varphi_q i_d) \tag{2.14}$$

where

$$u_d = R_s i_d + \frac{d\varphi_d}{dt} - \omega\varphi_q \tag{2.15}$$

$$u_q = R_s i_q + \frac{d\varphi_q}{dt} + \omega\varphi_d \tag{2.16}$$

$$\varphi_d = L_d i_d + \varphi_f \tag{2.17}$$

$$\varphi_q = L_q i_q \tag{2.18}$$

The stator current can be expressed as

$$\frac{di_d}{dt} = -\frac{R_s}{L_d}i_d + \frac{L_q}{L_d}i_q\omega + \frac{1}{L_d}u_d \tag{2.19}$$

$$\frac{di_q}{dt} = -\frac{L_d}{L_q}i_d\omega - \frac{R_s}{L_q}i_q + \frac{1}{L_q}u_q - \frac{\varphi_f}{L_q}\omega \tag{2.20}$$

and the mechanical equation is

$$\frac{d\omega}{dt} = \frac{1}{J}T - \frac{B_m}{J}\omega - \frac{T_L}{J} \tag{2.21}$$

For the interior PMSM (IPMSM), the magnetic path of d-axis passes through the permanent magnets, while the magnetic path of q-axis passes through the iron cores. As permanent magnets have a higher reluctance than iron cores, the

inductance L_q is always larger than the inductance L_d. The electromagnetic torque is given by

$$T = \frac{3}{2}p\left(\varphi_f i_q + \Delta L i_d i_q\right) \tag{2.22}$$

where $\Delta L = L_d - L_q$.

However, for the surface PMSM (SPMSM), as both the magnetic paths of d-axis and q-axis pass through the permanent magnets, the difference between L_d and L_q is usually very small as $\Delta L \approx 0$. The electromagnetic torque can then be simplified as

$$T = \frac{3}{2}p\varphi_f i_q \tag{2.23}$$

As (2.23) is a more general torque expression, the work presented in this thesis is based on IPMSM. Above equations form the mathematical model of a PMSM. To conduct the simulation or experimental test, a detailed machine specification is required. Table 2.1 lists the parameters of PMSM, which will be used throughout the thesis.

TABLE 2.1
MACHINE AND CONTROL DATA

Symbol	Constants	Values
p	number of pole pairs	5
φ_f	PM rotor flux	0.088 Wb
R_s	stator resistance	0.636 Ω
L_d	d-axis inductance	0.012 H
L_q	q-axis inductance	0.02 H
B_m	viscous friction	0.0017 kgm/s^2
J	moment of inertia	0.001 kgm^2
T_r	rated torque	7.8 Nm
ω_r	rated speed	1200 rpm
I_r	rated current	11.36A

2.2.2 Direct Torque Control

After the extensive research on the conventional and mature field-oriented control (FOC), direct torque control (DTC) is another research hotspot over the past years for machine drives [56, 57]. DTC has the merits including simple structure, fast dynamic response and straight-forward algorithm. In this subsection, the principle of DTC is concisely introduced, and the limitation of DTC is pointed out.

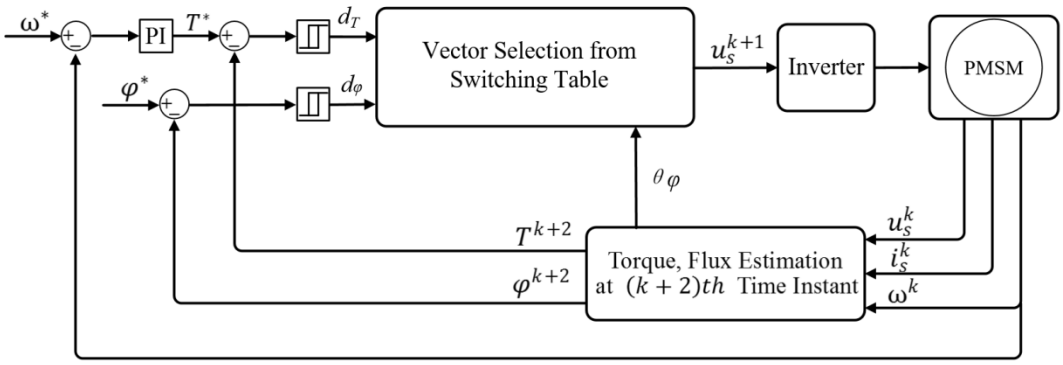

Fig. 2.4. Diagram of conventional DTC

Fig. 2.4 presents the diagram of conventional DTC. Using the measured machine information at *k th* time instant, including the stator current $\boldsymbol{i}_s^k$, stator voltage $\boldsymbol{u}_s^k$, rotor speed ω^k and electrical angle θ^k, the parameter estimation at $(k+2)th$ time instant can be conducted to compensate the one-step delay characteristic in practical applications. The reference torque T^* is obtained from the PI adapter, where the input of PI is the difference between the reference speed and measured speed. The obtained reference torque T^* and the user-defined flux reference φ^* are then to subtract the estimated torque at $(k+2)th$ time instant T^{k+2} and the estimated flux at $(k+2)th$ time instant φ^{k+2}, respectively. Sign of torque error d_T and sign of flux error d_φ are then generated by two hysteresis comparators.

The key component of DTC is a user pre-defined switching table. This switching table is constituted by eight voltage vectors, i.e., $\boldsymbol{V_0(000)}, \boldsymbol{V_1(001)}$,

$\boldsymbol{V_2(010), V_3(011), V_4(100), V_5(101), V_6(110), V_7(111)}$. For simplicity and convenience, these eight voltage vectors will be abbreviated as

$$\boldsymbol{u_s} \in \{\boldsymbol{V_0}, \boldsymbol{V_1}, \ldots \boldsymbol{V_6}, \boldsymbol{V_7}\} \tag{2.24}$$

in following chapters.

The optimal voltage vector, which will be applied to the inverter, is selected from switching table depending on the specific combination of the sign of torque error d_T, the sign of flux error d_φ and the electrical angle θ^k at *k th* time instant. The formation of the switching table is based on the variation of the $\frac{dT}{dt}$ and $\frac{d|\boldsymbol{\varphi}|}{dt}$ corresponding to different electrical angle.

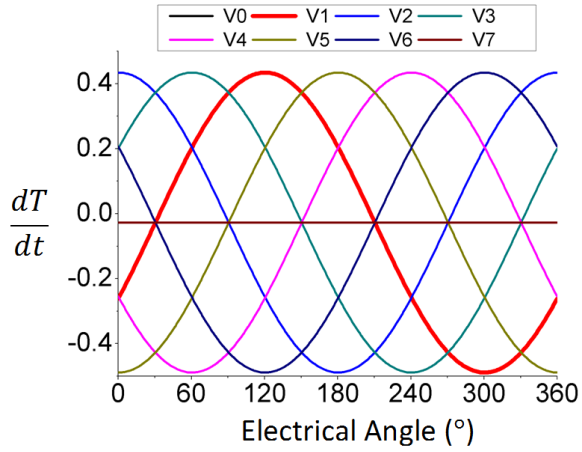

(a)

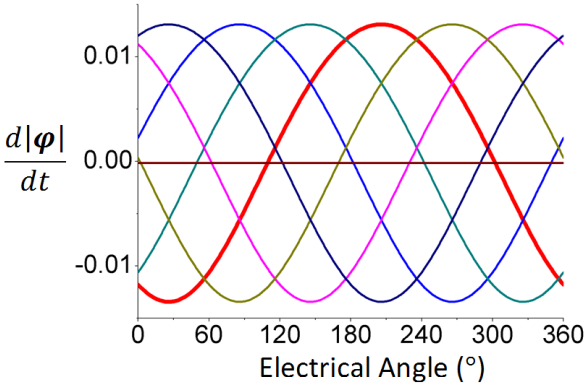

(b)

Fig. 2.5. The variation of (a) $\frac{dT}{dt}$ and (b) $\frac{d|\boldsymbol{\varphi}|}{dt}$ corresponding to different electrical angle for eight voltage vectors.

As is shown in Fig. 2.5, the variations of $\frac{dT}{dt}$ and $\frac{d|\boldsymbol{\varphi}|}{dt}$ corresponding to different electrical angle is demonstrated for eight voltage vectors. Besides, a conventional method is to divide a period of electrical angle (360°) into six sectors (S_1,S_2…S_6) [59], as is shown in Fig. 2.6. At different time instant, there are different combinations of $\frac{dT}{dt}$, $\frac{d|\boldsymbol{\varphi}|}{dt}$ and sector number.

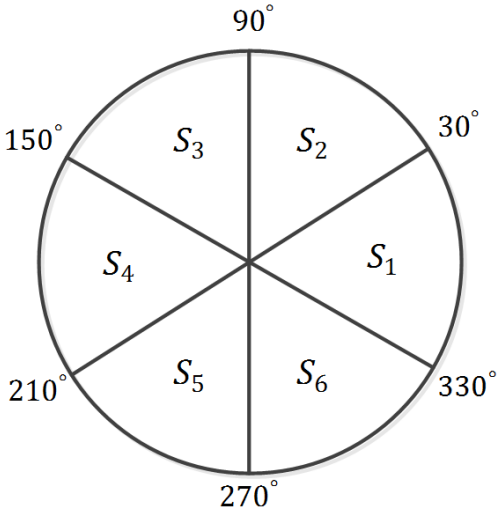

Fig. 2.6. Section of electrical angle for conventional DTC

Based on Fig 2.5 and Fig 2.6, a typical switching table of conventional DTC is defined in Table 2.2.

TABLE 2.2
SWITCHING TABLE OF CONVENTIONAL DTC

d_T	d_φ	S_1	S_2	S_3	S_4	S_5	S_6
1	1	$\boldsymbol{V_6}$	$\boldsymbol{V_2}$	$\boldsymbol{V_3}$	$\boldsymbol{V_1}$	$\boldsymbol{V_5}$	$\boldsymbol{V_4}$
1	0	$\boldsymbol{V_5}$	$\boldsymbol{V_4}$	$\boldsymbol{V_6}$	$\boldsymbol{V_2}$	$\boldsymbol{V_3}$	$\boldsymbol{V_1}$
0	1	$\boldsymbol{V_2}$	$\boldsymbol{V_3}$	$\boldsymbol{V_1}$	$\boldsymbol{V_5}$	$\boldsymbol{V_4}$	$\boldsymbol{V_6}$
0	0	$\boldsymbol{V_1}$	$\boldsymbol{V_5}$	$\boldsymbol{V_4}$	$\boldsymbol{V_6}$	$\boldsymbol{V_2}$	$\boldsymbol{V_3}$

The value of d_T and d_φ indicate the differences between the reference values and the measured values: 1 means the measured value is the lower than the reference value, whilst 0 means the measured value is the greater than the

reference value. The sign of torque error d_T, the sign of flux error d_φ and the sector (S_1 , S_2 … S_6) will locate an optimal voltage vector to lessen the difference/error. For example, when d_T and d_φ are 1, and the sector is located at S_1, the voltage vector $\boldsymbol{V_6}$ will be selected to increase the torque and flux.

Based on the machine parameters shown in Table 2.1, a simulation in MATLAB Simulink is conducted to present the performance of the conventional DTC, as is shown in Fig. 2.7. The flux reference is set to be 0.16 Wb. The sampling time is 100 μs. The PI parameters are set to be P=3 and I=0.5.

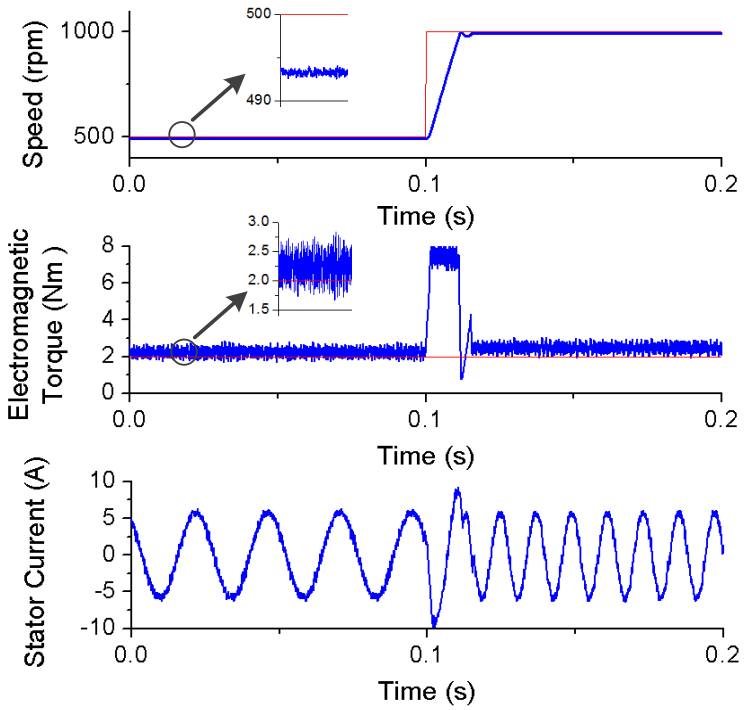

Fig. 2.7. Control performance of conventional DTC. From top: speed, electromagnetic torque and stator current.

Conventional DTC achieves satisfactory robustness, while the speed response is not good. When a new speed reference is changed suddenly, the speed can track the speed reference in a short time. However, a large speed offset is always of existence. Such speed offset is not allowable for practical applications, which may deteriorate or damage the system. After taking a long time, the speed can finally reach the reference value, as is shown in Fig. 2.8.

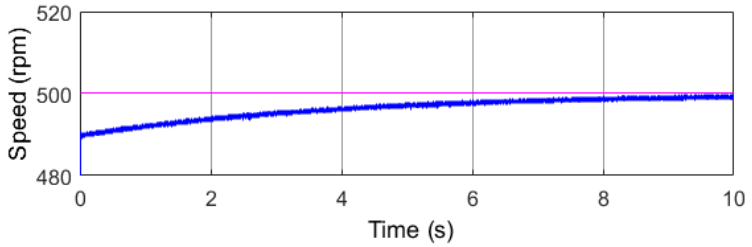

Fig. 2.8. Speed tracking performance of conventional DTC for a long time (P=2, I=0.5).

For conventional DTC, with careful tuned PI parameters, the speed offset can be reduced to some extent. However, it would result in relatively large speed ripple, as is demonstrated in Fig. 2.9.

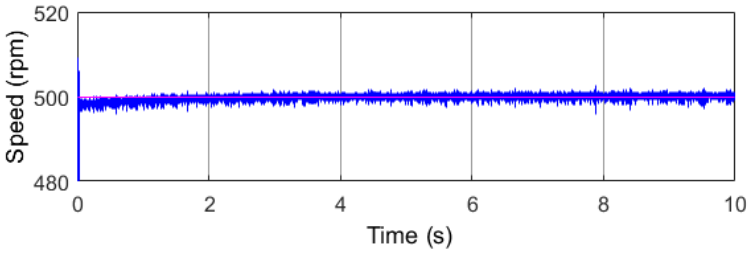

Fig. 2.9. Speed tracking performance of conventional DTC for a long time. (P=5, I=3.5).

Moreover, the torque ripple of conventional DTC should be regulated more moderately. The speed offset can be reduced by tuning PI parameters. However, with different PI parameters, there is no significant improvement on the torque ripple. Large torque ripple is the intrinsic drawback of the conventional DTC. It is because one period of electrical angle is roughly divided to six sections. The applied single voltage vector is simply selected in a pre-defined switching table depending on the signs of torque and flux. For the voltage vectors defined in the switching table, the changing rate of torque and flux is not optimized. More specifically, a general case is given below. For a particular time instant, the electrical angle is within the range of S_1, and the sign of d_T and d_φ are 1. In this case, a voltage vector, which can increase both torque and flux, should be selected and pre-defined in the switching table. Based on Fig. 2.5, both $\boldsymbol{V_2}$ and $\boldsymbol{V_6}$ can meet the requirement, but $\boldsymbol{V_6}$ is chosen as the voltage vector in the

switching table. Actually, $\boldsymbol{V_2}$ and $\boldsymbol{V_6}$ correspond to different changing rates of torque and flux, and optimal voltage vector should be one of them. However, conventional DTC simply employ the voltage vector predefined in the switching table, and the optimal voltage vector may not be the one defined in the switching table. Consequently, the torque ripple is large, and the current quality is not good enough.

To deal with the limitations of conventional DTC, model predictive control (MPC) is proposed to improve the control performance in terms of torque ripple and current THD.

2.2.3 Model Predictive Torque Control

In recent years, model predictive control (MPC) has been attracting much research attention due to its fast dynamics and flexible integration of various constraints. With several years of booming development, MPC has penetrated into many research fields, and two popular research orientations are grid-connected converters [98, 99, 161], and machine drives [126, 133, 140]. Compared to conventional DTC, MPC will not restricted by a predefined switching table, and has more selection freedom. Intrinsically, MPC is capable to handle the control objective of nonlinearity, multi-constraint and multi-variable. Different from DTC that voltage vectors are selected in a predefined switching table, MPC directly chooses the optimal voltage vector via a cost function with quantified control objectives, such as torque and flux in MPTC. The diagram of conventional MPTC is shown in Fig. 2.10.

The measured parameters at *k th* time instant are the same to DTC, i.e. stator current $\boldsymbol{i}_s^k$, stator voltage $\boldsymbol{u}_s^k$, rotor speed ω^k and electrical angle θ^k. The parameters at $(k+2)th$ time instant are estimated based on the mathematical model of PMSM. The outer speed loop first compares the reference speed with the measured speed, and the speed error is calculated as the input of the PI adapter. As PI parameters affect the control performance significantly, it is of

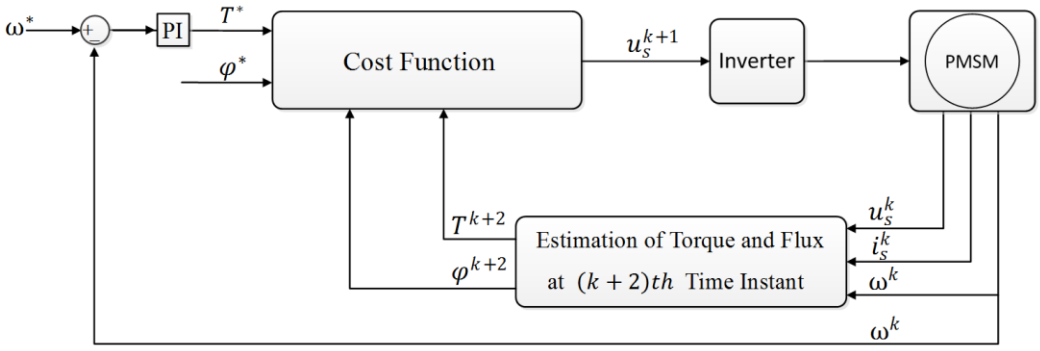

Fig. 2.10. Diagram of conventional MPTC

great importance to tune and select suitable values of PI parameters to maintain a satisfactory control performance. The torque reference is then generated from the PI adapter. Above parameters will be evaluated by the cost function to obtain the optimal voltage vector.

For conventional MPC, the cost function is usually constituted of many control variables, and the conventional MPTC is to employ torque and flux to develop the cost function [101-107]. In this case, the objective of the cost function is to minimize the torque error and flux error. Besides, a weighting factor ξ is always introduced to balance the weight between torque and flux. The cost function is expressed as

$$min.\, g = |T^{k+2} - T^*| + \xi|\varphi^{k+2} - \varphi^*| \tag{2.25}$$

$$\text{s.t.}\, \boldsymbol{u_s}^{k+1} \in \{V_0, V_1, \dots V_6, V_7\}$$

Each one of eight voltage vectors $\{V_0, V_1, \dots V_6, V_7\}$, corresponds to a set of estimated parameters at $(k+2)th$ time instant, including torque T^{k+2} and flux φ^{k+2}. The cost function will be compared every set's torque T^{k+2} and flux φ^{k+2} with their reference values. The voltage vector, which can achieve the minimum value of the cost function, will be selected as the one applying to the PMSM.

A simulation is conducted in MATLAB Simulink by using the machine parameters listed in Table 2.1. The simulation results are shown in Fig. 2.11.

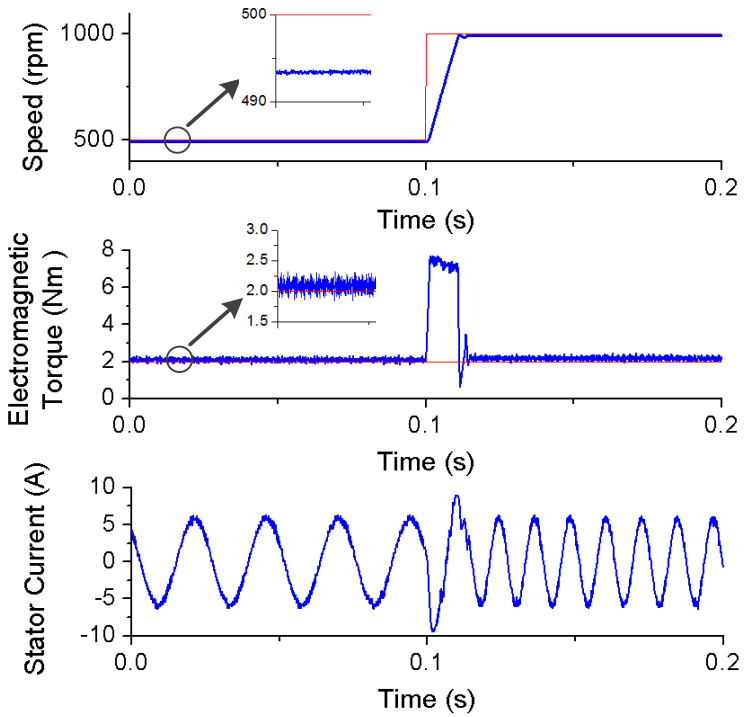

Fig. 2.11. Control performance of conventional MPC. From top: speed, electromagnetic torque and stator current.

As the control objective of MPTC is to manipulate the torque and flux, the torque ripple can be reduced significantly, and the current quality is improved to some extent. However, from Fig. 2.11, it can be seen that the speed offset is still large. Similar to conventional DTC, it is effective to reduce the speed offset of MPC by using well-tuned PI parameters. Nevertheless, there is a tradeoff between the speed offset and the ripples of speed and torque. As PMSM is a nonlinear system, it is time consuming and complicated to obtain suitable PI parameters to achieve better performance on both speed offset and ripples.

Through the manipulation of cost function, MPC is flexible to achieve different control objectives. The shortcoming of MPTC, i.e. large speed offset and ripple, can be overcome by the model predictive speed control (MPDSC). Although the control objective of MPDSC is to manipulate the speed, and response of torque may not be satisfactory, with some compensation, the torque ripple of MPDSC can be enhanced to be comparative to MPTC. More details are given in Chapter IV and V.

2.2.4 Load Torque Observer

In a motor control system, the load may change due to different working conditions. It is necessary to obtain the information of varying load torque to conduct the accurate parameter prediction. An on-line minimum order load torque observer (MOLTO) is thus employed to estimate the actual load torque [162]. This section presents the procedures to develop a load torque observer.

For better illustration, the state-space form of the observer can be expressed as

$$\dot{\boldsymbol{x}} = \mathbf{A}\boldsymbol{x} + \mathbf{B}\boldsymbol{u} \tag{2.26}$$

$$y = \mathbf{C}\boldsymbol{x} \tag{2.27}$$

or

$$\begin{bmatrix}\dot{x}_a \\ \dot{x}_b\end{bmatrix} = \begin{bmatrix}A_{aa} & A_{ab} \\ A_{ba} & A_{bb}\end{bmatrix}\begin{bmatrix}x_a \\ x_b\end{bmatrix} + \begin{bmatrix}B_a \\ B_b\end{bmatrix}u \tag{2.28}$$

$$\mathrm{y} = [C_a\ C_b]\begin{bmatrix}x_a \\ x_b\end{bmatrix} \tag{2.29}$$

where

$$\boldsymbol{x} = [T_L \quad \omega]^T,\ u = T,\ \mathbf{A} = \begin{bmatrix}0 & 0 \\ -\frac{1}{J} & -\frac{B_m}{J}\end{bmatrix},\ \mathbf{B} = \begin{bmatrix}0 \\ \frac{1}{J}\end{bmatrix},\ \mathbf{C} = [0 \quad 1] \tag{2.30}$$

T_L and ω are selected as the state variables. As T_L changes slowly with time during a short sampling period, it is assumed that $\dot{T}_L = 0$. T_L is the unmeasurable state variable. The state variable ω can be directly measured, and is equal to the output y. Based on the mechanical equation of PMSM, the matrices are obtained as shown in (2.28-2.29). Following the procedures of designing a full-order observer, (2.28) can be expressed as

$$\dot{\tilde{x}}_a = (A_{aa} - K_e A_{ba})\tilde{x}_a + A_{ab}x_b + B_a u + K_e(\dot{x}_b - A_{bb}x_b - B_b u) \tag{2.31}$$

where K_e is the observer gain. A derivative of x_b may amplify the noise of the observer, and $\dot{x}_b$ therefore should be eliminated. Therefore, (2.31) can be rewritten as

$$\begin{aligned}\dot{\tilde{x}}_a - K_e\dot{x}_b &= (A_{aa} - K_e A_{ba})\tilde{x}_a + (A_{ab} - K_e A_{bb})y + (B_a - K_e B_b)u \\ &= (A_{aa} - K_e A_{ba})(\tilde{x}_a - K_e y) + [(A_{aa} - K_e A_{ba})K_e + (A_{ab} - K_e A_{bb})]y + \\ &\quad (B_a - K_e B_b)u\end{aligned} \tag{2.32}$$

By defining

$$z = x_a - K_e y = x_a - K_e y \tag{2.33}$$

and

$$\tilde{z} = \tilde{x}_a - K_e y = \tilde{x}_a - K_e y \tag{2.34}$$

(2.32) becomes

$$\dot{\tilde{z}} = (A_{aa} - K_e A_{ba})\tilde{z} + [(A_{aa} - K_e A_{ba})K_e + (A_{ab} - K_e A_{bb})]y + (B_a - K_e B_b)u \tag{2.35}$$

Substituting matrices (2.30) into (2.33) and (2.35), the load torque can be predicted as

$$\tilde{T}_L = \tilde{z} + K_e \omega \tag{2.36}$$

$$\dot{\tilde{z}} = \frac{K_e}{J}(\tilde{z} + K_e \omega + B_m \omega - T) \tag{2.37}$$

To investigate the observer stability, the error of between the estimated and actual values is

$$T_{L_{error}} = T_L - \tilde{T}_L \tag{2.38}$$

From (2.28), $\dot{x}_a$ and $\dot{x}_b$ can be described as

$$\dot{x}_a = A_{aa} x_a + A_{ab} x_b + B_a\, u \tag{2.39}$$

$$\dot{x}_b = A_{ba} x_a + A_{bb} x_b + B_b\, u \tag{2.40}$$

Substituting (2.40) into (2.31), (2.31) can be rewritten as

$$\dot{\tilde{x}}_a = (A_{aa} - K_e A_{ba})\tilde{x}_a + A_{ab} x_b + B_a u + K_e A_{ba} x_a \tag{2.41}$$

By subtracting (2.41) from (2.39), one can obtain

$$\dot{x}_a - \dot{\tilde{x}}_a = (A_{aa} - K_e A_{ba})(x_a - \tilde{x}_a) \tag{2.42}$$

Therefore, the error equation of MOLTO can be expressed as

$$\dot{T}_{L_{error}} = (A_{aa} - K_e A_{ba}) T_{L_{error}} \tag{2.43}$$

From (2.43), the characteristic equation is obtained as

$$\det[s\mathbf{I} - (A_{aa} - K_e A_{ba})] = 0 \tag{2.44}$$

Based on the Lyapunov stability for linear state space models, if all real parts of the eigenvalues of $A_{aa} - K_e A_{ba}$ are negative, the system is asymptotically stable. Assuming the desired eigenvalue of $A_{aa} - K_e A_{ba}$ is v, then

$$v = A_{aa} - K_e A_{ba} \tag{2.45}$$

i.e. ,

$$v = \frac{K_e}{J} \tag{2.46}$$

Therefore, a negative v (or a negative observer gain K_e) can guarantee the stability of the load torque observer. The MOLTO developed in this subsection will be employed in the proposed MPDSC methods to estimate the load torque in real time, and the estimated load torque is the essential parameter to conduct parameter estimation.

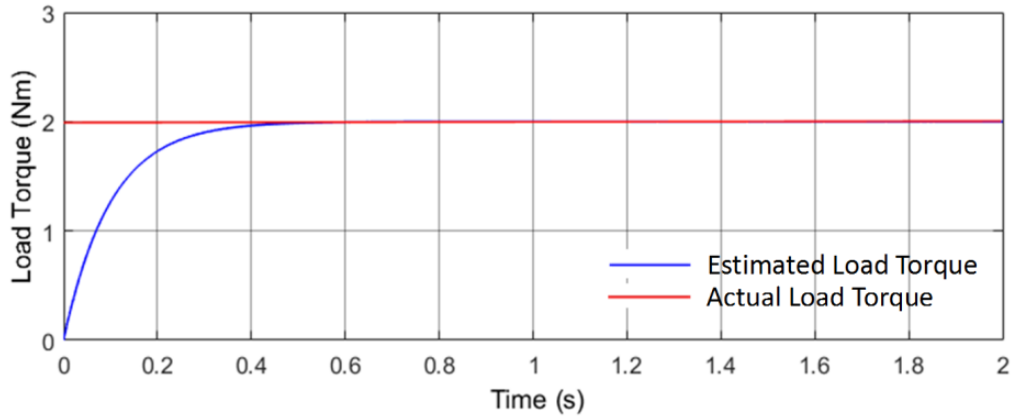

(a)

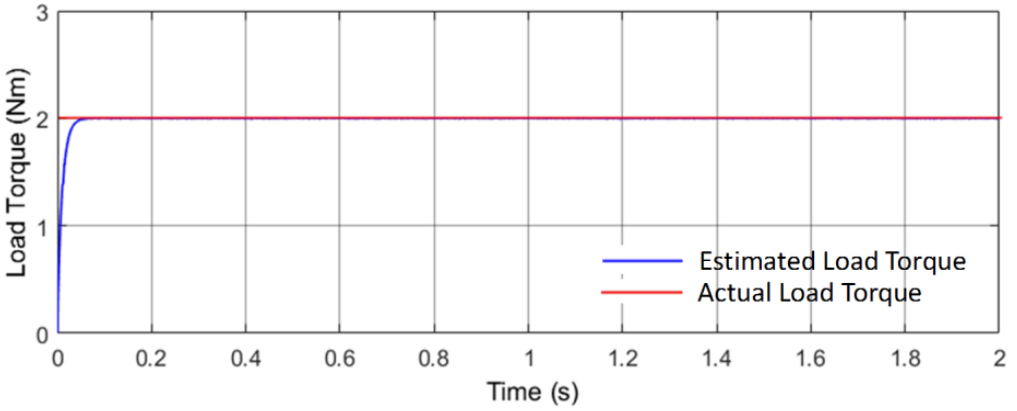

(b)

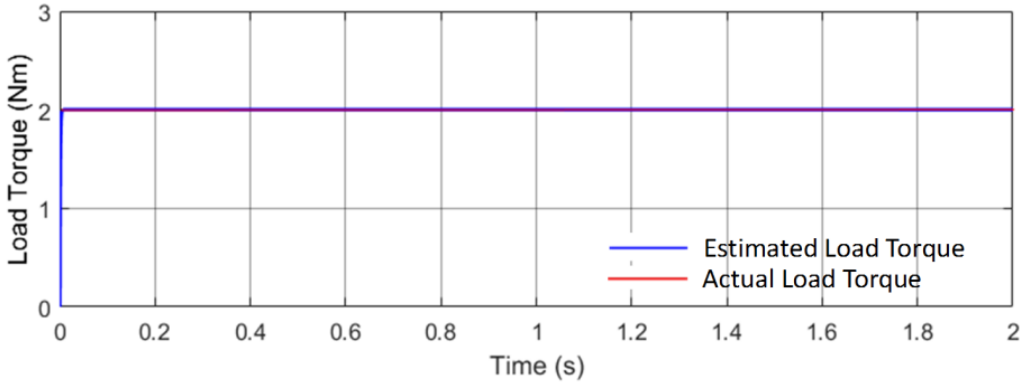

(c)

Fig. 2.12. Estimated load torque $\tilde{T}_L$ when (a) $v = -10$, (b) $v = -100$, (c) $v = -1000$.

Fig. 2.12 (a)-(c) compare the dynamic performance of the load torque observer when PMSM starts from standstill with v being -10, -100 and -1000, respectively. It can be seen that the estimated load torque can track the actual load torque in all the cases. Specifically, larger absolute value of the desired eigenvalue v enables a faster response.

In this thesis, above load torque observer is employed to estimate the actual load torque, which is necessary to conduct the accurate parameter estimation.

2.2.5 Maximum Torque per Ampere

To obtain the highest electrical efficiency, a PMSM should operate on the maximum torque per ampere (MTPA) trajectory when the motor speed is below the rated speed. For different working conditions, particular reference values of stator flux should be employed to meet the MTPA operation. The calculation procedures are demonstrated in this subsection. Assuming that

$$i = |i|$$

$$i_d = -i \sin\gamma$$

$$i_q = i \cos\gamma$$

where $\gamma = \arctan\left(-\frac{i_d}{i_q}\right)$. For surface PMSM (SPMSM), the expression of electromagnetic torque (2.23) can be rewritten as

$$T = \frac{3}{2} p \varphi_f i \cos\gamma \tag{2.47}$$

The trajectory of MTPA can be calculated by

$$\frac{\partial T}{\partial \gamma} = -\frac{3}{2} p \varphi_f i \sin\gamma = 0 \tag{2.48}$$

The unique solution of (2.48) is $i_d = 0$. For a given reference value of load torque $T_L{}^*$, a reference value of $i_q{}^*$ can be calculated based on (2.47),

$$i_q{}^* = \frac{T_L{}^*}{\frac{3}{2} p \varphi_f} \tag{2.49}$$

The reference value of stator flux φ^* is therefore obtained based on (2),

$$\varphi^* = \sqrt{{\varphi_f}^2 + \left(\frac{L_q {T_e}^*}{\frac{3}{2} p \varphi_f}\right)^2} \tag{2.50}$$

For interior PMSM (IPMSM), the expression of electromagnetic torque (2.22) can be rewritten as

$$T = \frac{3}{2} p\left(\varphi_f i \cos\gamma - \Delta L i^2 \cos\gamma \sin\gamma\right) = 0 \tag{2.51}$$

Applying $\frac{\partial T}{\partial \gamma}$, the solution is [16]

$$i_d + \frac{\Delta L}{\varphi_f}\left({i_d}^2 - {i_q}^2\right) = 0 \tag{2.52}$$

For a given reference value of load torque ${T_L}^*$, solving the equation set of (11) and (34), the reference value of ${i_d}^*$ can be obtained by solving the equation

$$b^2 c {i_d}^4 + (b^2 + 2ab){i_d}^3 + (2ab + a^2 c){i_d}^2 + a^2 i_d - c{T_L}^* = 0 \tag{2.53}$$

with the condition of

$$\frac{2\Delta L}{\varphi_f} i_d + 1 < 0 \text{ and } i_d + c{i_d}^2 > 0 \tag{2.54}$$

where $a = \frac{3}{2} p \varphi_f$, $b = \frac{3}{2} p \Delta L$ and $c = \frac{\Delta L}{\varphi_f}$. The reference value of stator flux φ^* is therefore obtained based on (2),

$$\varphi^* = \sqrt{\left(L_d {i_d}^* + \varphi_f\right)^2 + \left(L_q \sqrt{\frac{{i_d}^* + c{{i_d}^*}^2}{c}}\right)^2} \tag{2.55}$$

As heavy calculation burden is demanded to obtain the reference value of stator flux for IPMSM, a look-up table is usually pre-established based on particular machine parameters. A suitable reference value of stator flux, depending on the value of load torque, should be used to achieve higher efficiency. For simplicity, a fixed stator flux is selected and employed in the proposed MPDSC methods.

2.3 Summary

In this chapter, fundamentals and essentials of machine design and control are presented. First of all, the WPT system is introduced with the demonstration of resonant topologies. Different resonant topology has been investigated in terms of the phase characteristic, which is the underlying operation principle to develop the proposed MRCM. Then, relevant knowledge of machine control is presented. A specific machine mathematical model and machine parameters are demonstrated as the foundation of the machine control. Conventional machine control methods, namely DTC and MPTC, are discussed with in-depth analysis of their basic operational principles. The drawbacks of DTC and MPTC, which are the main incentive of the proposed MPDSC, have been pointed out. Moreover, as the essential parts of the proposed MPDSC and the contributions of this thesis, load torque observer and maximum toque per Ampere are explained with detailed mathematical derivation. In short, this chapter gives the theoretic foundation and the fundamentals of essentials for this thesis.

Chapter III

Magnetic Resonant Coupling Motor

3.1 Introduction

Presently, coil-to-coil WPT efficiencies of over 90% at multiple kW have been reported [163, 164], and would be an indication to the potential high efficiency of the proposed MRCM. Coupled with the small distance (a few millimeters) between stator and rotor power-transfer coils, the efficiency could be further enhanced. This chapter presents a novel MRCM. The proposed MRCM is configured without the use of any iron or permanent-magnet core. The proposed MRCM is a new generation of coreless and magnetless electric motor with the following merits:

1) The proposed MRCM has an inherent characteristic of unity power factor irrespective of the load condition.
2) The magnitude and direction of the output torque can be manipulated easily through the control of the excitation frequency.
3) The rotor can extract power from the stator to power devices installed on the rotor side, irrespective of the motor being rotating or not.

This chapter is organized as follows. In section 3.2, the operation principle of the proposed MPCM is introduced based on a pole pair. The magnitude and direction of the force in a pole pair, frequency splitting phenomenon, and the trajectory of resonant splitting frequency are discussed in this section. In addition, in section 3.3, the design procedure is demonstrated, and the simulations results using MAXWELL, PSIM and ANSYS Maxwell are presented to validate the feasibility of the proposed MRCM. Moreover, an excitation sequence is

elaborately designed, and a comparison between the proposed MRCM and IM are demonstrated. Finally, this chapter is concluded in section 3.4.

3.2 Pole Pair Analysis

The basic operation principle of this novel MRCM is illustrated in this section. A single pole pair as shown in Fig. 3.1 consists of two resonant circuits with series resonant topology. The material of stator and rotor cores is reinforce plastic.

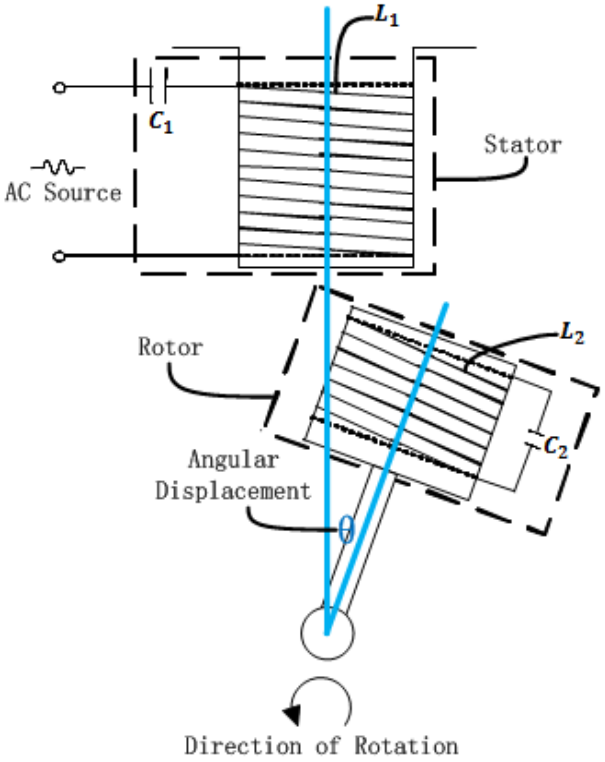

Fig. 3.1. A pole pair in the proposed MRCM.

The transmitter resonant circuit is referred as stator resonant circuit capable of generating an alternating magnetic field in response to a supplied sine-wave voltage, while the receiver resonant circuit is served as the rotor resonant circuit which is an independent closed circuit. The stator resonant circuit and the rotor resonant circuit are configured to have the same natural frequency ω_0 (or f_0). All stator or rotor windings should be configured with the same geometry and

symmetrical to avoid the adverse impact of end winding. Then, the equivalent circuit of a pole pair is shown in Fig. 3.2.

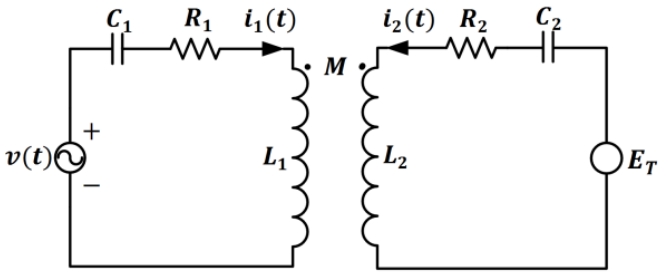

Fig. 3.2. Equivalent circuit of a pole pair.

Using the circuit theory, the relationship between the fundamental current phasor I_1 of transmitter resonant circuit, the fundamental current phasor I_2 of receiver resonant circuit, and the input RMS voltage V can be obtained as follows

$$\begin{bmatrix} j\omega L_1 + \frac{1}{j\omega C_1} + R_1 & j\omega M \\ j\omega M & j\omega L_2 + \frac{1}{j\omega C_2} + R_2 \end{bmatrix} \begin{bmatrix} \dot{I}_1 \\ \dot{I}_2 \end{bmatrix} = \begin{bmatrix} V \\ 0 \end{bmatrix} \tag{3.1}$$

The RMS current I_1 and I_2 in stator and rotor resonant circuits can be derived as

$$I_1 = \frac{V\sqrt{\left(\omega L_2 - \frac{1}{\omega C_2}\right)^2 + {R_2}^2}}{\sqrt{A^2 + B^2}} \tag{3.2}$$

$$I_2 = \frac{Vk\omega\sqrt{L_1 L_2}}{\sqrt{A^2 + B^2}} \tag{3.3}$$

where

$$A = R_1\left(\omega L_2 - \frac{1}{\omega C_2}\right) + R_2\left(\omega L_1 - \frac{1}{\omega C_1}\right)$$

$$B = R_1 R_2 - \left(\omega L_1 - \frac{1}{\omega C_1}\right)\left(\omega L_2 - \frac{1}{\omega C_2}\right) + k^2\omega^2 L_1 L_2$$

R_1 and R_2 are the internal resistance of stator and rotor resonant circuit respectively. E_T represents the output. k is the coupling coefficient which indicates the coupling degree between the stator resonant circuit. The relationship between coupling coefficient k and mutual inductance M is

$$k = \frac{M}{\sqrt{L_1 L_2}} \tag{3.4}$$

3.2.1 Natural Frequency

For any WPT system, it is necessary to select a suitable natural frequency f_0. The employment of higher natural frequency f_0 has merits including more compact, higher quality factor and longer transmission distance, but demands more expensive drive and control system.

As stator and rotor resonant circuits are special oscillation circuits, a process of starting oscillation is essential for each effective pole pair. As is indicated in Fig. 3.3, certain number of periods is needed to achieve a complete oscillation for resonant circuits in an effective pole pair. Since period is inversely proportional to the natural frequency f_0, the magnitude of natural frequency therefore determines the duration of starting oscillation process, and affects the performance of the proposed MRCM.

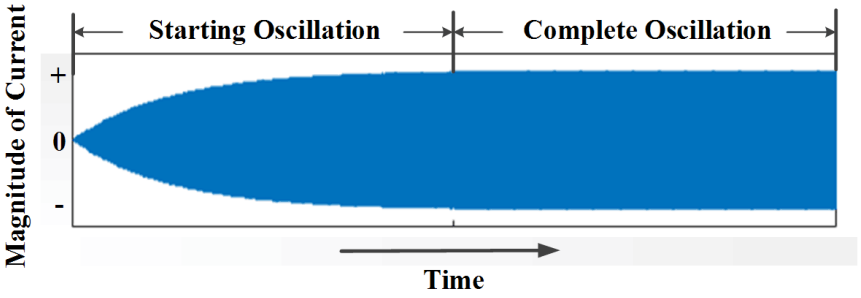

Fig. 3.3. Starting oscillation and complete oscillation in stator or rotor resonant circuit.

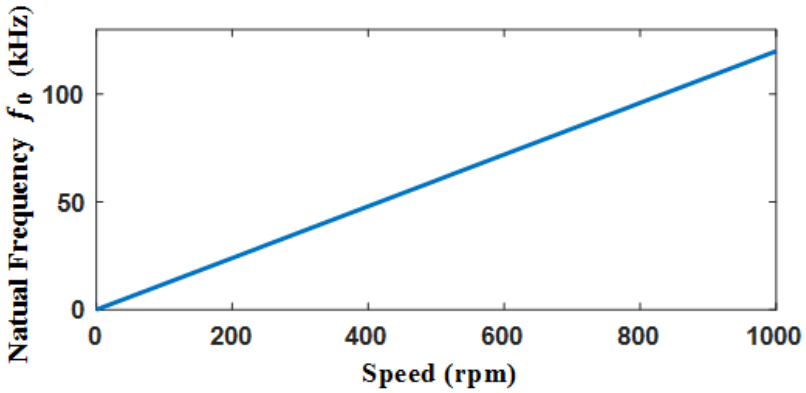

Fig. 3.4. Natural frequency f_0 for achieving complete oscillation within 5° rotation against speed.

For a rotor to rotate in a certain speed, a suitable natural frequency has to be selected to guarantee that stator and rotor resonant circuits can achieve the complete oscillation in a short time to generate maximum output electromagnetic force. For example, if the complete oscillation can be fulfilled in one hundred periods within 5 ° rotation, the relation between speed and natural frequency is depicted in Fig. 3.4, which could serve as a guideline for selecting the natural frequency f_0.

3.2.2 Force Magnitude and Direction

From the aforementioned analysis of topology selection, the phase difference δ between $\dot{I}_1$ and $\dot{I}_2$ determines the direction of the force developed in a pole pair. Moreover, the phase difference δ between $\dot{I}_1$ and $\dot{I}_2$ can affect the magnitude of the force developed in a pole pair. With the consideration of internal resistances, the expression of the phase difference δ between $\dot{I}_1$ and $\dot{I}_2$ is derived as

$$\delta = arctan \frac{R_2}{\frac{1}{\omega C_2} - \omega L_2} \tag{3.5}$$

For a pole pair, when $R_2 = 0$ or $R_2 > 0$, the locus of the phase difference δ between $\dot{I}_1$ and $\dot{I}_2$ for difference excitation frequency is plotted in Fig. 3.5.

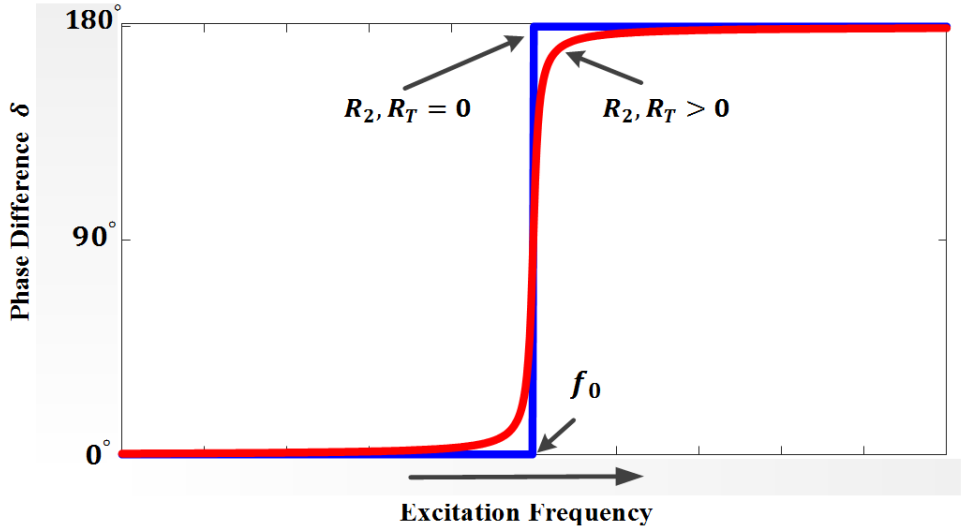

Fig. 3.5. Phase difference δ between $\dot{I}_1$ and $\dot{I}_2$ for difference excitation frequency for a pole pair when $R_2 = 0$ or $R_2 > 0$.

Due to the existence of R_2, the phase difference δ between $\dot{I}_1$ and $\dot{I}_2$ is no longer exactly 0° (when $f < f_0$) or 180° (when $f > f_0$), which would deteriorate the force developed in a pole pair. Besides, large values of R_2 in the rotor resonant circuit would also worsen the performance. Therefore, a smaller resistance value in rotor resonant circuit is preferable. Here, an attenuation coefficient γ is introduced to represent the magnitude and direction of the force developed in a pole pair.

$$\gamma = \frac{\int_0^{2\pi} sin(t)sin(t-\delta)}{\int_0^{2\pi} sin^2(t)} = cos\delta \tag{3.6}$$

When the excitation frequency f is smaller than f_0, the phase difference δ between $\dot{I}_1$ and $\dot{I}_2$ is in the range of $0^\circ \leq \delta < 90^\circ$. The attenuation coefficient γ is thus in the range of $0 < \gamma \leq 1$. Positive value of γ means an attraction force can be generated, and the maximal attraction force is achievable when $\gamma = 1$. Besides, when the excitation frequency f is greater than f_0, the phase difference δ between $\dot{I}_1$ and $\dot{I}_2$ is in the range of $90^\circ < \delta \leq 180^\circ$. The attenuation coefficient γ is therefore in the range of $-1 \leq \gamma < 0$. Negative value of γ means a repulsion force can be generated, and the maximal repulsion force is achievable when $\gamma = -1$. Moreover, no force would be generated in a pole pair when γ is equal to 0, and excitation frequency f is equal to f_0.

While the sign of attenuation coefficient γ determines the direction of the force in a pole pair, its magnitude can affect but not determine the magnitude of the force in a pole pair. To achieve a maximum force magnitude in a pole pair, the excitation frequency has to follow the frequency splitting trajectory for different angular displacement θ.

3.2.3 Frequency Splitting Phenomenon

The angular displacement θ shown in Fig. 3.1 indicates the position of the rotor resonant circuit relative to the stator resonant circuit. For a specific value of

the angular displacement θ, there is a corresponding value of the coupling coefficient k.

In the strong coupling condition, where the coupling coefficient k is greater than the critical coupling coefficient k_c, the optimal excitation frequency to achieve the maximum values of I_1 and I_2 splits into two specific frequency sets. It is the frequency splitting phenomenon as shown in Fig. 3.6.

The critical coupling coefficient k_c can be derived as follows. By letting $\omega = \omega_0$ in (3.3), I_2 is

$$I_2 = \frac{V\omega_0 k\sqrt{L_1 L_2}}{R_1 R_2 + k^2 {\omega_0}^2 L_1 L_2} \tag{3.7}$$

The first derivative of I_2 to k is

$$\frac{dI_2}{dk} = \frac{V\omega_0\sqrt{L_1 L_2}(R_1 R_2 - k^2 {\omega_0}^2 L_1 L_2)}{(R_1 R_2 + k^2 {\omega_0}^2 L_1 L_2)^2} \tag{3.8}$$

Then, solving k for $\frac{dI_2}{dk} = 0$. The value of k_c is analytically derived as

$$k_c = \sqrt{\frac{R_1 R_2}{{\omega_0}^2 L_1 L_2}} = \frac{1}{\sqrt{Q_1 Q_2}} \tag{3.9}$$

where Q_1 and Q_1 are the quality factor for stator resonant circuit and rotor resonant circuit respectively. The stator and rotor resonant circuits in a pole pair should always be configured to have a coupling coefficient k which is always greater than critical coupling coefficient k_c.

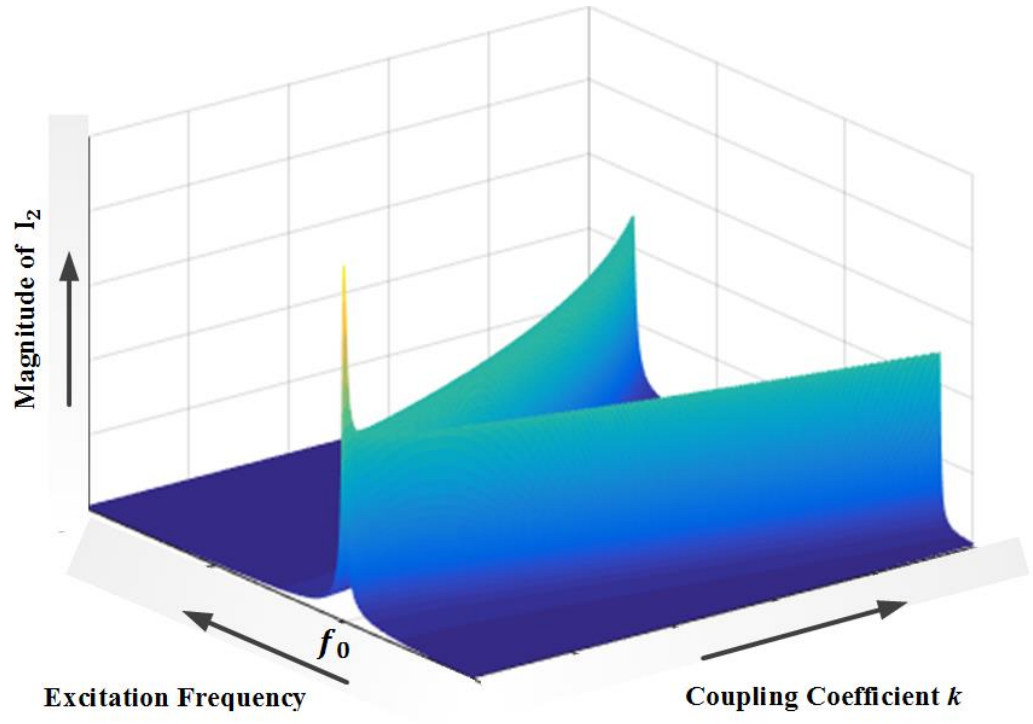

(a)

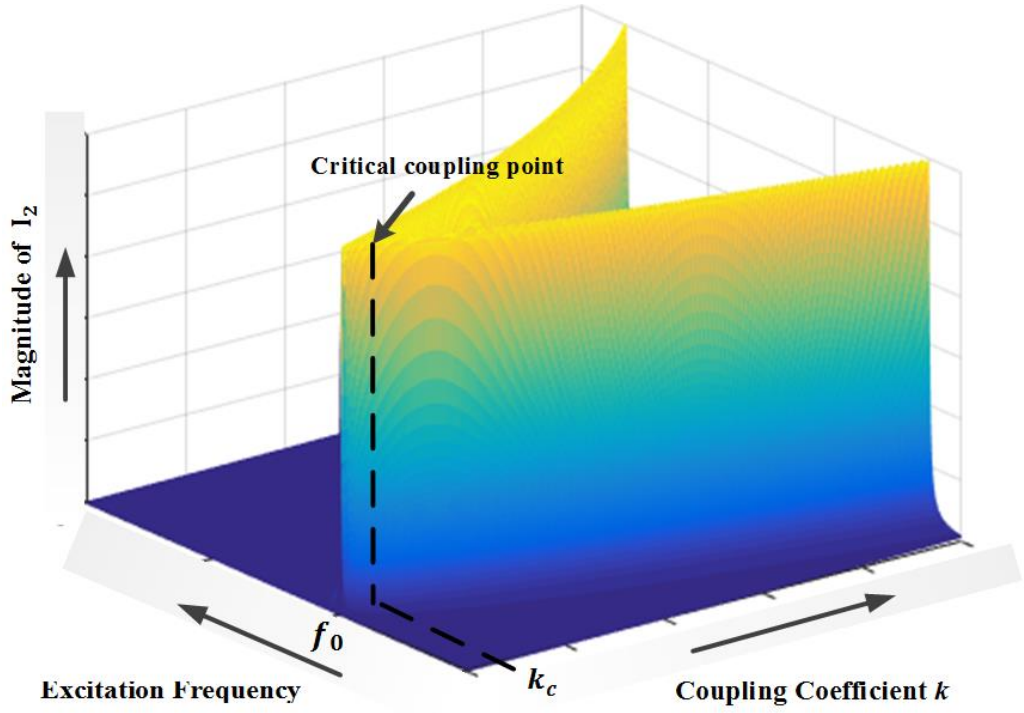

(b)

Fig. 3.6. Frequency splitting phenomenon with different excitation frequency and coupling coefficient for (a) I_1 and (b) I_2.

3.2.4 Lower/Higher Resonant Splitting Frequency

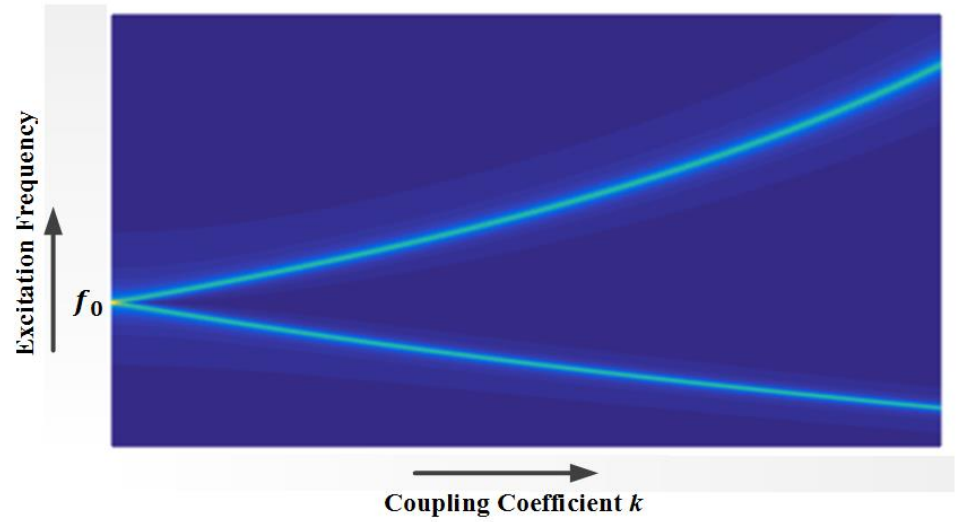

(a)

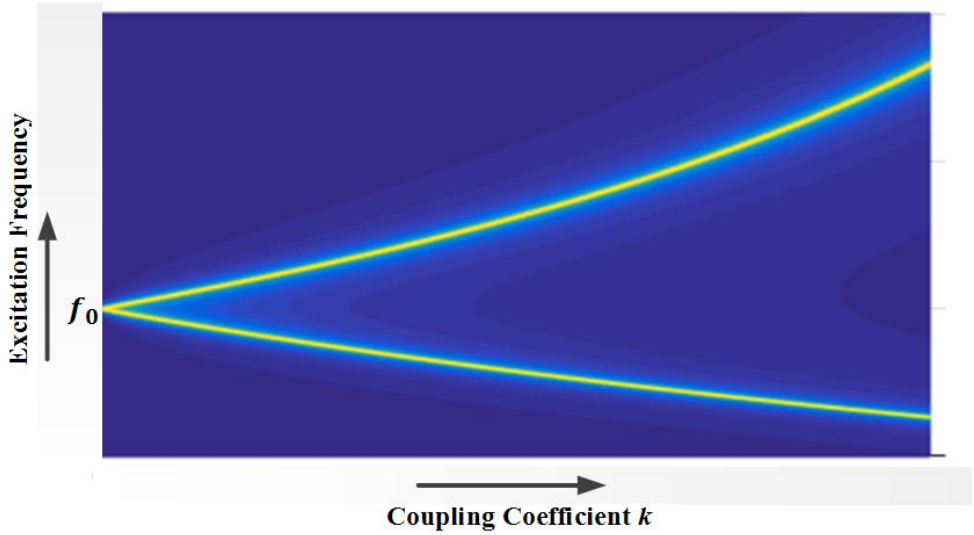

(b)

Fig. 3.7. Trajectory of lower resonant splitting frequency f_L and higher resonant splitting frequency f_H. (a) in the view of I_1. (b) in the view of I_2.

For the aforementioned two frequency sets to achieve the maximum values of I_1 and I_2, one set of which is lower than the natural frequency f_0, named as the lower resonant splitting frequency f_L, while the other higher than the natural frequency f_0 is named as the higher resonant splitting frequency f_H. The trajectory of lower resonant splitting frequency f_L and higher resonant splitting

frequency f_H are shown in Fig. 3.7, where I_1 and I_2 have the same trajectory of lower resonant splitting f_L and higher resonant splitting frequency f_H.

The lower resonant splitting frequency f_L and higher resonant splitting frequency f_H can be derived as follows. With the assumption of no resistances, the undamped natural response is

$$\begin{bmatrix} 1-\frac{{\omega_0}^2}{\omega^2} & k\sqrt{\frac{L_2}{L_1}} \\ k\sqrt{\frac{L_1}{L_2}} & 1-\frac{{\omega_0}^2}{\omega^2} \end{bmatrix}\begin{bmatrix} I_1 \\ I_2 \end{bmatrix} = \begin{bmatrix} 0 \\ 0 \end{bmatrix} \tag{3.10}$$

The assumption of neglecting the internal resistances is reasonable since internal resistances are usually much smaller than the resonant impedance ωL and $\frac{1}{\omega C}$. (3.10) can be rearranged as

$$\frac{{\omega_0}^2}{\omega^2}\begin{bmatrix} I_1 \\ I_2 \end{bmatrix} = \begin{bmatrix} 1 & k\sqrt{\frac{L_2}{L_1}} \\ k\sqrt{\frac{L_1}{L_2}} & 1 \end{bmatrix}\begin{bmatrix} I_1 \\ I_2 \end{bmatrix} \tag{3.11}$$

where $\frac{{\omega_0}^2}{\omega^2}$ is the eigenvalue of the matrix *A*, which is written as

$$A=\begin{bmatrix} 1 & k\sqrt{\frac{L_2}{L_1}} \\ k\sqrt{\frac{L_1}{L_2}} & 1 \end{bmatrix} \tag{3.12}$$

The eigenvalue of matrix *A* can be calculated as

$$\frac{{\omega_0}^2}{\omega^2} = 1+k, 1-k \tag{3.13}$$

The expressions of lower resonant splitting frequency f_L and higher resonant splitting frequency f_H are therefore derived as

$$f_L = \frac{\omega_0}{2\pi\sqrt{1+k}}, f_H = \frac{\omega_0}{2\pi\sqrt{1-k}} \tag{3.14}$$

Equation (3.14) of the lower resonant splitting frequency f_L and higher resonant splitting frequency f_H are the function of coupling coefficient k. Since coupling coefficient k is directly related to the angular displacement θ, the

values of lower resonant splitting frequency f_L and higher resonant splitting frequency f_H correspond to the angular displacement θ. As the force generated in a pole pair is directly proportional to the magnitude of I_1 and I_2, the highest magnitude of I_1 and I_2 is preferred. To achieve maximum magnitude of I_1 and I_2, and thus to generate the possible maximum force in a pole pair, the excitation frequency f must follow the trajectory of lower resonant splitting frequency f_L and higher resonant splitting frequency f_H.

3.2.5 Power Factor

The power factor (PF) is defined as the ratio of the real power to the apparent power. Unity PF is preferable for all electric-motor loads since higher PF indicates lower cost and higher efficiency. Most conventional electric motors, such as IMs and PMSMs, have relatively poor PFs (< 0.9), though capacitors are installed to compensate the inductance of copper winding.

In an electric motor, PF can be represented by the phase difference between the input voltage and current. The phase difference φ between V and $\dot{I}_1$ can be derived as

$$\varphi = arctan \frac{(\omega L_1 - \frac{1}{\omega C_1}) - \frac{\omega^2 M^2 (\omega L_2 - \frac{1}{\omega C_2})}{{R_2}^2 + (\omega L_2 - \frac{1}{\omega C_2})^2}}{R_1 + \frac{\omega^2 M^2 R_2}{{R_2}^2 + (\omega L_2 - \frac{1}{\omega C_2})^2}} \tag{3.15}$$

and PF can then be calculated as

$$\text{PF} = \cos\varphi \tag{3.16}$$

When applying lower resonant splitting frequency f_L and higher resonant splitting frequency f_H, the variation of PF can be depicted as is shown in Fig. 3.8. Smaller value of R_2 and smaller absolute value of angular displacement θ corresponds to higher PF for the proposed MRCM. Since R_2 is usually small, the power factor of the proposed MRCM is close to unity. In practice, R_2 should be less than 1% of the total impedance to achieve a power factor close to unity.

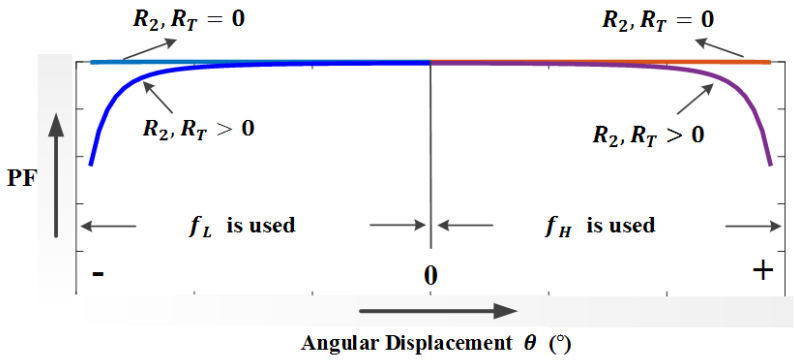

Fig. 3.8. Variation of PF corresponding to different angular displacement θ and different R_2.

3.2.6 Operation Principle

From the perspective of a pole pair, the underlying operation principle is illustrated as follows. As shown in Fig. 3.9 (a), when the rotor resonant circuit is approaching the stator resonant circuit, for different angular displacement θ, the stator resonant circuit would be powered with the trajectory of the low resonant splitting frequency f_L to generate the possible maximum force. At such a circumstance, as the phase difference δ between $\dot{I}_1$ and $\dot{I}_2$ is 0°, the stator and rotor poles would have the same polarity. An attraction force can be therefore developed between the stator resonant circuit and the adjacent rotor resonant circuit.

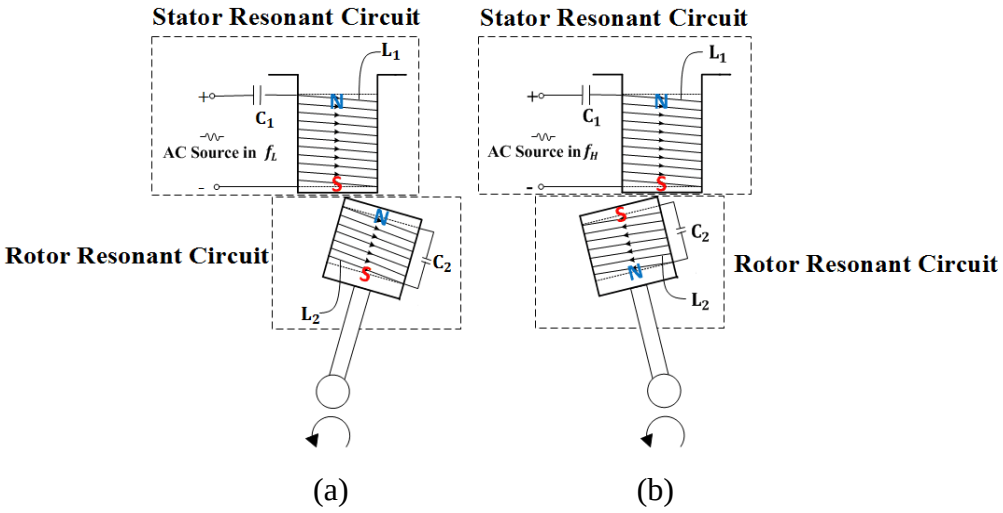

Fig. 3.9. Polarity demonstration for a pole pair with excitation frequency in (a) lower resonant frequency f_L (b) higher resonant frequency f_H.

Furthermore, as shown in Fig. 3.9 (b), when the rotor resonant circuit is leaving the stator resonant circuit, for different angular displacement θ, the stator resonant circuit would be powered with the trajectory of the high resonant splitting frequency f_H to generate the possible maximum force. In this case, as the phase difference δ between $\dot{I}_1$ and $\dot{I}_2$ is 180°, the stator and rotor poles would have the opposite polarity. A repulsion force can thus be developed between them. With the coordination of those attraction and repulsion forces, the rotor could be driven to rotate and operates as an electric motor. Besides, different arrangement of pole number and pole ratio could be developed based on such a pole pair.

3.3 Design Guideline and Validation

The pole pair is the fundamental element of a complete MRCM, and different pole-ratio arrangement could be further optimized based on the pole pair. Therefore, simulation results shown in this section are from the perspective of a single pole pair. The basic design procedures are demonstrated in the following.

Preliminary Design

- Selection of Resonant Topology
- Motor Dimension Design

  Determine the diameter of stator and rotor, diameter of copper wire, winding turns, air gap, etc. based on the desired output torque.
- Selection of Natural Resonant Frequency

  Higher speed demands higher natural resonant frequency.
- Selection of Capacitor Value

  After obtaining the value of the winding inductance, calculating the required value of discrete capacitor based on the natural resonant frequency.

Secondary Design

- Trajectory of Coupling Coefficient k

  Determine the variation of coupling coefficient k for different angular displacement θ.

- Effective Angular Range

  Determine the effective angular range by the critical coupling coefficient k_c.

- Trajectory of Resonant Splitting Frequency

  Determine the trajectory of lower resonant splitting frequency f_L and higher resonant splitting frequency f_H for different angular displacement θ.

- Trajectory of Attenuation Coefficient γ

  Determine the force magnitude and direction.

The proposed MRCM has been comprehensively validated using computer simulations in MATLAB, PSIM and ANSYS Maxwell. As shown in Fig. 3.10, a 2D pole pair model is firstly developed in ANSYS Maxwell. The constructional dimension and technical parameters are listed in Table 3.1 with practical consideration.

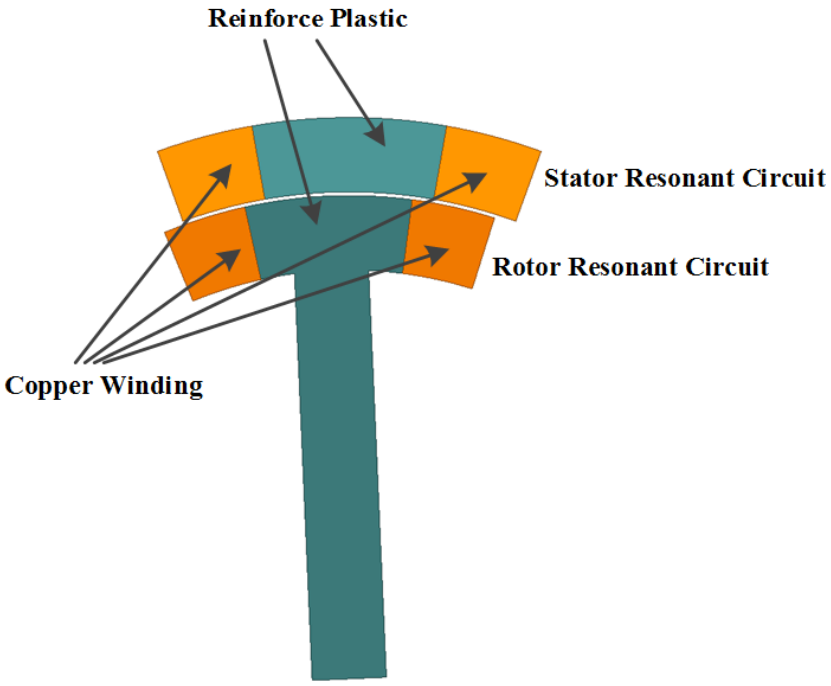

Fig. 3.10. A 2D pole pair model in ANSYS Maxwell

TABLE 3.1
Design Parameters of Proposed MRCM

Symbol	Parameters	Values
	2D Model Specifications	
-	model depth	200 mm
-	outer radius of stator	150 mm
-	outer radius of rotor	130 mm
-	air gap	1 mm
-	section area of copper winding	400 mm^2
-	number of stator poles	10
-	number of rotor poles	8
-	estimated weight	37.8 kg
	Resonant Circuit in a Pole Pair	
N_1, N_2	number of turns of stator and rotor winding	100, 100
L_1, L_2	inductance of stator and rotor winding	1.1093 mH, 1.1467 mH
C_1, C_2	capacitance in stator and rotor resonant circuit	0.0571 μF, 0.0552 μF
R_1, R_2	internal resistance of stator and rotor winding	0.2 Ω, 0.2 Ω
f_0	natural frequency	20 kHz
	Excitation	
V	RMS value of voltage source	6 V
-	f_L at $-5°$ angular displacement θ	16.786 kHz
-	f_H at 5° angular displacement θ	26.251 kHz

The turns of stator and rotor winding are 96 and 280 respectively to develop a large inductance. Besides, litz copper wire is employed to generate small internal resistances of stator and rotor winding.

3.3.1 k, f_L, f_H and γ

The self-inductance and mutual inductance of stator and rotor windings at different angular displacement θ is simulated using the 2D model of Fig. 3.10. The coupling coefficient *k* is then calculated by (3.4), and the fitting curve of coupling coefficient *k* at different angular displacement θ is depicted in Fig. 3.11.

Substituting parameters in Table 3.1 into (3.9), k_c is calculated to be 0.0035. The corresponding angular displacement θ for k_c is around $\pm 14°$, which is the effective angular range for a pole pair.

Combining the simulation results of coupling coefficient k in Fig. 3.11 and the analytical expression in (3.14), the trajectory of lower resonant splitting frequency f_L and higher resonant splitting frequency f_H corresponding to different angular displacement θ can be calculated and depicted in Fig. 3.12.

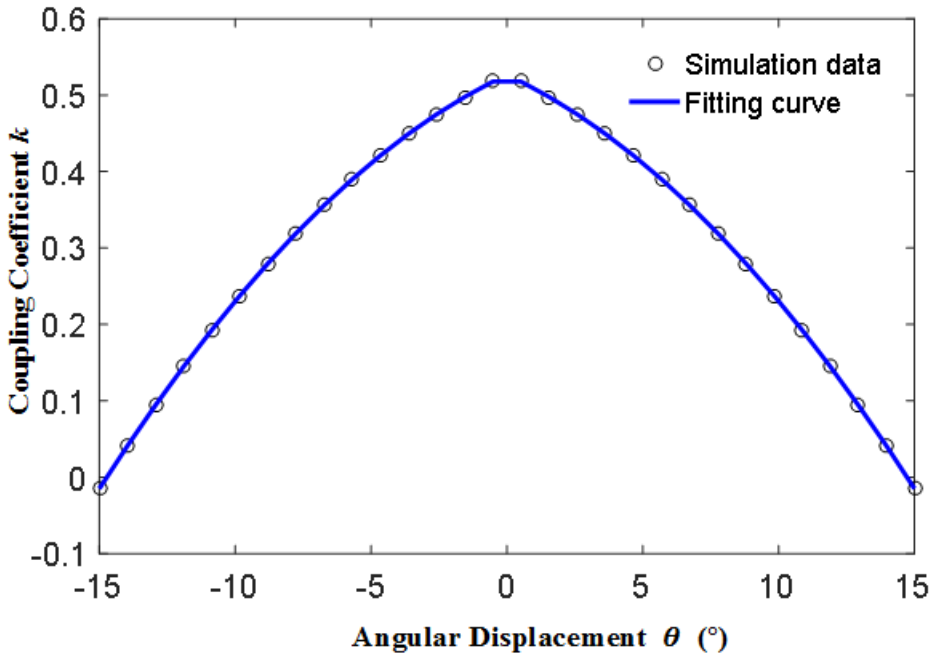

Fig. 3.11. Simulation result from ANSYS Maxwell: coupling coefficient k corresponding to different angular displacement θ

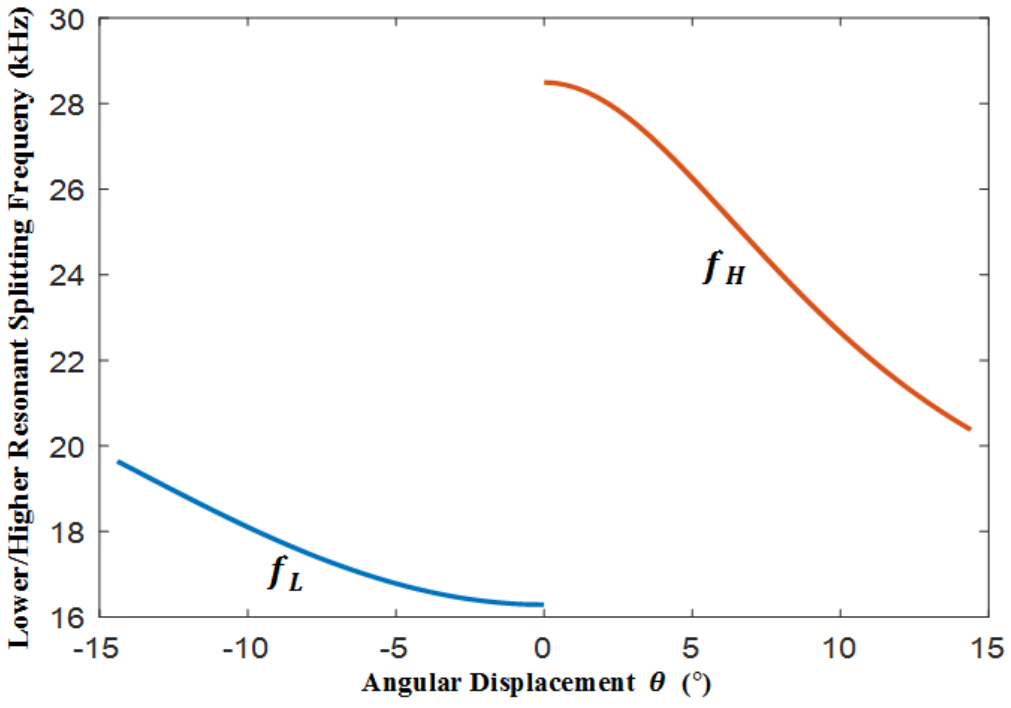

Fig. 3.12. Simulation result from MATLAB: trajectory of lower resonant splitting frequency f_L and higher resonant splitting frequency f_H corresponding to different angular displacement θ

When the excitation frequency follows the trajectory of lower resonant splitting frequency f_L and higher resonant splitting frequency f_H as shown in Fig. 3.12, the magnitude of attenuation coefficient γ corresponding to different angular displacement θ can be obtained. As is shown in Fig. 3.13, the attenuation coefficient γ is approximately -1 when the lower resonant splitting frequency f_L is used, while the attenuation coefficient γ is approximately 1 when the higher resonant splitting frequency f_H is used. Fig. 3.13 indicates that, due to the small resistance value in the rotor resonant circuit, the possible maximum attraction and repulsion forces are achievable by using the lower resonant splitting frequency f_L and higher resonant splitting frequency f_H as the excitation frequency.

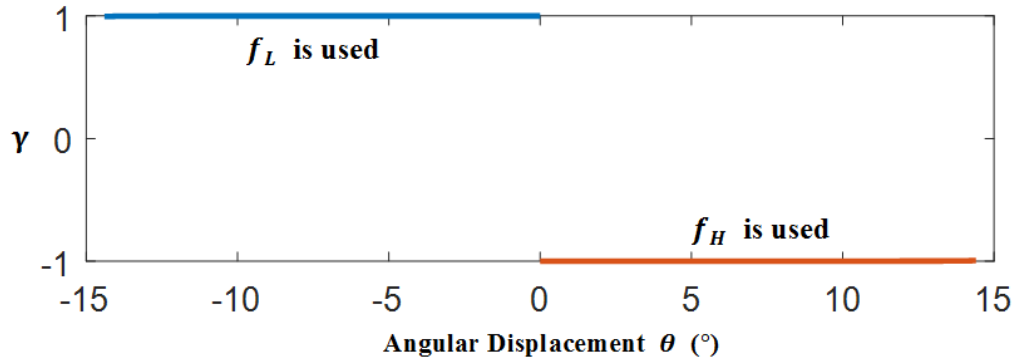

Fig. 3.13. Simulation result from MATLAB: the magnitude of attenuation coefficient γ corresponding to different angular displacement θ when f_L or f_H is used as the excitation frequency.

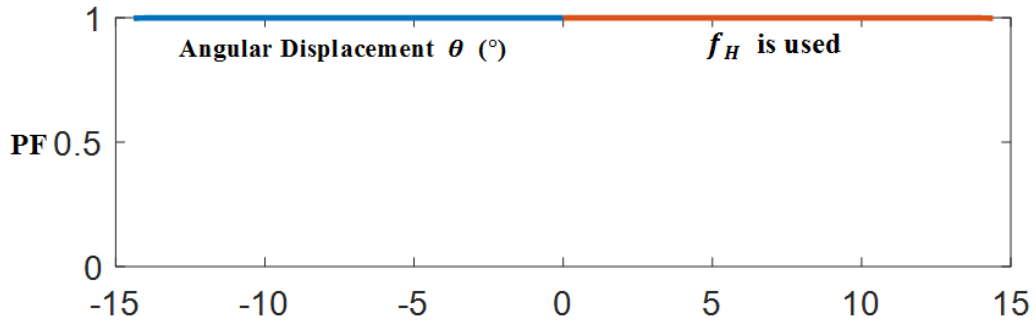

Fig. 3.14. Simulation result from MATLAB: the magnitude of PF corresponding to different angular displacement θ with $R_2 = 0.2\ \Omega$.

With the R_2 in TABLE 3.1, the magnitude of PF corresponding to different angular displacement θ can be obtained from the simulation as is shown in Fig. 3.14. A unity power factor can be maintained at all angular displacement θ for the proposed MRCM.

3.3.2 RMS Currents and Average Torque

Using the data obtained in Fig. 3.11-3.13, the magnitudes of RMS current I_1 and I_2 corresponding to different angular displacement θ are then simulated in PSIM. As is shown in Fig. 3.15, blue curve is the RMS current I_1, while the red curve is the RMS current I_2. When the lower resonant splitting frequency f_L is used as the excitation frequency, the magnitude of RMS current I_1 is greater than that of RMS current I_2. However, when the higher resonant splitting frequency f_H is used as the excitation frequency, the magnitude of RMS current I_1 is always smaller than that of RMS current I_2. The possible reason is that the variation rate of capacitive and inductive impedance is different with the frequency variation.

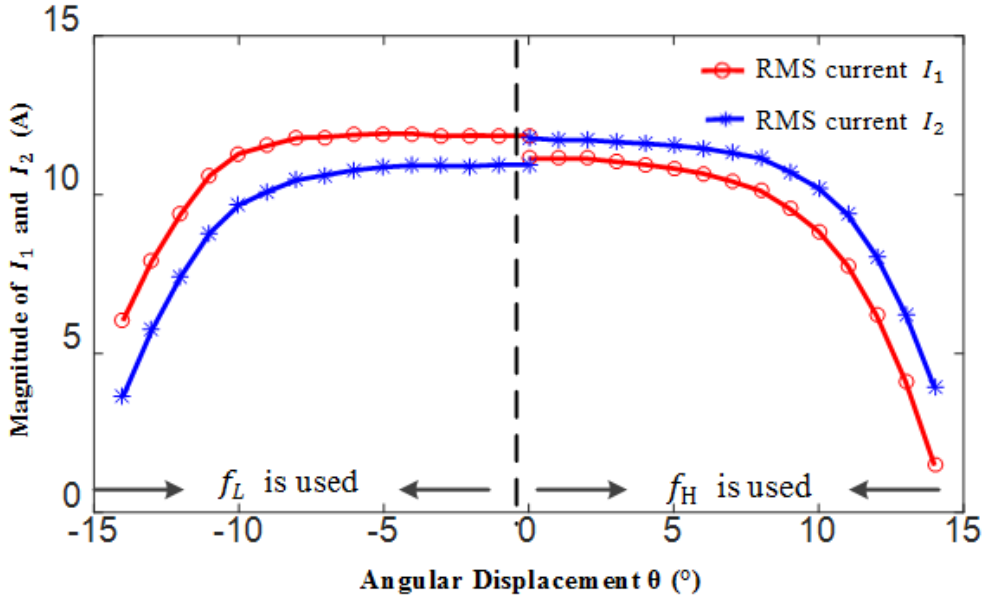

Fig. 3.15. Simulation result from PSIM: the magnitudes of I_1 and I_2 corresponding to different angular displacement θ.

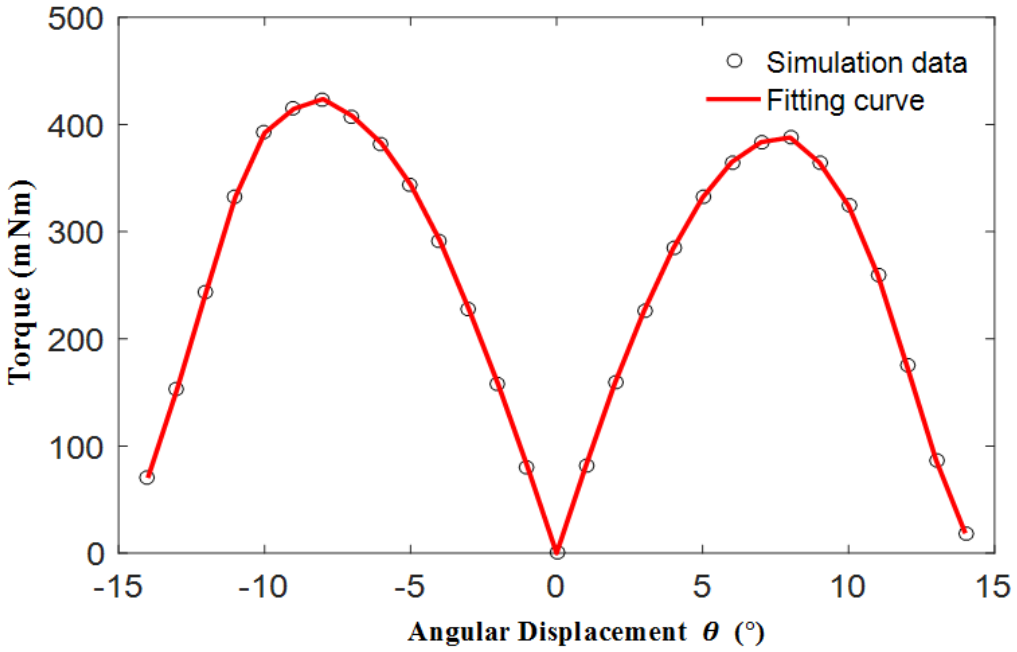

Fig. 3.16. Simulation result from ANSYS Maxwell: the magnitude of average torque corresponding to different angular displacement θ in a pole pair.

The magnitude of the average torque is determined by not only the attenuation coefficient γ and the magnitudes of RMS current I_1 and I_2, but the relative position between the stator resonant circuit and the rotor resonant circuit. As is shown in Fig. 3.16, the magnitude of the average torque corresponding to

different angular displacement θ is further simulated in ANSYS Maxwell based on the data obtained in Fig. 3.13 and 3.15. Fig. 3.16 shows that when the stator and rotor resonant circuits are aligned, i.e. the angular displacement θ is 0°, no torque would be developed. Besides, the maximum attraction force is developed at the angular displacement θ of $-8°$, and the maximum repulsion force is developed at angular displacement θ of 8°. For one pole pair in the proposed MRCM, the maximum value of average torque is around 400 mNm with the input power of about 60 watts.

The magnitude of the simulated torque ripple in a pole pair is relatively large. Nevertheless, the overall torque ripple could be much smaller with the careful manipulation of pole arrangement and control strategy in a multi-pole MRCM.

3.3.3 Transient Process and Steady State

To investigate the transient process of the proposed MRCM, a specific example with the angular displacement θ $\pm 5°$ is presented here. Using the parameters listed in Table 3.1, simulation results are obtained from PSIM.

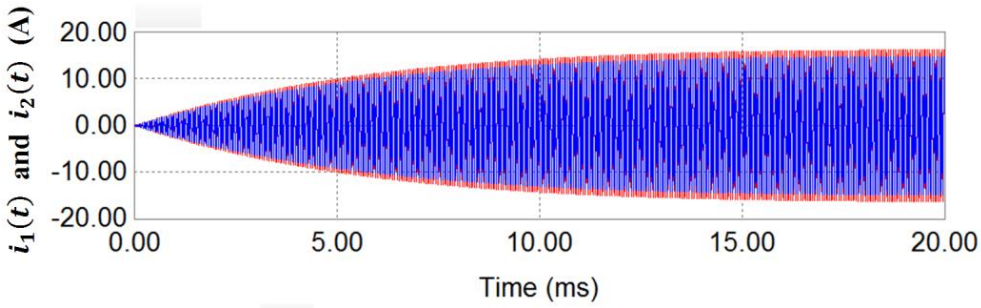

(a)

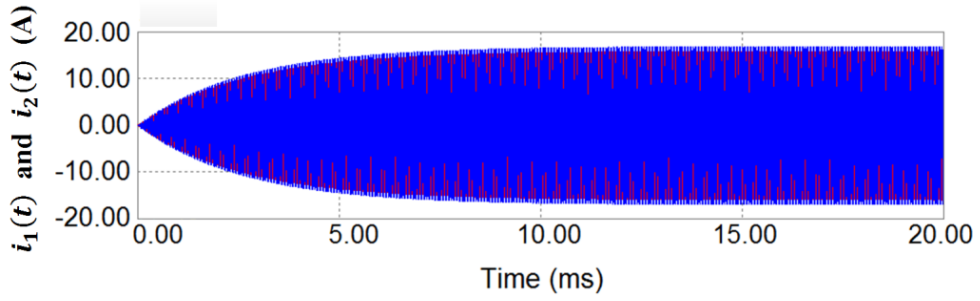

(b)

Fig. 3.17. Simulation result from PSIM: transient process of the currents of red curve $i_1(t)$ and blue curve $i_2(t)$ during the period from 0 ms to 20 ms in PSIM. (b) a lower resonant splitting frequency f_L is used when the angular displacement θ is $-5°$. (b) a higher resonant splitting frequency f_H is used when the angular displacement θ is $5°$.

As is shown in Fig. 3.17, using the lower resonant splitting frequency f_L or higher resonant splitting frequency f_H, the currents $i_1(t)$ and $i_2(t)$ of stator and rotor resonant circuits can reach a steady state with the amplitude of around 16A. Moreover, since the total number of period to reach the steady state is constant, to use the higher resonant splitting frequency f_H could reach the full resonance in a shorter time than to use lower resonant splitting frequency f_L. As tens of period are necessary to reach the full resonance, for different rotational speed, it is essential to select a natural frequency f_0 which can guarantee that the stator and rotor resonant circuit have sufficient time to fulfill the full resonance. In other words, a higher rotational speed demands a higher designed natural frequency f_0 to maintain the full resonance.

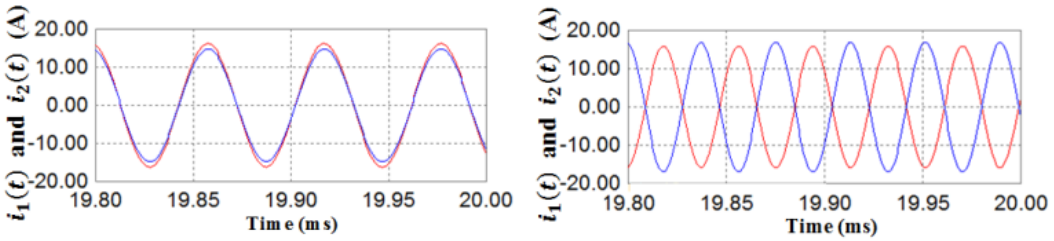

Fig. 3.18. Simulation result from PSIM: steady state of the currents of red curve $i_1(t)$ and blue curve $i_2(t)$ during the period from 19.8 ms to 20 ms. (a) a lower resonant splitting frequency f_L is used when the angular displacement θ is $-5°$. (b) a higher resonant splitting frequency f_H is used when the angular displacement θ is $5°$.

Fig. 3.18 presents a zoom-in view of Fig. 3.19 during the period from 19.8 ms to 20 ms. It is clear to identify that using lower resonant splitting

frequency f_L provides an approximately 0° phase difference δ between $i_1(t)$ and $i_2(t)$, while using higher resonant splitting frequency f_L provides an approximately 180° phase difference δ between $i_1(t)$ and $i_2(t)$.

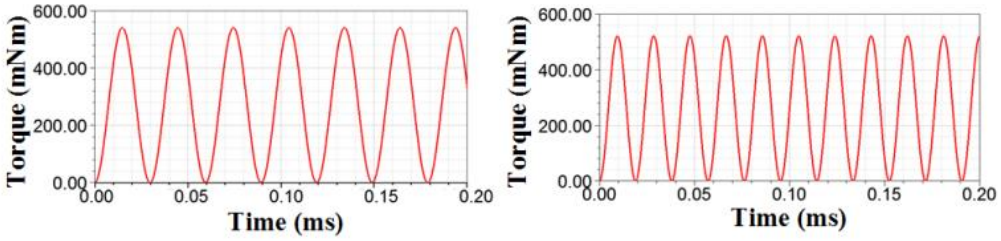

(a) (b)

Fig. 3.19. Simulation result from ANSYS Maxwell: steady state of torque corresponding to Fig. 3.18. (a) a lower resonant splitting frequency f_L is used when the angular displacement θ is $-5°$. (b) a higher resonant splitting frequency f_H is used when the angular displacement θ is $5°$

Based on the magnitude of currents $i_1(t)$ and $i_2(t)$, a transient simulations in ANSYS Maxwell are conducted to perform the torque estimation. Fig. 3.19 (a) demonstrates the simulated torque when a lower resonant splitting frequency f_L is used at the angular displacement θ of $-5°$. The average torque is calculated to be 344 mNm. Besides, when a higher resonant splitting frequency f_H is used at the angular displacement θ of $5°$, the average torque is calculated to be 331 mNm as shown in Fig. 3.19 (b). These average torque values are the same as the data shown in Fig. 3.16. Above transient and steady state simulations have further verified the feasibility of the proposed MRCM.

3.3.4 *Simulation Results of a Complete MRCM*

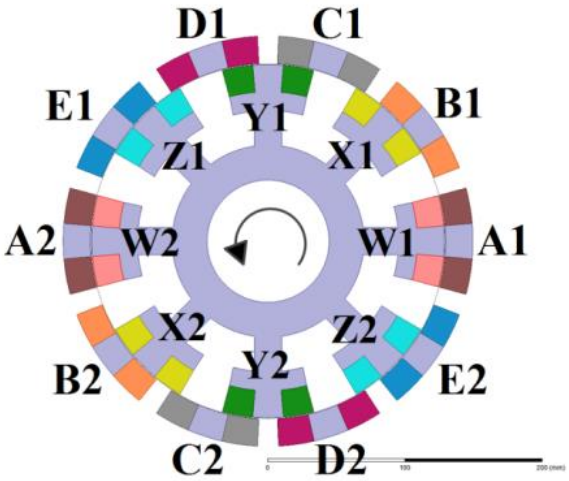

Fig. 3.20. Simulation model of the proposed MRCM in ANSYS Maxwell when the rotation angle is 0°.

Based on design parameters detailed in Table 3.1, a MRCM simulation model, consisting of 10 stator poles and 8 rotor poles, is developed in ANSYS Maxwell. As shown in Fig. 3.20, the 10 stator poles are divided into 5 phases (A, B, C, D and E) while the 8 rotor poles are divided into 4 phases (W, X, Y, Z). With the proposed pole arrangement, the excitation sequence is well manipulated such that each stator phase would have a working range of 9° rotation angle with the corresponding angular displacement θ being $-12^{\circ}\sim-3^{\circ}$ for attraction force and $3^{\circ}\sim12^{\circ}$ for repulsion force. The sequence of the effective stator phase is a repetition of the order B-A-E-D-C, and the sequence of the effective rotor phase is a repetition of the order X-W-Z-Y. However, the effective stator and rotor phases would have different combinations depending on the rotor position.

TABLE 3.2

Excitation Sequence for the Proposed Simulation Model of MRCM

Repulsion Force Using Higher Resonant Splitting Frequency f_H:							
Rotation Angle	0 °–3 °	3 °–12 °	12 °–21 °	21 °–30 °	30 °–39 °	39 °–48 °	48 °–57 °
Effective Stator Phase	B	A	E	D	C	B	A
Effective Rotor Phase	X	W	Z	Y	X	W	Z

Attraction Force Using Lower Resonant Splitting Frequency f_L:							
Rotation Angle Phase	0°–6°	6°–15°	15°–24°	24°–33°	33°–42°	42°–51°	51°–57°
Effective Stator Phase	E	D	C	B	A	E	D
Effective Rotor	Z	Y	X	W	Z	Y	X

Besides, as shown in Table 3.2, at each time instant only two nonadjacent stator phases are powered to generate rotational force, where one stator phase produces repulsion force using higher resonant splitting frequency f_H, the other stator phase produces attraction force using lower resonant splitting frequency f_L. Specifically, when the rotation angle is 0° as demonstrated in Fig. 3.20, the angular displacement θ between stator phase B and rotor phase X is 9°, and a specific higher resonant splitting frequency f_H is used to power stator phase B to generate repulsion force. The angular displacement θ between stator phase E and rotor phase Z is 9°, and a specific lower resonant splitting frequency f_L is used to power stator phase E to generate attraction force.

Considering the large torque ripple in one pole pair as shown in Fig. 3.19, the excitation for two poles (B1 and B2) of stator phase B would have a phase different of $\frac{\pi}{2}$ to reduce the torque ripple: $V\sin(2\pi f_H t)$ and $V\sin(2\pi f_H t + \frac{\pi}{2})$. Similarly, the excitation for two poles (E1 and E2) of stator phase E would also have a phase different of $\frac{\pi}{2}$ to reduce the torque ripple: $V\sin(2\pi f_L t)$ and $V\sin(2\pi f_L t + \frac{\pi}{2})$.

When the rotor speed is 1,000 rpm, the simulation result of output torque is obtained as shown in Fig. 3.21. Compared to the simulated torque in one pole pair as shown in Fig. 3.16, the torque ripple in Fig. 3.21 is reduced significantly. The torque ripple could be further reduced by using more number of poles and more sophisticated control strategy. More simulation results are presented in Table 3.3.

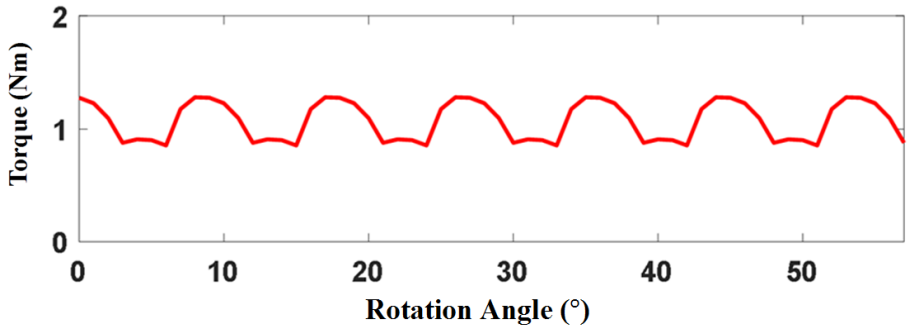

Fig. 3.21. Simulation results of proposed MRCM from ANSYS Maxwell: output torque for different rotation angle.

TABLE 3.3
Simulation Results of Machine Outputs

Parameters	Values
rotor speed	1000 rpm
input power	305.44 W
power factor	1
average output torque	1.0678 Nm
torque ripple	39.32%
efficiency	36.61%
output power density	2.96 W/kg

3.3.5 Comparison with Conventional Induction Motor

While to the best of author's knowledge there is no existing coreless and magnetless motor available for comparison, it would be difficult and unfair to make a thorough comparison between a coreless and magnetless electric motor and a conventional induction motor with cores in high permeability. Instead, a simple comparison with a conventional induction motor using ANSYS Maxwell simulation is provided here to further illustrate the relative merits of the proposed MRCM.

The drive system of the proposed MRCM is similar to the one for conventional electric motors consisting of an AC/DC rectifier, a DC bus, a DC/AC inverter and a controller with the main differences of requiring (1) a

higher switching frequency to enable the efficient wireless power transfer between stator resonant circuits and rotor resonant circuits, and (2) a high revolution encoder and a fast digital controller to track the rotor-position-dependent excitation frequency. Therefore, for the same power level, their weight would be comparable while the power losses in the drive of the conventional induction motor would be smaller due to its lower switching frequency.

A 2D simulation model of a conventional induction motor as shown in Fig. 3.22 was developed with specifications comparable to the proposed MRCM. Table 3.4 lists the design parameters of this conventional induction motor including 2D model specifications and rated parameters.

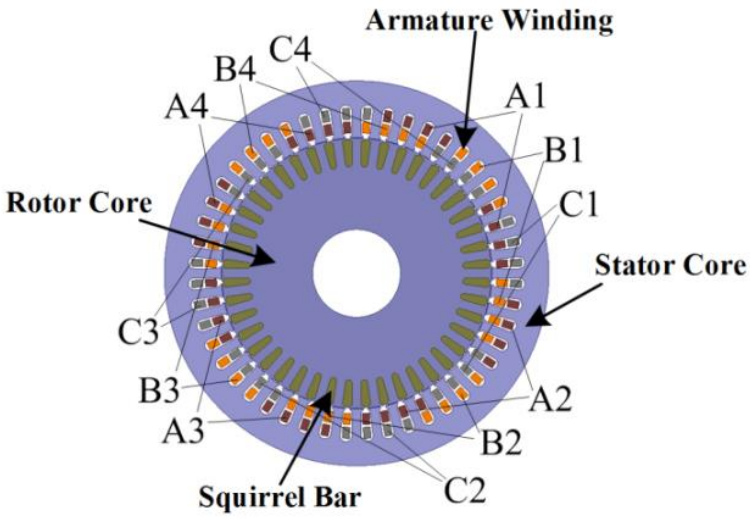

Fig. 3.22. Simulation model of the conventional induction motor in ANSYS Maxwell.

For comparison purpose, the operating conditions of the conventional induction motor were adjusted to be comparable to the proposed MRCM with same input power of 305 W and rotor speed of 1000 rpm. The efficiency, power factor and output power density of conventional induction motor were then obtained. Besides, with the same output torque, the torque ripple percentage is calculated by using the simulation result as is shown in Fig. 3.23. Table 3.4

summaries the quantitive comparison between the proposed MRCM and the conventional induction motor.

TABLE 3.4

Design Parameters of Conventional Induction Motor

Parameters	Values
2D Model Specifications	
model depth	200 mm
outer radius of stator	150 mm
outer radius of rotor	111.5 mm
length of air gap	1 mm
number of stator slots	48
number of rotor bars	44
number of phases	3
number of stator pole pairs	2
turns of stator conductors	15
core material	MG19_24
phase resistance	0.67 Ω
phase inductance	0.23 mH
estimated weight	73.8 kg
Rated Parameters	
input power	8.41 kW
input voltage	310.27 V
excitation frequency	50 Hz
rotation speed	1453.66 rpm
torque	49.22 Nm
efficiency	89.1%
power factor	0.93
output power density	101.53 W/kg

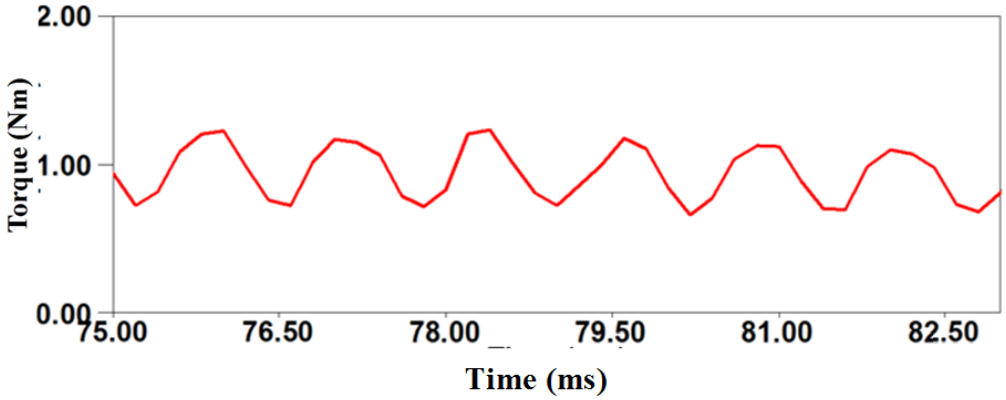

Fig. 3.23. Simulation results of conventional induction motor from ANSYS Maxwell: output torque at steady state.

TABLE 3.5

Comparison between Proposed MRCM and Conventional Induction Motor

Parameters	Proposed MRCM	Conventional Induction Motor
efficiency	36.61 %	73.52 %
power factor	1	0.896
output power density	2.96 W/kg	3.04 W/kg
torque ripple	39.32 %	60.41 %

From Table 3.5, it can be concluded that one of the promising characteristics of proposed MRCM is the inherent unity power factor. With a similar output torque, the torque ripple percentage of the proposed MRCM is smaller than the convention induction motor. Besides, the output power density of the proposed MRCM is almost the same as the conventional induction motor. However, the efficiency of the proposed MRCM, which is defined as the ratio between the output power generated by the rotating force and the input power, is significantly lower than the conventional induction motor, mainly due to the compromise for the proposed coreless design. Nevertheless, this can be improved by making full

use of rotor space, reducing the conductor resistance, and especially employing suitable cores with high permeability.

3.4 Summary

This chapter presents a novel MRCM. Due to the coreless and magnetless design, the proposed MRCM has the following merits including lighter in weight, no core loss and no flux saturation problem. As an elementary and essential part of the proposed MRCM, a pole pair is analyzed elaborately in terms of the selection of resonant topology, the force magnitude and direction, and the frequency splitting phenomenon. Besides, the underlying operation principle has been developed from the perspective of a pole pair. Following the proposed design procedures, the feasibility of the proposed MRCM is fully validated using computer simulations in MATLAB, PSIM and ANSYS Maxwell. A rough comparison with the conventional induction motor was provided to further illustrate the relative merits of the proposed MRCM. Simulation results obtained so far are encouraging and the proposed MRCM could well be a promising start for a new generation of future electric motor. Further research could focus on the optimization of the motor structure and pole ratio as well as the realization of sophisticated position tracking and frequency control. Furthermore, it is possible to enhance the proposed MRCM by employing suitable cores material with high permeability. As the proposed MRCM is lighter in weight than conventional electric motors, the potential application of the proposed MRCM could be in the aerospace industry. As a summary, the proposed MRCM is a new electric motor, which still requires further enhancements on its design and control, but could be a start of a promising electric motor based on the proposed MRCM.

Chapter IV

Single-Vector-Based Model Predictive Direct Speed Control with Compensation Factors for PMSM Drives

4.1 Introduction

As is analyzed in Chapter II, conventional DTC has poor speed response and large torque ripple. MPTC can mitigate the torque ripple, but the speed response is still unsatisfactory. In this chapter, an improved MPDSC strategy is proposed for PMSM drives. The proposed MPDSC strategy is a PI-free control strategy, and has a superior speed tracking capability with very small speed offset and ripple. Moreover, by integrating some compensation factors in the cost function, the torque ripple is regulated and minimized effectively. Compared to conventional DTC and MPTC, the proposed MPDSC strategy has an overall better performance in terms of speed ripple, torque ripple, current THD and switching frequency.

This chapter is organized as follows. In section 4.2, an on-line load torque observer is firstly introduced to estimate load torque. An overshoot mitigation method is then proposed to regulate the torque within the permissible range and avoid large oscillations. Besides, a myopic prediction is discussed, and a correction method is proposed to enhance the dynamic and steady state responses. For the validation of the proposed MPDSC strategy, section 4.3 presents simulation results of load torque observer, the overshoot mitigation and the correction of myopic prediction. Moreover, a comparison between conventional DTC and FOC is conducted to show the superiority of the proposed MPDSC.

Hardware-in-the-loop (HIL) experimental results are presented in section 4.4, and this chapter is concluded with a summary in section 4.5.

4.2 Proposed Single-Vector-Based MPDSC strategy

Fig. 4.1 illustrates the DTC strategy. The torque reference from the outer speed loop, together with the flux reference, are compared with the actual values. Then, the torque and flux errors are delivered to two fixed band hysteresis comparators to produce digitized signals d_T and d_φ. Finally, the voltage vector is selected from a predefined switching table according to d_T, d_φ and the position of state flux. For conventional cascade speed loop control methods, such as FOC, conventional DTC and even model predictive DTC (MPDTC), real-time reference of electromagnetic torque T^* is generated from the PI unit, whose input is the speed error ω_{error} between the reference speed ω^* and the measured speed ω.

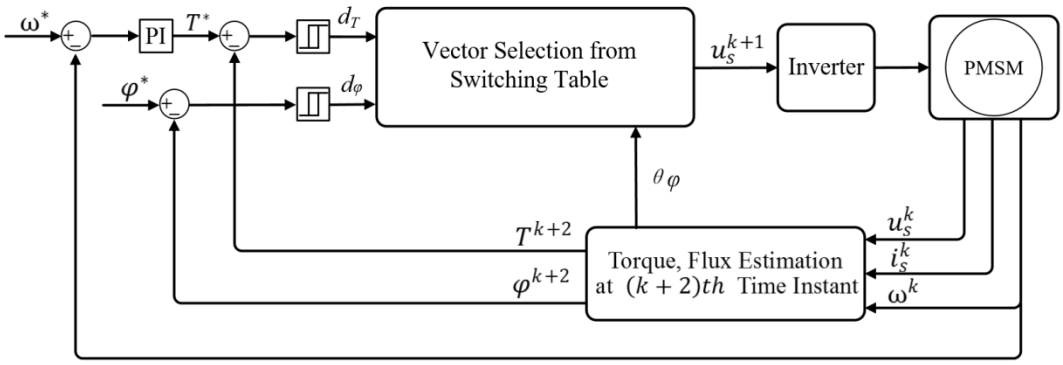

Fig. 4.1. Traditional DTC with outer speed control loop.

This section presents the proposed single-vector-based MPDSC strategy. After the formation of the cost function, the speed prediction procedures, the estimation of load torque, the torque mitigation and the correction of myopic prediction are developed to enhance the tracking capability of speed and load, as well as to reduce the torque oscillation. The overall control diagram of the proposed single-vector-based MPDSC strategy is shown in Fig. 4.2.

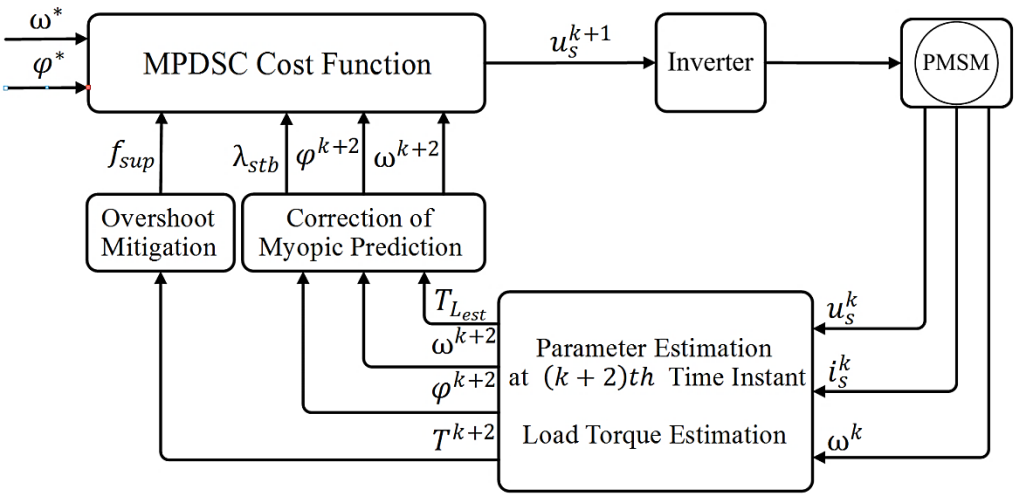

Fig. 4.2. Control diagram of the proposed single-vector-based MPDSC.

Different from the conventional MPDTC strategy, the main control objective for the proposed single-vector-based MPDSC strategy is the motor speed. By integrating the outer speed loop into the MPC strategy, such cascade linear structure with PI controllers can be eliminated. Consequently, a speed error ω_{error}, rather than the torque error T_{error}, is formulated in the cost function as

$$\omega_{error} = |\omega - \omega^*| \tag{4.1}$$

The speed error ω_{error} is minimized in the cost function, and hereby the optimal voltage vector is selected to approach the predefined speed reference ω^*. As the speed error ω_{error} is directly used in the control algorithm, the PI unit is avoided in the control loop. The tuning process of PI parameters is therefore eliminated.

The speed error ω_{error} involved in the cost function contributes to regulate the speed, and thus, the stator currents need to be controlled separately. Since the quality of stator currents can be indirectly controlled through stator flux, a stator flux error φ_{error} is included in the cost function to improve the quality of stator currents.

$$\varphi_{error} = |\varphi - \varphi^*| \tag{4.2}$$

The two dominating elements in the cost function, motor speed and flux, are defined in (4.13) and (4.14) respectively. The speed reference can be changed

flexibly, depending on the requirement in actual application. The flux reference is usually determined to follow maximum torque per ampere to achieve high efficiency. The information of flux determination is provided in section 2.2.5.

4.2.1 Speed and Flux Prediction

As the motor controller needs time to conduct the calculation, the optimal voltage vector cannot be applied to the PMSM immediately after the sampling process. A one-step delay is inevitable, which deteriorates the control performance without any compensation. The one-step compensation is therefore necessary in the motor control. With the consideration of one-step delay, the future speed ω^{k+2} and flux φ^{k+2} at $(k+2)th$ time instant can be predicted based on present states of the machine and the possible control behaviors. The optimal voltage vector applied at the $(k+1)th$ time instant is then determined by the speed error ω_{error}^{k+2} and flux error φ_{error}^{k+2}. The procedures of the parameter estimation for one-step delay compensation are depicted in the diagram as shown in Fig. 3.

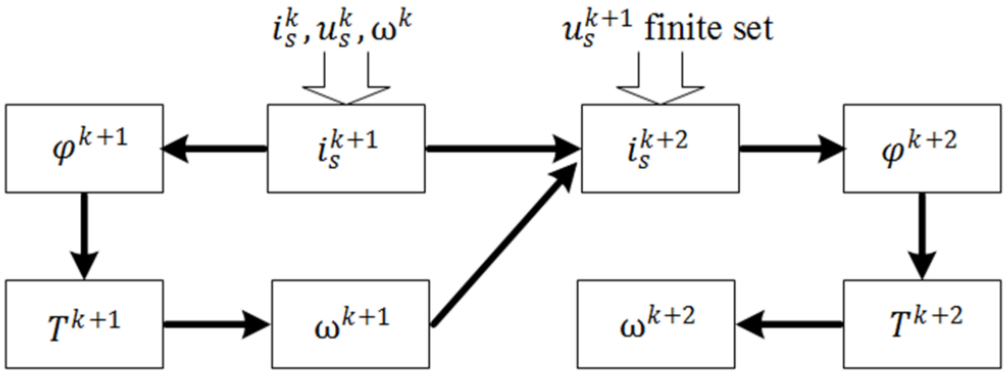

Fig. 4.3. Procedures of the parameter estimation.

Assuming that the sampling of $\boldsymbol{i}_s^k$, $\boldsymbol{u}_s^k$ and ω^k is conducted at and a suitable voltage vector $\boldsymbol{u}_s{}^k$ has been selected as the motor input at kth time instant, the stator current at the $(k+1)th$ time instant can be predicted as

$$i_d^{k+1} = i_d^k + T_s\left(-\frac{R_s}{L_d}i_d^k + \frac{\omega^k L_q}{L_d}i_q^k + \frac{1}{L_d}u_d^k\right) \tag{4.3}$$

$$i_q^{k+1} = i_q^k + T_s\left(-\frac{\omega^k L_d}{L_q} i_d^k - \frac{R_s}{L_q} i_q^k + \frac{1}{L_q} u_q^k - \omega^k \varphi_f\right) \tag{4.4}$$

Then, the stator flux and electromagnetic torque at the $(k+1)th$ time instant can be estimated as

$$\varphi_d^{k+1} = L_d i_d^{k+1} + \varphi_f \tag{4.5}$$

$$\varphi_q^{k+1} = L_q i_q^{k+1} \tag{4.6}$$

$$T^{k+1} = \frac{3}{2} p(\varphi_d^{k+1} i_q^{k+1} - \varphi_q^{k+1} i_d^{k+1}) \tag{4.7}$$

The speed at $(k+1)th$ time instant is therefore estimated using the mechanical equation

$$\omega^{k+1} = \omega^k + T_s\left(\frac{T^{k+1}}{J} - \frac{T_L}{J} - \frac{\omega^k B_m}{J}\right) \tag{4.8}$$

The estimated parameters at the $(k+1)th$ time instant above, together with the finite set voltage vectors $\boldsymbol{u}_s{}^{k+1} \in \{V_0, V_1, \ldots V_6, V_7\}$, will be used in the procedure of voltage vector selection. The process of the parameter estimation at the $(k+2)th$ time instant is similar to (4.3)-(4.8). With the compensation of one-step delay, the cost function is expressed as

$$g_1 = \omega_{error}^{k+2} + \varphi_{error}^{k+2} \tag{4.9}$$

4.2.2 Prediction of Load Torque

As indicated in (4.8), the motor actual load torque is required to predict the motor speed. As shown in Fig. 4.1, the outer speed control loop with PI unit is commonly used to produce the torque reference. The developed torque reference can reflect and track the variation of load torque. Without the outer speed loop with PI unit, the estimation of the load torque becomes a problem in the proposed MPDSC strategy. An on-line load torque observer based on discrete-time sliding mode control (DSMC) scheme [165] is therefore employed for the purpose of tracking the load torque in a real-time. Considering $\dot{T}_L = 0$ during a short sampling period, the motor equation can be expressed in state-space form as

$$\dot{\boldsymbol{x}}(t) = \mathbf{A}\boldsymbol{x}(t) + \mathbf{B}\boldsymbol{u}(t) \tag{4.10}$$

$$\boldsymbol{y}(t) = \mathbf{C}\boldsymbol{x}(t) \tag{4.11}$$

where $\boldsymbol{x}(t)$=$[T_L \quad \omega]^T$, $\boldsymbol{u}(t) = T$, and

$$\mathbf{A} = \begin{bmatrix} 0 & 0 \\ -\frac{1}{J} & -\frac{B_m}{J} \end{bmatrix}, \mathbf{B} = \begin{bmatrix} 0 \\ \frac{1}{J} \end{bmatrix}, \mathbf{C} = [0 \quad 1]$$

Following the procedures of designing a full-order observer, a load torque observer is developed, in which the load torque can be predicted as

$$\tilde{T}_L = \tilde{z} + K_e\omega \tag{4.12}$$

where

$$\dot{\tilde{z}} = \frac{K_e}{J}(\tilde{z} + K_e\omega + B_m\omega - T) \tag{4.13}$$

where v is the desired pole of $\dot{T}_L$, and a negative value of v is adopted to guarantee the asymptotically stable of $\dot{T}_L$. Besides, the value of $|v|$ should be carefully selected in order to achieve rapid converge without the oscillation. In this motor control system, the value of v is set to -1000 for rapid convergence and good accuracy.

Similar to most industrial drives with torque estimation, the application of the load torque observer here can also reduce the mechanical complexity as well as the manufacture cost of the motor system. More importantly, the on-line load torque observer helps the proposed MPDSC to achieve the rapid and accurate tracking of the speed variation.

4.2.3 Overshoot Mitigation

While the speed and flux can be directly manipulated through the cost function using (21), the electromagnetic torque is indirectly controlled via the predictive speed ω^{k+2} estimated from the electromagnetic torque T^{k+2} and load torque T_L in the mechanical equation (2.10). As there is no restriction on the estimated electromagnetic torque, the selected voltage vector would change the torque and speed sharply during the start-up, speed-down and speed-up instants. As the magnitude of torque and speed could be higher than their rated limit, the motor may not be able to reach the reference speed and torque after some

oscillations. Even worse, such undesired electromagnetic fluctuation of torque and speed may damage the PMSM.

As a remedy, a suppression factor f_{sup} is introduced in the cost function to restrict the selection range of the voltage vector. Considering one-step delay compensation, suppression factor f_{sup} is defined as

$$f_{sup} = \begin{cases} \infty & |T^{k+2}| > T_r \;||\; |i_a| > I_r \\ 0 & |T^{k+2}| \leq T_r \end{cases} \tag{4.14}$$

The function of suppression factor f_{sup} is illustrated as following. When the absolute value of the estimated electromagnetic torque $|T^{k+2}|$ is greater than the rated torque T_r, or the stator current is larger than the rate value, the suppression factor f_{sup} is set to be ∞. In this case, the corresponding voltage vector is excluded from the selection range. On the other hand, if the torque or the stator current is smaller than the rated value, f_{sup} is set to be 0. It means that f_{sup} take no effect on the selection of voltage vectors. The integration of the suppression factor f_{sup} into cost function is essential to guarantee reduction of torque oscillations and stator current within a safety region of the proposed MPDSC strategy.

4.2.4 Correction of Myopic Prediction

Most predictive control methods are based on the motor's mathematical model, and the accuracy of the motor parameters would directly determine the control performance. For example, the differential of L_d and L_q will vary with respect to i_d and i_q respectively. The permanent flux φ_f would vary with the temperature of the permanent magnet. This is widely recognized as one of the common issues in MPC. Another important factor, known as myopic prediction, lacks sufficient discussion and investigation. Different to parameter variation, myopic prediction is a common but intrinsic problem for predictive control methods. This subsection will illustrate the possible reasons of the myopic prediction, and a simple but effective method is proposed to deal with it.

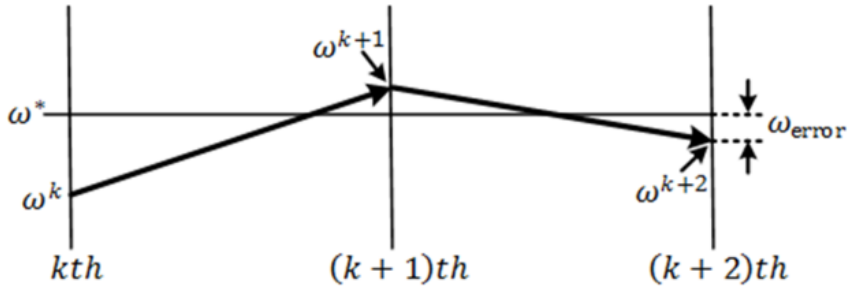

Fig. 4.4. Conventional methods to achieve local optimization.

As is shown in Fig. 4.4, speed values ω^{k+1} and ω^{k+2} are predicted using the one-step ahead information. Considering the compensation of the one-step delay, the speed error ω_{error}^{k+2} at the $(k+2)th$ time instant is used in the cost function to select the optimal voltage vector. The control algorithm enables the drastic change of speed to achieve the minimum ω_{error}^{k+2} at the $(k+2)th$ time instant, without the consideration of the performance after the $(k+2)th$ time instant. More specifically, this process is the local optimization-oriented operation, and the selected voltage vector is the best one only at the $(k+2)th$ time instant. However, for a longer time scale, the selected voltage vector may result in a large torque and speed ripple.

Such process is a myopic prediction, which may deteriorate the transient and steady state control performance. During the start-up or speed change process, myopic prediction will cause large overshoot and oscillations. During the steady state operation, without the compensation of the myopic prediction, flux and torque ripples is relatively large, especially at low sampling frequency. A simple but effective method is proposed to tackle the myopic prediction problem, and to improve the overall prediction as well as the operating performance.

Stability factor λ_{stb} are defined as

$$\lambda_{stb} = \frac{1}{2!}(\omega_{error}^{k+3} + \varphi_{error}^{k+3}) + \frac{1}{3!}(\omega_{error}^{k+4} + \varphi_{error}^{k+4}) \tag{4.15}$$

where

$$\omega_{error}^{k+i} = \omega^{k+1} + (\mathrm{i}-1) * (\omega^{k+2} - \omega^{k+1}) - \omega^*$$

$$\varphi_{error}^{k+i} = \varphi^{k+1} + (\mathrm{i}-1) * (\varphi^{k+2} - \varphi^{k+1}) - \varphi^* \ (i = 3, 4)$$

Considering the calculation burden, only errors at $(k+3)th$ and $(k+4)th$ time instant are included. The weighting coefficient of predictive errors for the $(k+3)th$ time instant and the $(k+4)th$ time instant are $1/2!$ and 1/3! respectively. The magnitude of the weighting coefficient reflects the impact of different time instant. It is obvious that the nearer time instant has higher impact factor for the prediction, and the farer time instant has lower impact factor for the prediction.

With the help of stability factor, it is effective to reduce the adverse impact caused by the myopic prediction. A more forward-looking voltage vector is selected with the consideration of the further performance after the $(k+2)th$ time instant.

With the integration of the one-step delay compensation, the mitigation of torque overshoot and the correction of myopic prediction, the cost function can be formulated eventually as

$$\begin{aligned} min.\, g &= g_1 + f_{sup} + \lambda_{stb} \\ \text{s.t.}\, {u_s}^{k+1} &\in \{V_0, V_1, \dots V_6, V_7\} \end{aligned} \tag{4.16}$$

4.2.5 Overall control strategy

Based on the control diagram of the proposed MPDSC strategy shown in Fig. 1, the whole implementation process can be described as follows.

1) Measurement

In the proposed MPDSC strategy, motor information such as stator currents, voltages and rotor speed needs to be measured. The three-phase stator currents will then be converted to *d*,*q*-components through coordinated transformation.

2) Load torque prediction

The load torque is required in the speed prediction, and the change of load torque should be estimated correctly. An on-line load torque observer is therefore employed to obtain an accurate load torque prediction.

3) MPDSC Controller

The main MPDSC controller essentially consists of two components, namely the prediction model and the cost function. One-step delay compensation is incorporated into the prediction model to predict current, flux, torque and speed at $(k+2)th$ time instant. Besides, the suppression factor and stability factor are integrated into the cost function.

4) Optimal voltage vector determination

The control command with the rotor speed reference and stator flux reference, together with the actual speed and the estimated torque, are sent to the main MPDSC controller to determine the optimum voltage vector to control the PMSM.

5) Pulse Generation

After the voltage vector (i.e. the switching state of the inverter) is selected, PWM gate drives signal can be generated accordingly. Taking $\boldsymbol{V}_2$ (110) as an example, it can be generated by just simply turning on the upper switch and turning off the bottom switch of leg A, and turning on the upper switch and turning off the bottom switch of leg B, and turning off the upper switch and turning on the bottom switch of leg C. Thus, PMSM is powered by three-phase voltages in suitable magnitudes to reach its reference speed and track the load torque.

4.3 Simulation Studying

In this section, the proposed MPDSC strategy is simulated in the environment of MATLAB/Simulink. The parameters of machine and control system are listed in Table 2.1.

Simulations shown in this section are conducted when the sampling frequency is 10 kHz, unless explicitly indicated otherwise. In all presented simulation results, red curves indicate the reference values, while blue curves

refer to actual values. Simulation results of the proposed MPDSC strategy include the performance of load torque observer, overshoot mitigation and correction of myopic prediction. Besides, to investigate the effect of myopic prediction at steady state, more obvious comparative simulation results are presented when the sampling frequency is 5 kHz. Moreover, to reveal the superiority of the proposed MPDSC, a dynamic response of the conventional DTC is involved referred as a comparison counterpart.

4.3.1 Load Torque Observer

The on-line load torque observer with fast and accurate tracking capability of load torque lays the foundation of the proposed MPDSC strategy. The on-line load torque observer is tested as shown in Fig. 4.5. The red curve presents the variation of the reference load torque, and the blue curve is the tracking trajectory of the estimated load torque by the load torque observer. The simulation has validated that the on-line load torque observer performs a rapid and accurate tracking of the load torque variation. Moreover, the rapid and accurate tracking of the load torque variation helps the proposed MPDSC to achieve rapid and accurate tracking of the speed variation. All the remaining simulations employ this on-line load torque observer to estimate the load torque mathematically.

Based on a complete MPDSC algorithm with overshoot mitigation and correction of myopic prediction, Fig. 4.6 shows the dynamic response with step changes in the load torque. A step change of the load results in a transient speed decrease. However, the proposed MPDSC strategy is capable to achieve the new speed tracking in a very short time with very small speed offset, which has validated that the proposed MPDSC has good speed robustness against the variation of load torque.

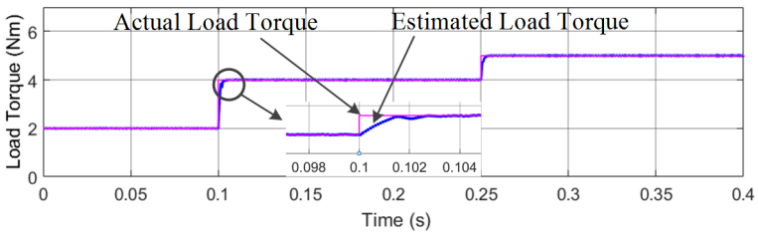

Fig. 4.5. Performance of load torque observer.

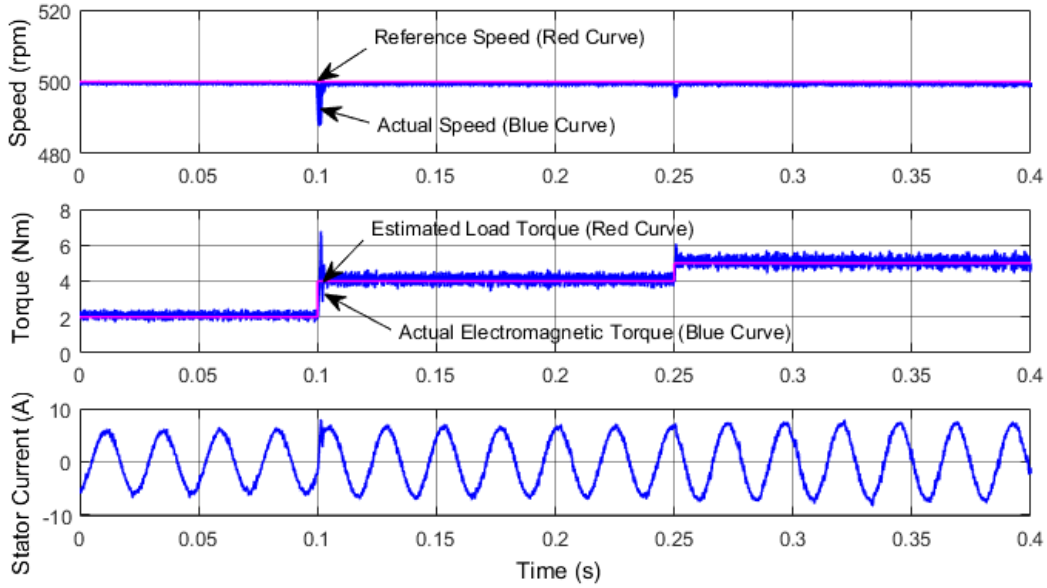

Fig. 4.6. Steady state response of proposed MPDSC strategy with different load torque reference. From top: speed, torque and stator current.

4.3.2 Overshoot Mitigation

Without the mitigation of torque overshoot, the MPDSC algorithm results in huge speed, torque and current ripples, and PMSM cannot achieve a steady state. After integrating the suppression factor f_{sup} into the cost function, the MPDSC algorithm is effective to enable the PMSM to reach reference values of speed and load torque, as is shown in Fig. 4.7. However, during the step change of speed from 500 rpm to 1000 rpm, oscillations of speed and torque are still relatively large. A correction of myopic prediction is therefore proposed to deal with the problem of large oscillation, which will be demonstrated in the next section.

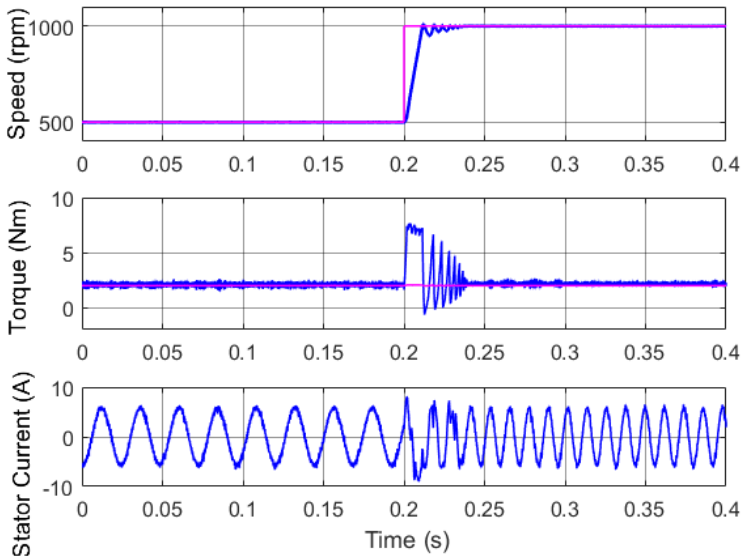

Fig. 4.7. Dynamic response of proposed MPDSC strategy with the overshoot mitigation from 500 rpm to 1000 rpm (Red curves: references; Blue curves: actual values).

4.3.3 Correction of Myopic Prediction

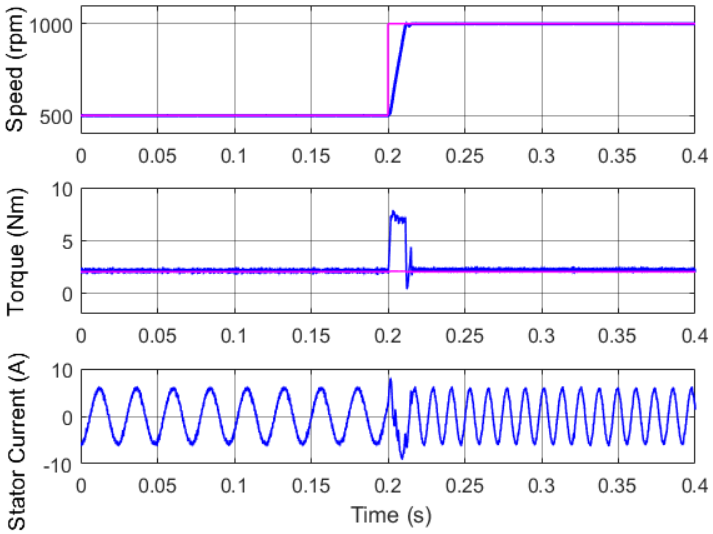

Fig. 4.8. Dynamic response of proposed MPDSC strategy with the correction of myopic prediction from 500 rpm to 1000 rpm (Red curves: references; Blue curves: actual values).

To tackle the above problem of large speed and torque oscillations, a stability factor λ_{stb} is integrated into the cost function to fulfill the correction of myopic prediction. Fig. 4.8 shows the motor performance by using the proposed

correction of myopic prediction. In comparison with Fig. 4.7, the speed and torque oscillations have been mitigated significantly when the speed speeds up from 500 rpm to 1000 rpm.

With regard to the steady state response, applying the correction of myopic prediction is also effective to improve the control performance especially at low sampling frequency. When the sampling frequency is 5 kHz, the steady-state performance with and without the correction of myopic prediction are compared in Fig. 4.9 and 4.10.

Comparing Fig. 4.9 and 4.10, it is seen that the torque ripple of the proposed MPDSC strategy with the correction of myopic prediction is much smaller than the one without the correction of myopic prediction. Table 4.1 presents a quantitative comparison for the proposed MPDSC strategy with and without the correction of myopic prediction. A corresponding bar curve is depicted as is shown in Fig. 4.11. It is seen that, with the correction of the myopic prediction, the speed ripple ω_{ripple}, torque ripple T_{ripple} and current THD can be reduced greatly. Besides, the switching frequency can be reduced to some extent when the correction of myopic prediction is employed. The comparison data have validated that the correction of myopic prediction is helpful to enhance the control performance.

TABLE 4.1

Comparison of proposed MPDSC strategy with and without the correction of myopic prediction at 5kHz Sampling Frequency

MPDSC strategy	ω_{ripple} (rpm)	T_{ripple} (Nm)	Current THD (%)	f_{sw} (kHz)
With the correction of myopic prediction	0.4861	0.2676	21.02	2.70
Without the correction of myopic prediction	0.7360	0.3680	26.26	3.04

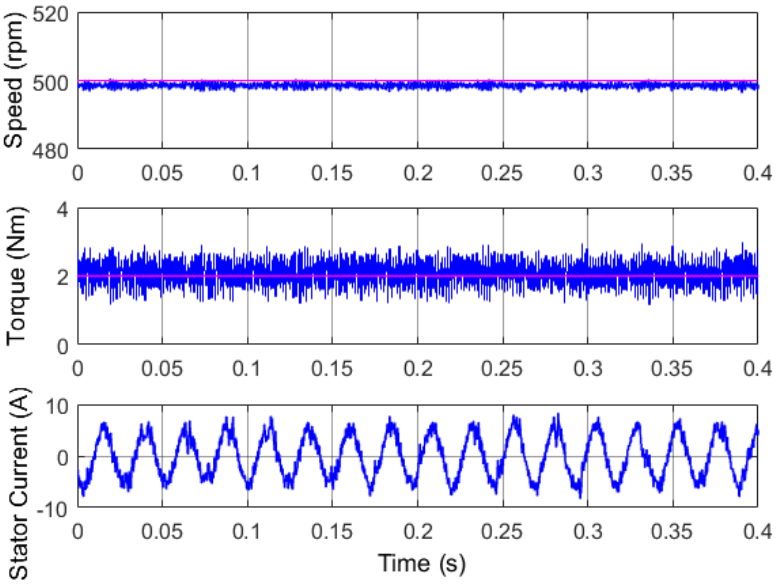

Fig. 4.9. Steady state response of proposed MPDSC strategy without the correction of myopic prediction from 500 rpm to 1000 rpm when the sampling frequency is 5 kHz (Red curves: references; Blue curves: actual values).

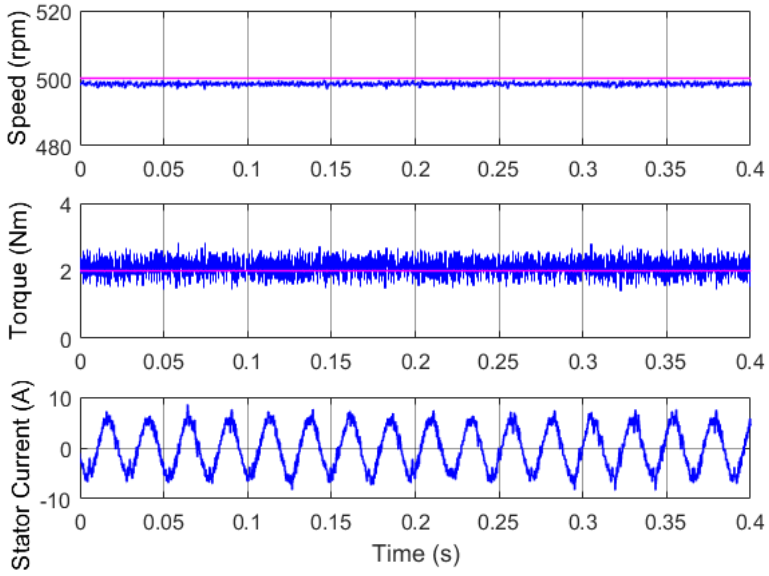

Fig. 4.10. Steady state response of proposed MPDSC strategy with the correction of myopic prediction from 500 rpm to 1000 rpm when the sampling frequency is 5 kHz (Red curves: references; Blue curves: actual values).

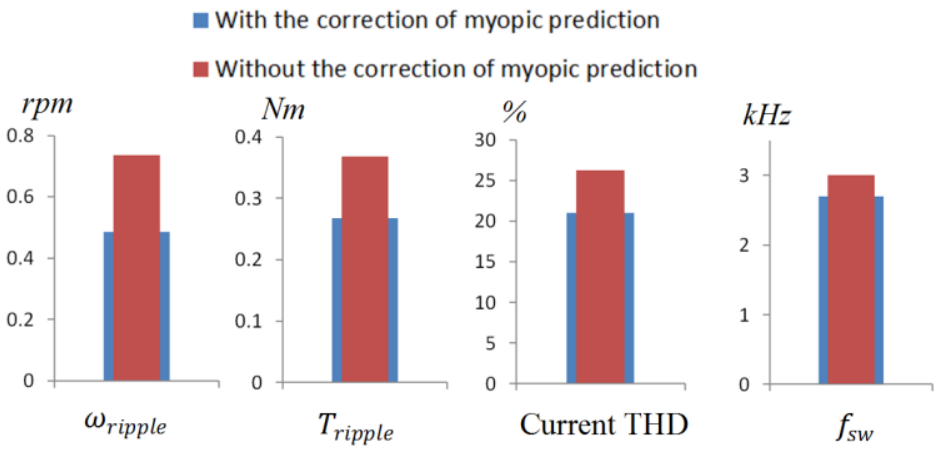

Fig. 4.11. Bar graph for the comparison of current THD, speed ripple ω_{ripple}, torque ripple T_{ripple}, and average switching frequency f_{sw} for proposed MPDSC strategy with and without the correction of myopic prediction.

4.3.4 Comparison with Conventional DTC and FOC

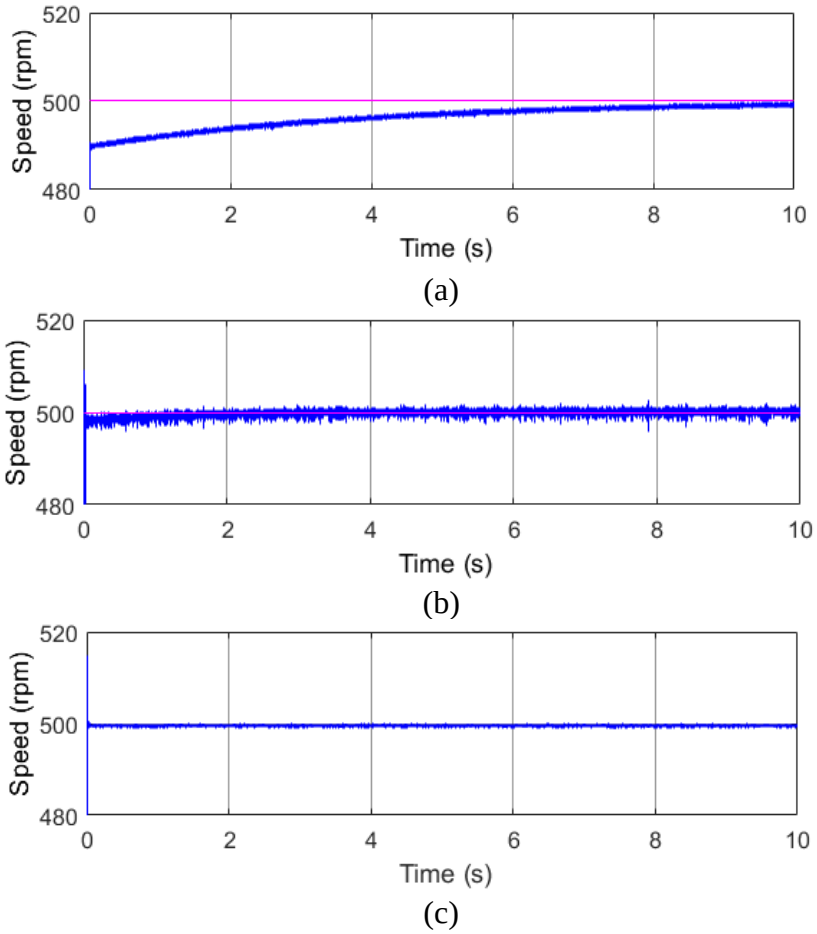

Fig. 4.12. Comparison of speed performance. (a) Conventional DTC (P=2, I=0.5). (a) Conventional DTC (P=5, I=3.5). (c) Proposed MPDSC strategy.

Fig. 4.12 shows the speed performance of the conventional DTC and the proposed MPDSC strategy at 500 rpm. It can been observed that, by using conventional DTC method, a large speed offset (about 15%) between the actual value and the reference can be generated. Although the speed tracking performance of the conventional DTC can be improved to some extent through the adjustment of PI parameters, such process, however, is complicated and time-consuming, and PI parameters have inferior robustness with the variation machine parameters. Moreover, the speed tracking capability of the conventional DTC depends on the cascaded speed loop with PI unit. On the contrary, the actual speed can track the reference tightly by using proposed MPDSC strategy. This excellent speed control capability makes it very suitable in servo drives where high speed accuracy is required.

To obtain a quantitative and intuitive comparison, the current THD, speed ripple ω_{ripple}, torque ripple T_{ripple}, and average switching frequency f_{sw} are listed in Table 4.2, and a bar graph is depicted in Fig. 4.13, respectively. It is obvious that the proposed MPDSC strategy is superior than the conventional DTC in all four aspects.

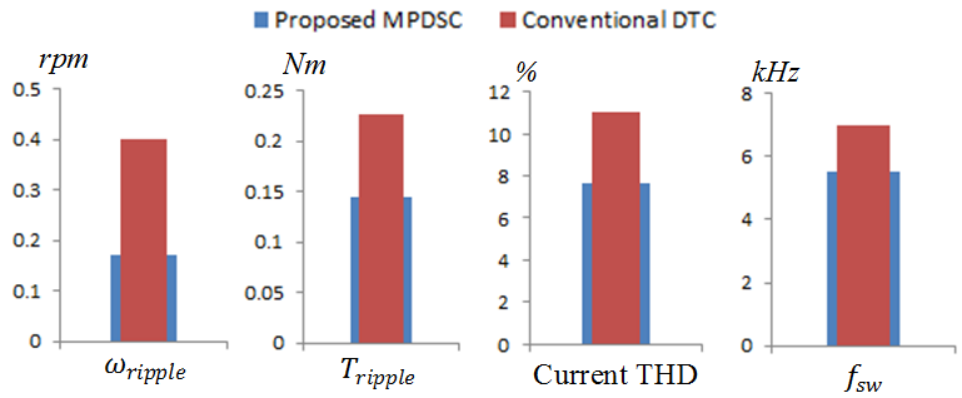

Fig. 4.13. Bar graph for the comparison of current THD, speed ripple ω_{ripple}, torque ripple T_{ripple}, and average switching frequency f_{sw} between proposed MPDSC strategy and conventional DTC.

TABLE 4.2

Comparison between proposed MPDSC strategy and conventional DTC at 10kHz Sampling Frequency

Method	ω_{ripple} (rpm)	T_{ripple} (Nm)	Current THD (%)	f_{sw} (kHz)
Proposed MPDSC strategy	0.1701	0.1438	7.63	5.5
Conventional DTC	0.4018	0.2274	11.07	7

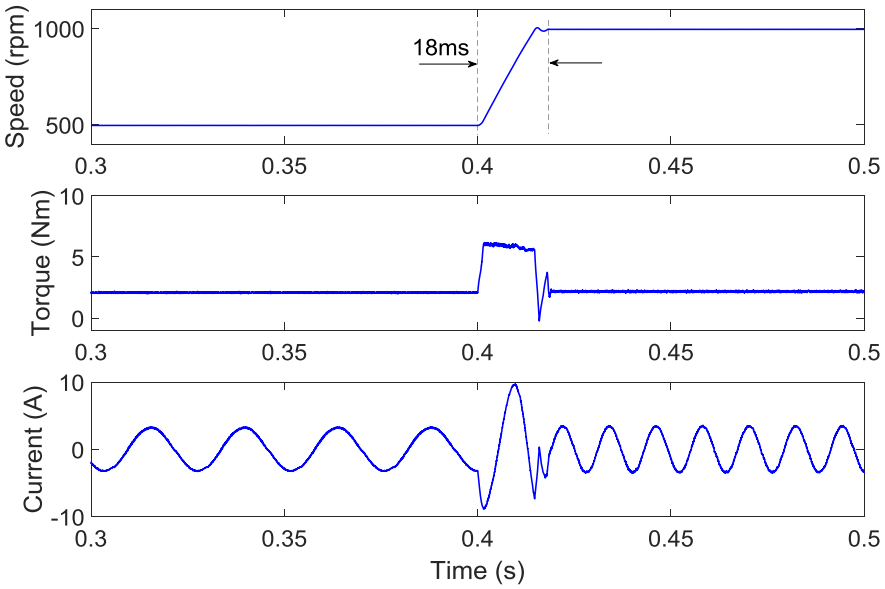

Fig. 4.14.Dynamic performance of FOC at f_{sw}=10kHz.

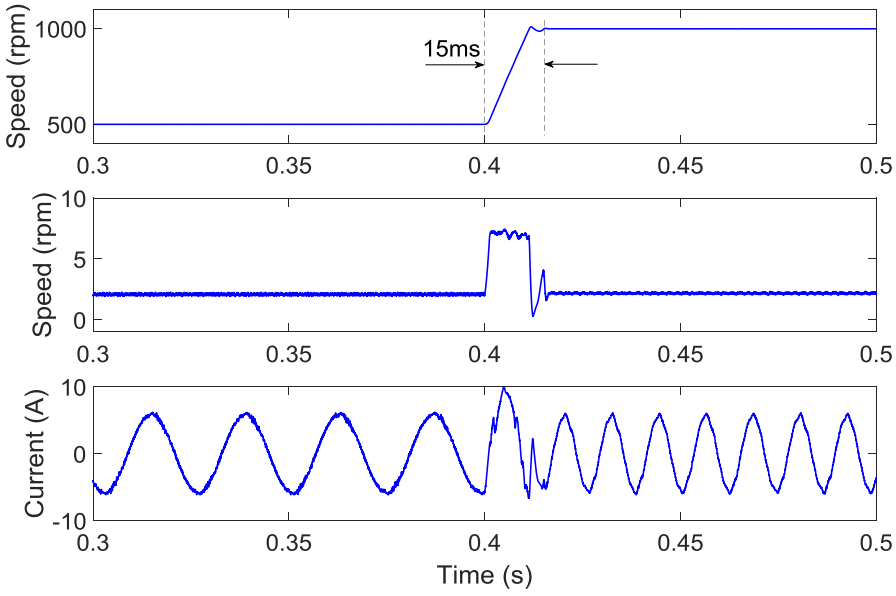

Fig. 4.15. Dynamic performance of MPDSC at f_{sw}=10kHz.

The comparison between a typical FOC and the proposed MPDSC both at 10kHz sampling frequency is presented in Fig. 4.14 and Fig. 4.15. Both methods show accurate and fast speed control capability. It takes about 18ms for FOC to reach new steady state, and it takes about 15ms for MPDSC to achieve this goal. It is worth mentioning here that different stator current amplitudes are attributed to different fluxes by using different control methods under the same load torque.

4.3.5 Robustness against Parameter Variations

Due to the variations in operating condition like temperature, the motor parameters can vary. Then, the motor drive system may become unstable if the parameters used in the control are different to the actual values. Therefore, parameter sensitivity is a significant concern in practical implementation. To evaluate the robustness against parameter variation, Fig. 4.16 shows the performance of different control methods in which the stator inductance is smaller than the actual value by 20%. Specifically, L_q is changed from 20mH to 16mH in the control algorithm at 0.2s. It can been observed that both conventional DTC and MPDTC result in a speed offset between the actual value and the reference, and the speed offset becomes larger after 0.2s. This means that DTC and MPDTC are affected easily by the accuracy of the machine parameters. Although the speed tracking performance of the conventional DTC and MPDTC can be improved to some extent through the adjustment of PI parameters. Such process, however, is complicated and time-consuming. On the contrary, the actual speed can track the reference tightly by using the proposed MPDSC strategy. This excellent speed control capability makes it very suitable in servo drives where high speed accuracy is required. To obtain a better observation, the speed error against different stator inductance variations is shown in Fig. 4.17. The result reveals that, for DTC and MPDTC, the speed control accuracy is deteriorated considerably when the machine parameters vary. On the other hand, the MPDSC presents better parameter-independent capability in speed control.

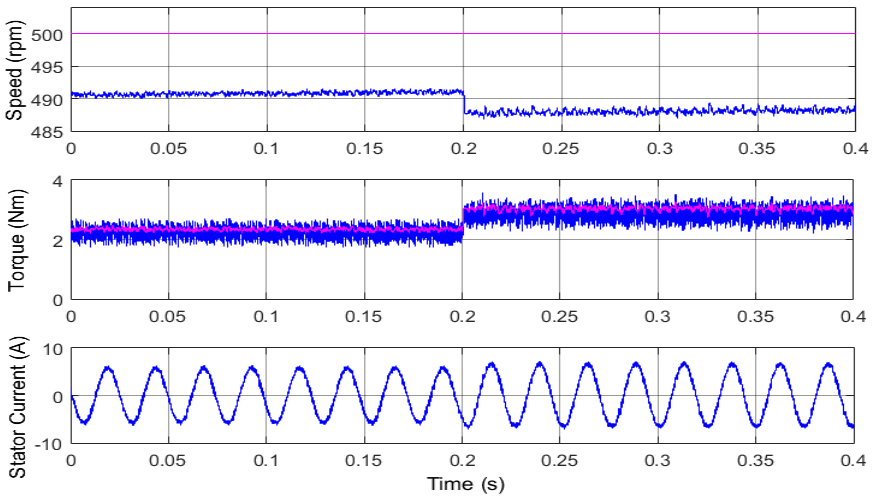

(a)

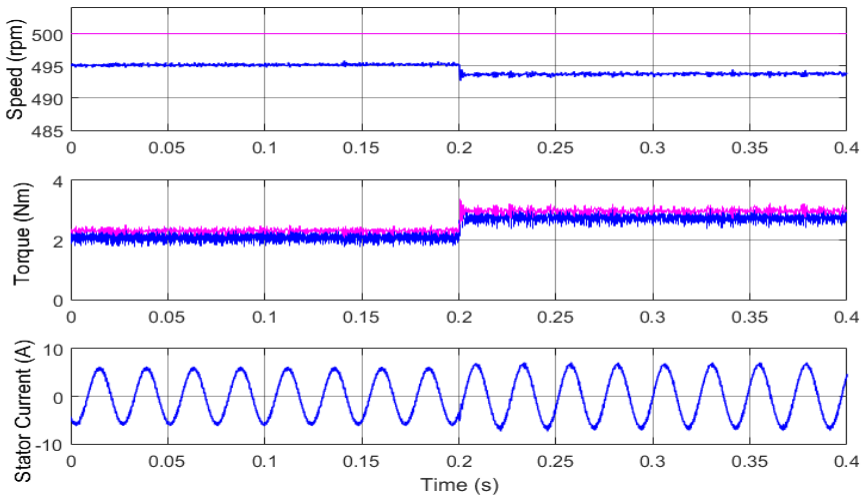

(b)

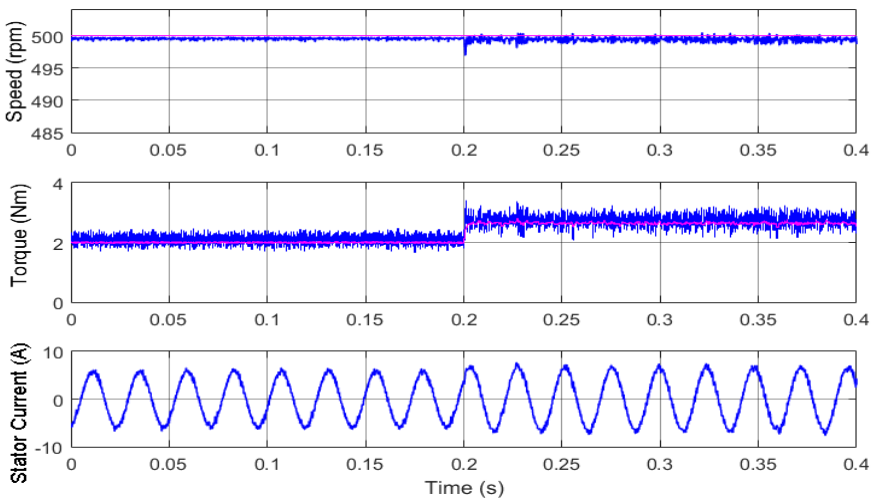

(c)

Fig. 4.16. Comparison of speed, torque and stator current with 20% L_q deviation (L_q=16mH) when the sampling frequency is 10 kHz (a) conventional DTC (P=2, I=0.5). (b) MPDTC (P=2, I=0.5). (c) Proposed MPDSC.

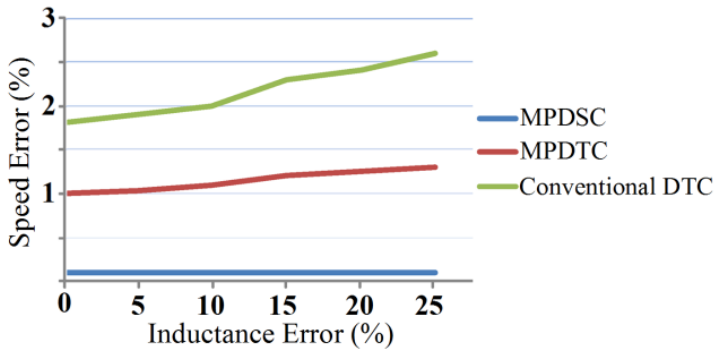

Fig. 4.17. Comparison of speed error against inductance error for conventional DTC (P=2, I=0.5), MPDTC (P=2, I=0.5), and proposed MPDSC.

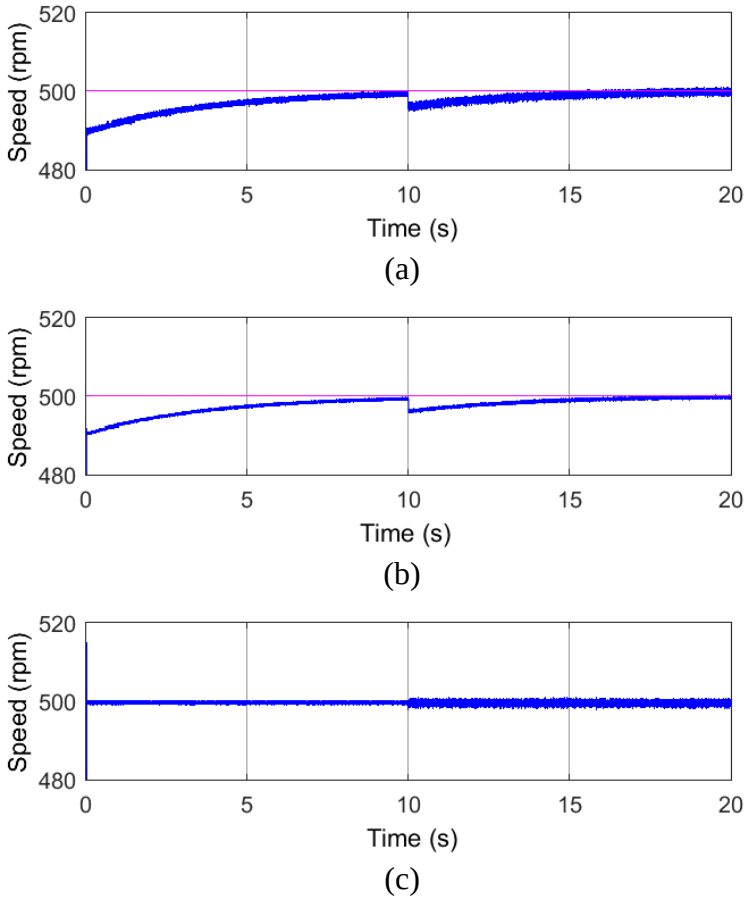

Fig. 4.18. Complete waveforms of speed response with 20% L_q deviation (L_q=16mH) when the sampling frequency is 10 kHz. (a) Conventional DTC (P=2, I=0.5). (b) MPDTC (P=2, I=0.5). (c) Proposed MPDSC.

To obtain a clearer comparison in a longer duration of 20s, the complete waveforms of speed response in Fig. 4.16 have now been shown in Fig. 4.18. It is seen that the motor speed by using MPDSC can track the reference tightly before

and after the parameter variation. On the other hand, obvious speed errors by using DTC and MPDTC are observed in both start-up and parameter variation processes.

4.4 Hardware-in-the-Loop Test

The proposed MPDSC strategy is further verified using HIL tests. As is shown in Fig. 4.19, the experimental setup consists of the devices including the RTlab with OPAL-RT OP5700 simulator, a DSP with F28335 chip, a laptop and an oscilloscope.

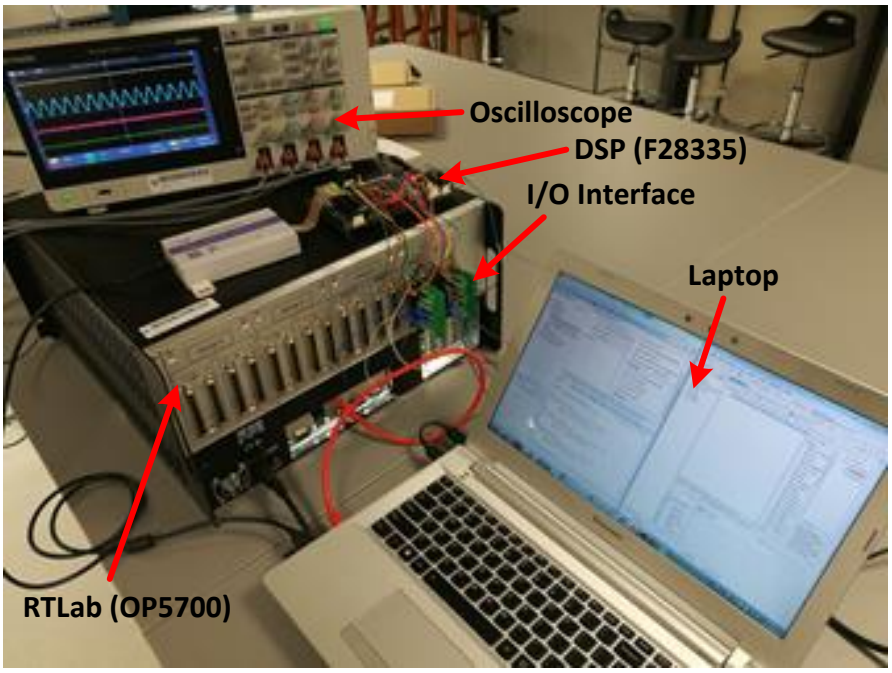

Fig. 4.19. HIL testbed for the verification of the proposed single-vector-based MPDSC strategy.

The DC bus, inverter and PMSM are modeled in the RTlab, and RTlab offers an I/O interface for the communication with the DSP. Through the analog-output interface on RTlab, DSP collects the real-time PMSM operating information including currents, voltages and speed. Based on the collected information, DSP selects optimal voltage vector using the loaded MPDSC algorithm. Then, through the digital-input interface on RTlab, selected switching signals are sent into the

RTlab to control the inverter. The model in RTlab and the MPDSC algorithm in DSP can be revised and manipulated by the laptop. An oscilloscope is connected to the interface on RTlab to observe and record the operating information of the PMSM.

In this test, the sampling time is 200 μs while the simulation step size of the model in RTlab is 20 μs. The parameters of the machine and control listed in Table 2.1 are accordingly adopted in the HIL experiment test. The HIL results are shown in Fig. 4.20-4.22. Specifically, Fig. 4.20 shows the steady state response with the speed at 500 rpm. Fig. 4.21 presents the dynamic response when the load torque is stepped from 2 Nm up to 4 Nm with constant speed reference. Fig. 4.22 shows the dynamic response when the speed is in step change from 500 rpm to 1000 rpm with constant load torque. Once again, these HIL tests demonstrate the effectiveness of the proposed MPDSC control in speed tracking and torque ripple oscillation reduction.

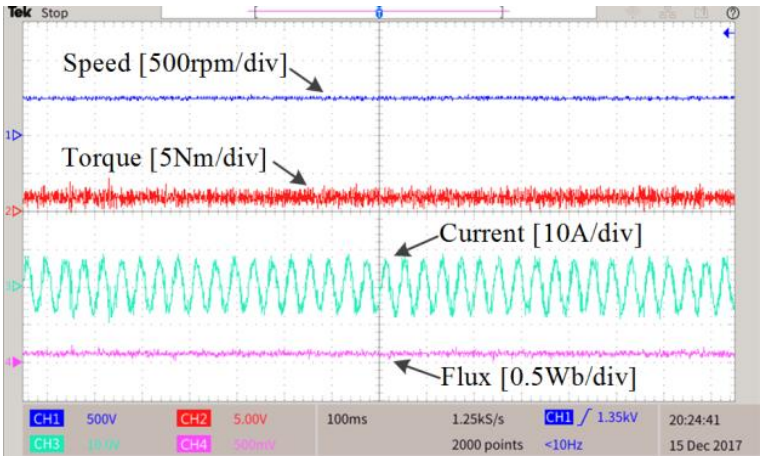

Fig. 4.20. HIL experimental results: steady state response of proposed MPDSC strategy at 500 rpm when the sampling frequency is 5 kHz.

A variety of HIL tests using 10kHz sampling frequency (100μs sampling period) are also conducted. Specifically, the motor transient performances of stepped changes in speed reference and load torque are compared, respectively. Fig. 4.23 presents the results of stepped changes in load torque with constant

speed, and Fig. 4.24 compares the performance of stepped changes in speed with constant load torque. These results successfully demonstrate that, without any cascade control loops or PID regulators, the proposed MPDSC method can achieve effective speed control and torque regulation.

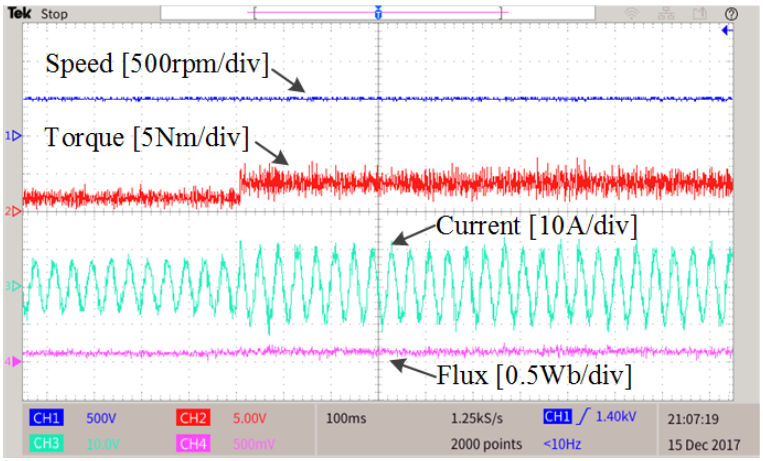

Fig. 4.21. HIL experimental results: dynamic response of proposed MPDSC strategy with a step change in load torque from 2 Nm to 4 Nm when the sampling frequency is 5 kHz.

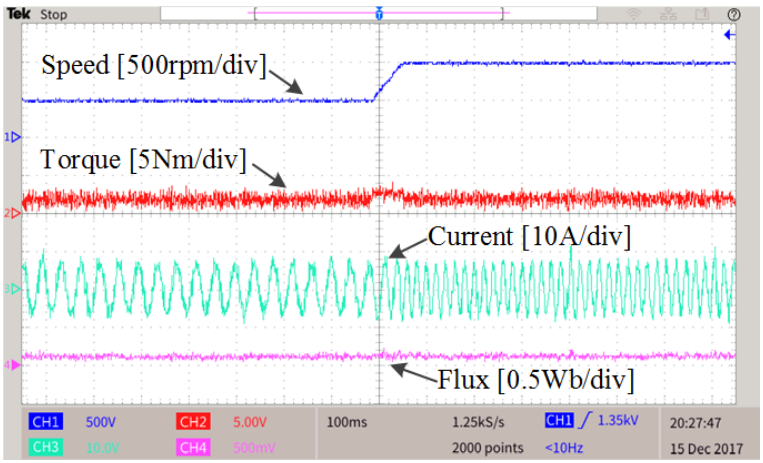

Fig. 4.22. HIL experimental results: dynamic response of proposed MPDSC strategy with a step change in speed from 500 rpm to 1000 rpm when the sampling frequency is 5 kHz.

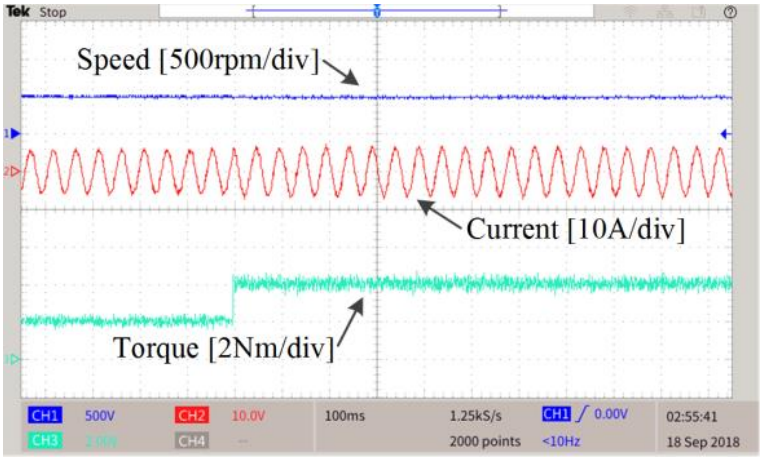

(a)

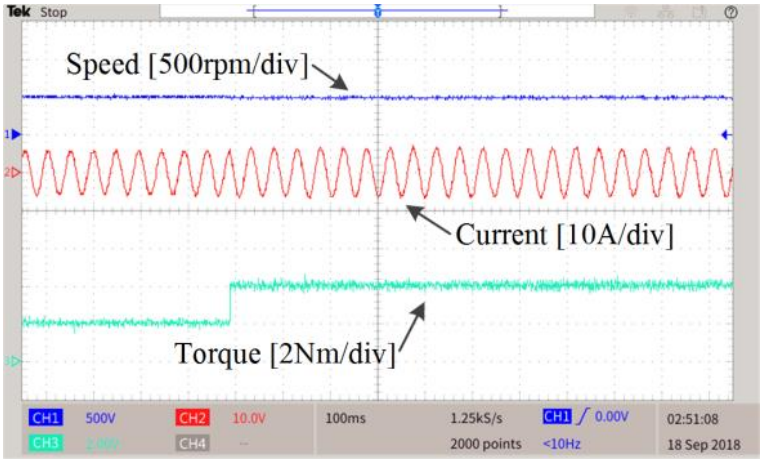

(b)

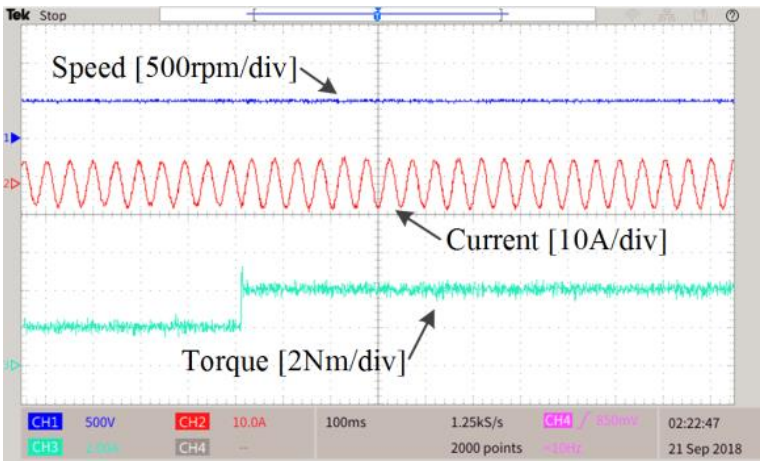

(c)

Fig. 4.23. HIL experimental results: dynamic response of a step change in load torque from 2 Nm to 4 Nm when the sampling frequency is 10 kHz. (a) Conventional DTC (P=2, I=0.5). (b) MPDTC (P=2, I=0.5). (c) Proposed MPDSC.

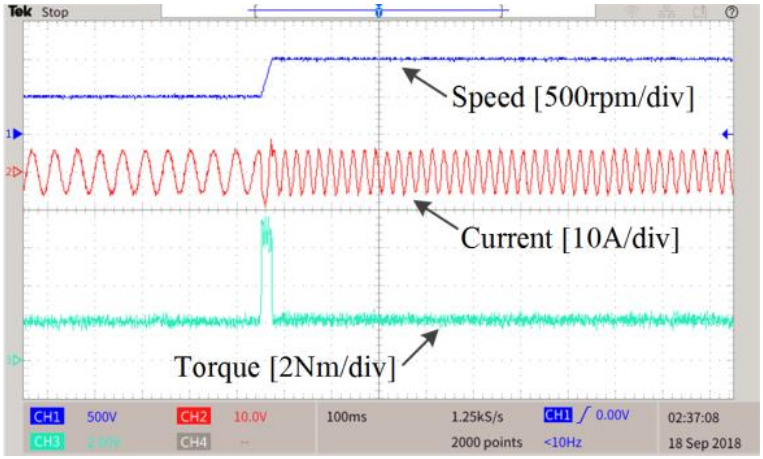

(a)

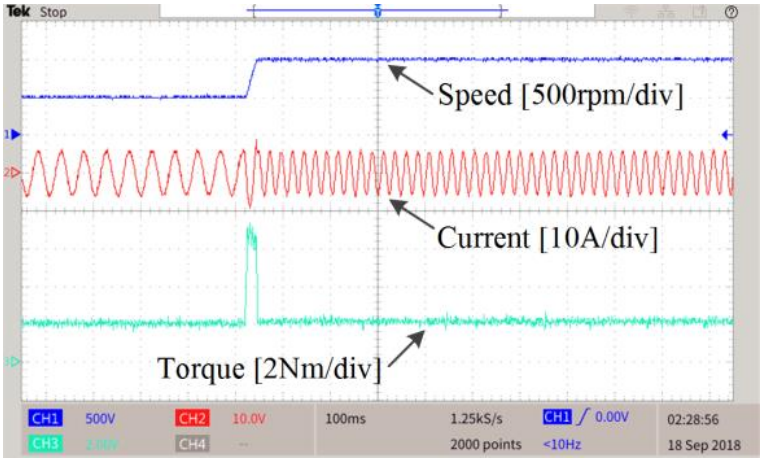

(b)

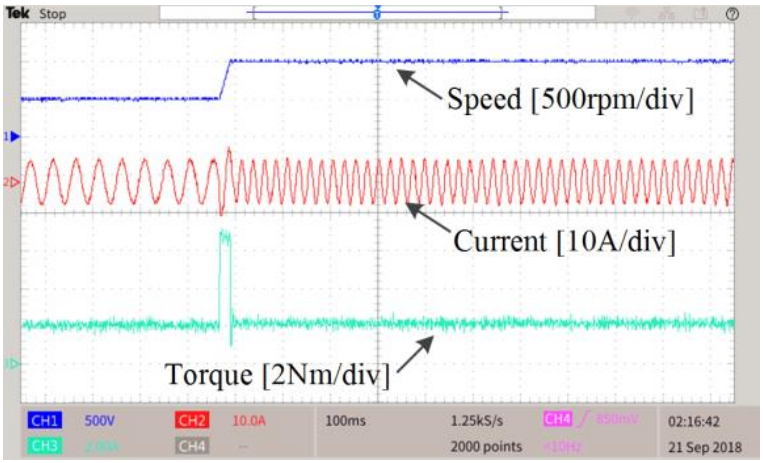

(c)

Fig. 4.24. HIL experimental results: dynamic response of a step change in speed from 500 rpm to 1000 rpm when the sampling frequency is 10 kHz. (a) Conventional DTC (P=2, I=0.5). (b) MPDTC (P=2, I=0.5). (c) Proposed MPDSC.

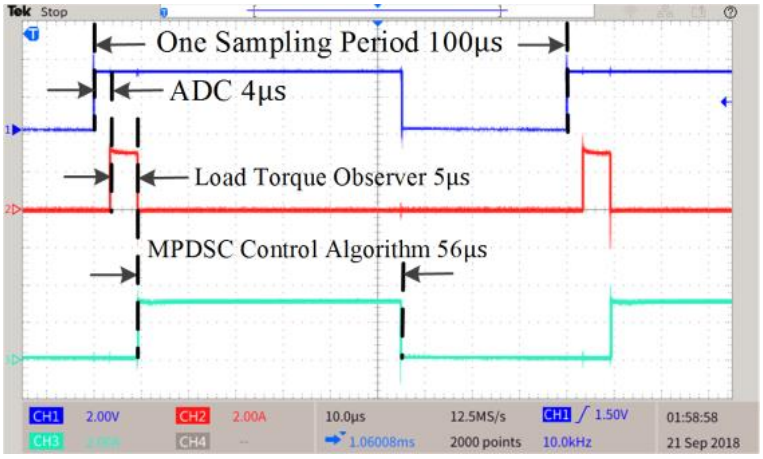

(a)

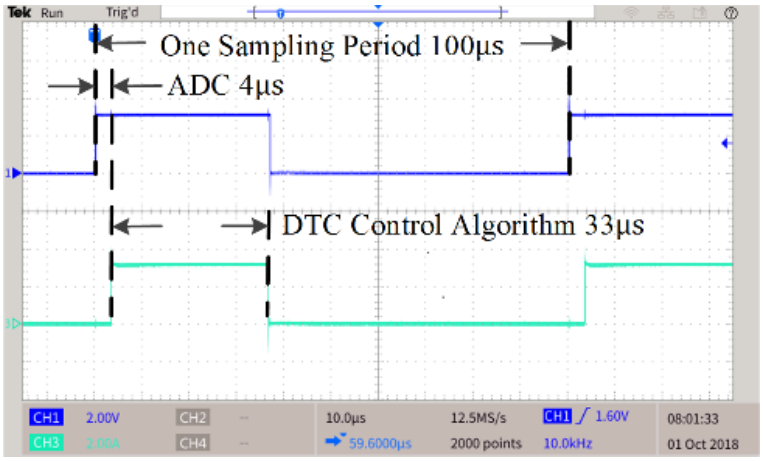

(b)

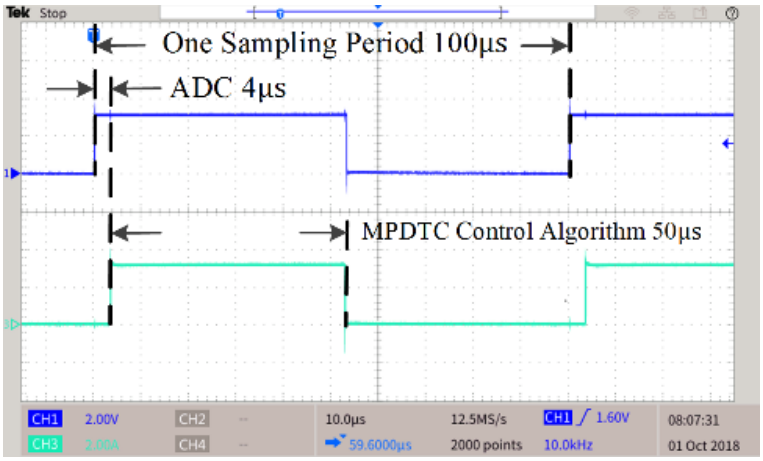

(c)

Fig. 4.25. Computational time in digital implementation using DSP (a) proposed MPDSC, (b) conventional DTC, and (c) MPDTC.

The computational time of important components has now been measured, as indicated in Fig. 4.25 (a). It can be seen that it takes about 4μs to complete the ADC process and about 5μs to execute the load torque observer. Then, the execution of the main control algorithm consumes about 56μs. Since the sampling period is 100μs, it is demonstrated that the proposed MPDSC controller can be executed completely within every control period. As expected, other methods have relatively less computational burden with about 33μs for conventional DTC Fig. 4.25 (b), and about 50μs for MPDTC Fig. 4.25 (c).

4.5 Summary

In this chapter, a MPDSC strategy has been developed, and the effectiveness of the proposed MPDSC strategy has been verified by simulations and HIL experiments. The proposed MPDSC strategy eliminated the PI unit, presenting an excellent speed tracking capability with very small speed offset. To reduce the manufacturing cost, an on-line load torque observer is firstly developed to track the variation of load torque. Then, a torque suppression factor is incorporated into the cost function to suppress large torque oscillations and overshoots during the start-up, speed-down and speed-up. Besides, the myopic prediction is introduced and analyzed. The correction of myopic prediction can enhance both the dynamic and steady state response, especially at low sampling frequency. Moreover, after a comparison, the proposed MPDSC strategy has an overall better performance than the conventional DTC. Finally, simulations and HIL experiments have verified the feasibility and effectiveness of the proposed MPDSC strategy.

Chapter V

Duty-Ratio-Based Model Predictive Direct Speed Control with Two Cost Functions for PMSM Drives

5.1 Introduction

The previous chapter has demonstrated the single-vector-based MPDSC to enhance the response of speed and torque, where the speed offset is very small, and the torque ripple is mitigated by the utilization of compensation factors. However, all existing MPDSC methods use only one voltage vector in a control period [138-140, 166], and the speed ripple and torque ripple can be further optimized by employing more than one voltage vector in a control period. The duty-ratio-based MPDSC presented in this chapter would fully consider every combination possibility of the active voltage vector and the zero voltage vector. Eight combinations of voltage vectors are thus developed, to be refined by the two cost function acting sequentially. The mechanism of using two cost functions can not only improve the dynamic of the proposed MPDSC, but also ensure an optimal selection of voltage vector combination. More detailed analysis and verification will be illustrated in the flowing sections.

This chapter is organized as follows. In section 5.2, with the parameter estimation for future sampling instant, the procedures to deduce eight duty ratios are introduced, and eight combinations of voltage vectors are developed. After that, two cost functions are formulated to refine the combinations of voltage vectors. Simulation results and HIL experimental tests are presented in section 5.3 and 5.4, respectively.

5.2 Methodology

The overall control diagram of the proposed duty-ratio-based MPDSC strategy is shown in Fig. 5.1, and the control process can be described as follows.

a. The load torque is first estimated using a load torque observer. An on-line minimum order load torque observer (MOLTO) is employed to estimate the actual load torque in a real-time manner. Such MOLTO system has been defined in Chapter IV, subsection 4.3.2.

b. The estimated load torque $\tilde{T}_L$, together with real-time measurements from the PMSM and the optimal duty ratio d_{opt} determined at $(k-1)th$ time instant, will be used to conduct the prediction at $(k+1)th$ time instant. Meanwhile, eight duty ratios $d_{V_i}^{k+1}$ corresponding to eight possible voltage vectors V_i can

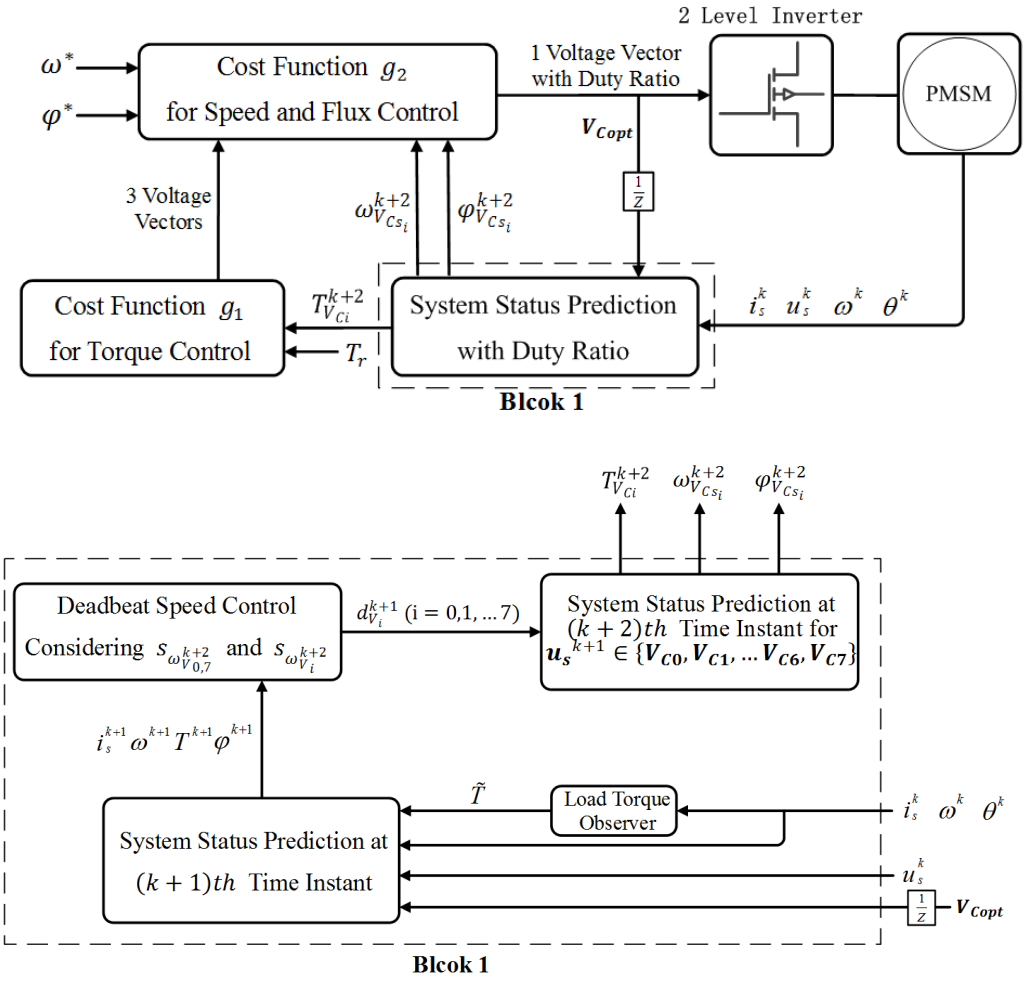

Fig. 5.1. Control diagram of the proposed duty-ratio-based MPDSC

be calculated using the slope of speed $s_{\omega_{V_i}^{k+2}}$ (i = 0,1, ... 7) according to the deadbeat criteria. Eight combinations of voltage vector are thus formed.

c. The motor status at $(k+2)th$ time instant is then predicted with the substitution of duty ratios. First, a cost function g_1 is used to pre-select three combinations of voltage vector for torque ripple reduction. The optimal voltage vector combination out of three is then further determined by the second cost function g_2 for speed control. At this step, the corresponding optimal duty ratio d_{opt} is saved in the register waiting to be applied on next control period.

Now, a more detailed illustration of the proposed control algorithm will be presented in the following subsections.

5.2.1 System Status Prediction

There are totally eight voltage vectors that can be applied to the two-level inverter, i.e., $\boldsymbol{u_s} \in \{\boldsymbol{V_0}, \boldsymbol{V_1}, \dots \boldsymbol{V_6}, \boldsymbol{V_7}\}$. With the measured machine information at $k\ th$ time instant, including $\boldsymbol{i_s^k}$, $\boldsymbol{u_s^k}$, ω^k and θ^k, the parameter prediction can be conducted.

When the selected active voltage vector, i.e., one of $\{\boldsymbol{V_1}, \boldsymbol{V_2}, \dots \boldsymbol{V_6}\}$, is applied during the control period, (2.8) and (2.9) can be rewritten as

$$\frac{di_{d\_V_i}^k}{dt} = -\frac{1}{L_d}\left(R_s i_d^k + \varphi_q^k \omega^k + u_d^k\right) \tag{5.1}$$

$$\frac{di_{q\_V_i}^k}{dt} = -\frac{1}{L_q}\left(-R_s i_q^k + \varphi_d^k \omega^k + u_q^k\right) \tag{5.2}$$

When zero voltage vectors ($\boldsymbol{V_0}$ or $\boldsymbol{V_7}$) are selected and applied during the control period, (2.8) and (2.9) are then obtained as

$$\frac{di_{d\_V_{0,7}}^k}{dt} = -\frac{1}{L_d}\left(R_s i_d^k + \varphi_q^k \omega^k\right) \tag{5.3}$$

$$\frac{di_{q\_V_{0,7}}^k}{dt} = -\frac{1}{L_q}\left(-R_s i_q^k + \varphi_d^k \omega^k\right) \tag{5.4}$$

The stator current at $(k+1)\ th$ time instant can be calculated as

$$i_d^{k+1} = i_d^k + d_{opt}^k T_s \frac{di_{d\_V_i}^k}{dt} + \left(1 - d_{opt}^k\right) T_s \frac{di_{d\_V_{0,7}}^k}{dt} \tag{5.5}$$

$$i_q^{k+1} = i_q^k + d_{opt}^k T_s \frac{di_{q\_V_i}^k}{dt} + \left(1 - d_{opt}^k\right) T_s \frac{di_{q\_V_{0,7}}^k}{dt} \tag{5.6}$$

where d_{opt}^k is the duty ratio between the active vector application duration and the zero vector application duration, which is selected during $(k-1)\ th$ to kth time instant. Meanwhile, the electromagnetic torque T^{k+1} at $(k+1)th$ time instant can be derived by the equation (2.14). The speed at $(k+1)th$ time instant is therefore obtained using the mechanical equation (2.21).

$$\omega^{k+1} = \omega^k + \frac{T_s}{J}\left(T^{k+1} - \tilde{T}_L - B_m \omega^k\right) \tag{5.7}$$

The above predicted parameters at the $(k+1)th$ time instant, along with eight voltage vectors ${\boldsymbol{u}_s}^{k+1} \in \{\boldsymbol{V_0}, \boldsymbol{V_1}, \ldots \boldsymbol{V_6}, \boldsymbol{V_7}\}$, will be employed in the following procedures to develop the combinations of voltage vector.

When the zero voltage vector ($\boldsymbol{V_0}$ and $\boldsymbol{V_7}$) is applied to the two-level inverter during the whole period from $(k+1)th$ to $(k+2)th$ time instant, $\frac{di_{d\_V_{0,7}}^{k+1}}{dt}$ and $\frac{di_{q\_V_{0,7}}^{k+1}}{dt}$ can be obtained as

$$i_{d\_V_{0,7}}^{k+2} = i_d^{k+1} + T_s \frac{di_{d\_0,7}^{k+1}}{dt} \tag{5.8}$$

$$i_{q\_V_{0,7}}^{k+2} = i_q^{k+1} + T_s \frac{di_{q\_0,7}^{k+1}}{dt} \tag{5.9}$$

Following the deduction procedures presented before, the corresponding electromagnetic torque $T_{V_{0,7}}^{k+2}$ is thus derived, which is further used to calculate the rotor speed at $(k+2)th$ time instant

$$\omega_{V_{0,7}}^{k+2} = \omega^{k+1} + \frac{T_s}{J}\left(T_0^{k+2} - \tilde{T}_L - B_m \omega^{k+1}\right) \tag{5.10}$$

5.2.2 Effect of Zero Vectors and Determination of Duty Ratio

A simple and effective method to improve MPC performance is the employment of the duty ratio modulation [119, 141, 147]. In other words, more than one vector is applied duration every control period based on an optimal duty ratio. Although this method has been adopted in direct torque control, it has not

been studied in direct speed control yet due to the complicated speed prediction model. Before deriving the duty ratio for direct speed control, it is better to investigate into the effects of different voltage vectors on the PMSM. More specifically, for eight voltage vectors, $\frac{dT}{dt}$, $\frac{d\omega}{dt}$ and $\frac{d|\boldsymbol{\varphi}|}{dt}$ are investigated to present a clear analysis.

As shown in Fig. 5.2, the variation of $\frac{dT}{dt}$, $\frac{d\omega}{dt}$ and $\frac{d|\boldsymbol{\varphi}|}{dt}$ are depicted for eight voltage vectors. Every particular electric angle corresponds to a specific time instant, and different voltage vectors result in various values of $\frac{dT}{dt}$, $\frac{d\omega}{dt}$ and $\frac{d|\boldsymbol{\varphi}|}{dt}$. Taking $\boldsymbol{V_1}$ (red curve) for instance, when electric angle is 60°, $\frac{dT}{dt}$ and $\frac{d\omega}{dt}$ are positive values, which indicates that applying $\boldsymbol{V_1}$ can increase both the electromagnetic torque and rotor speed; however, $\frac{d|\boldsymbol{\varphi}|}{dt}$ is a negative value, resulting in a decreased stator flux by applying $\boldsymbol{V_1}$. When electric angle is 120°, $\frac{dT}{dt}$, $\frac{d\omega}{dt}$ and $\frac{d|\boldsymbol{\varphi}|}{dt}$ are all positive values, applying $\boldsymbol{V_1}$ can increase all three parameters.

It can be concluded that, by applying a same active voltage vector (one of $\{\boldsymbol{V_1}, \boldsymbol{V_2}, \ldots \boldsymbol{V_6}\}$), the changing tendency of the electromagnetic torque and speed are similar, while the changing tendency of the stator flux may not be the same. Besides, by applying zero voltage vectors ($\boldsymbol{V_0}$ or $\boldsymbol{V_7}$), $\frac{dT}{dt}$, $\frac{d\omega}{dt}$ and $\frac{d|\boldsymbol{\varphi}|}{dt}$ are all very small (almost zero), indicating that zero voltage vectors will not cause significant changes in the controlled variables. Consequently, with the insertion of the zero voltage vectors, the PMSM can be better controlled with reduced ripples in torque, speed or flux, provided that the duty ratio between the active vector duration and zero vector duration can be optimized. A specific case is that, when the duty ratio is 0, such combination of voltage vector can be regarded as a single zero voltage vector.

After the investigation of zero vector effect, let us now move on to design the duty ratio for direct speed control. The speed slope $s_{\omega_{V_{0,7}}^{k+2}}$, which can reflect the effect of applied zero voltage vector ($\boldsymbol{V_0}$ or $\boldsymbol{V_7}$) during the whole period from $(k+1)th$ to $(k+2)th$ time instant, is therefore deduced as

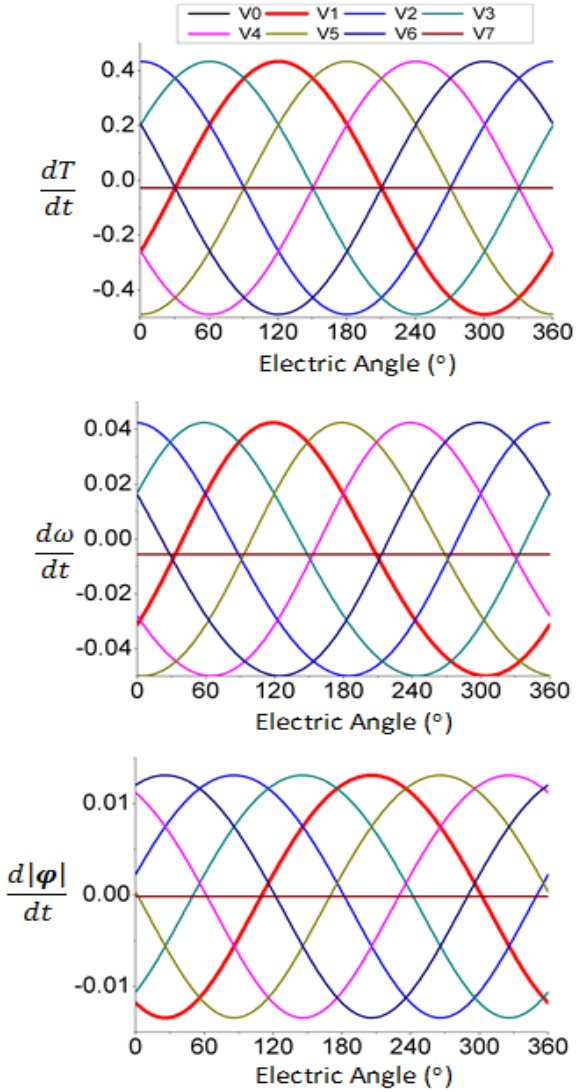

Fig. 5.2. $\frac{dT}{dt}$, $\frac{d\omega}{dt}$ and $\frac{d|\boldsymbol{\varphi}|}{dt}$ for eight voltage vectors.

$$s_{\omega_{V_{0,7}}^{k+2}} = \frac{d\omega_{V_{0,7}}^{k+2}}{dt} = \frac{1}{J}\left(T_{V_{0,7}}^{k+2} - T_L - B_m\omega_{V_{0,7}}^{k+2}\right) \tag{5.11}$$

Following the above steps (5.8)-(5.11), for eight voltage vectors $\boldsymbol{u_s}^{k+1} \in \{\boldsymbol{V_0}, \boldsymbol{V_1}, \ldots \boldsymbol{V_6}, \boldsymbol{V_7}\}$, the slope of speed $s_{\omega_{V_i}^{k+2}}$ (i = 0,1, ... 7), representing the speed charging tendency from $(k+1)th$ to $(k+2)th$ time instant, can be obtained as

$$s_{\omega_{V_i}^{k+2}} = \frac{d\omega_{V_i}^{k+2}}{dt} = \frac{1}{J}\left(T_{V_i}^{k+2} - T_L - B_m\omega_{V_i}^{k+2}\right) \tag{5.12}$$

Based on the deadbeat speed criterion, the duty ratio for eight voltage vectors can be calculated as

$$d_{V_i}^{k+1} = \frac{\omega^* - \omega^{k+1} - T_s\left(s_{\omega_{V_{0,7}}^{k+2}}\right)}{T_s\left(s_{\omega_{V_i}^{k+2}} - s_{\omega_{V_{0,7}}^{k+2}}\right)} \text{ (i = 0,1, ... 7)} \tag{5.13}$$

It should be mentioned that the magnitude of $d_{V_i}^{k+1}$ is in the range of [0, 1]. The possible combination does not have to always contain one active voltage vector and one zero voltage vector. For example, $d_{V_i}^{k+1} = 0$ indicates one zero voltage vector is applied during the whole control period.

5.2.3 Selection of Optimal Combination of Voltage Vector

Every voltage vector has its corresponding duty ratio $d_{V_i}^{k+1}$, which indicates that there are eight combinations of voltage vectors. Eight combinations of voltage vectors, named $\{\boldsymbol{V_{C0}}, \boldsymbol{V_{C1}}, \ldots \boldsymbol{V_{C7}}\}$, are developed. As is shown in Table 5.1, each combination is consisted of an active voltage vector and a calculated duty ratio based on deadbeat speed criterion.

TABLE 5.1
Eight Combinations of Voltage Vectors

Combination of Voltage Vectors	Active Voltage Vector	Duty Ratio Based on Deadbeat Speed Criterion
$\boldsymbol{V_{C0}}$	$\boldsymbol{V_0}$=**0**	$d_{V_0}^{k+1} = 0$
$\boldsymbol{V_{C1}}$	$\boldsymbol{V_1}$	$d_{V_1}^{k+1}$
$\boldsymbol{V_{C2}}$	$\boldsymbol{V_2}$	$d_{V_2}^{k+1}$
$\boldsymbol{V_{C3}}$	$\boldsymbol{V_3}$	$d_{V_3}^{k+1}$
$\boldsymbol{V_{C4}}$	$\boldsymbol{V_4}$	$d_{V_4}^{k+1}$
$\boldsymbol{V_{C5}}$	$\boldsymbol{V_5}$	$d_{V_5}^{k+1}$
$\boldsymbol{V_{C6}}$	$\boldsymbol{V_6}$	$d_{V_6}^{k+1}$
$\boldsymbol{V_{C7}}$	$\boldsymbol{V_7}$=**0**	$d_{V_7}^{k+1} = 0$

With the consideration of the reduction of switching frequency, the corresponding zero voltage vectors are assigned to minimize the switching frequency, as is tabulated in Table 5.2.

TABLE 5.2

Eight Combinations of Voltage Vectors and Corresponding Zero Voltage Vectors to Minimize Switching Frequency

Combination of Voltage Vectors	Corresponding Zero Voltage Vectors to Minimize Switching Frequency
$\boldsymbol{V_{C0}}$	$\boldsymbol{V_0}$
$\boldsymbol{V_{C1}}$	$\boldsymbol{V_0}$
$\boldsymbol{V_{C2}}$	$\boldsymbol{V_0}$
$\boldsymbol{V_{C3}}$	$\boldsymbol{V_7}$
$\boldsymbol{V_{C4}}$	$\boldsymbol{V_0}$
$\boldsymbol{V_{C5}}$	$\boldsymbol{V_7}$
$\boldsymbol{V_{C6}}$	$\boldsymbol{V_7}$
$\boldsymbol{V_{C7}}$	$\boldsymbol{V_7}$

One of eight combinations of voltage vectors will be selected and applied during the control period from $(k+1)th$ time instant to $(k+2)th$ time instant. The parameters at $(k+1)th$ time instant are already obtained in section II.B. Following the similar procedures from (14) to (20), the parameter estimation can be conducted once again for $(k+2)th$ time instant for eight combinations of voltage vectors. Eight combinations of voltage vectors can deduce eight groups of parameters at $(k+2)th$ time instant. Each group consists of the following parameters: the stator currents $i_{d\_V_{Ci}}^{k+2}$ and $i_{q\_V_{Ci}}^{k+2}$, stator fluxes $\varphi_{d\_V_{Ci}}^{k+2}$ and $\varphi_{q\_V_{Ci}}^{k+2}$, the electromagnetic torque $T_{V_{Ci}}^{k+2}$ and the rotor speed $\omega_{V_{Ci}}^{k+2}$ $(\mathrm{i} = 0,1,\dots 7)$. Specifically, the electromagnetic torque $T_{V_{Ci}}^{k+2}$ can be expressed as

$$T_{V_{Ci}}^{k+2} = 1.5p\left(\varphi_f i_{q\_V_{Ci}}^{k+2} + \Delta L i_{d\_V_{Ci}}^{k+2} i_{q\_V_{Ci}}^{k+2}\right) \tag{5.14}$$

and the rotor speed $\omega_{V_{Ci}}^{k+2}$ is

$$\omega_{V_{Ci}}^{k+2} = \omega^{k+1} + \frac{T_s}{J}\left(T_{V_{Ci}}^{k+2} - \tilde{T}_L - B_m\omega^{k+1}\right) \tag{5.15}$$

These parameters will be further evaluated by two cost functions (g_1 and g_2) to finally determine the optimal vector combination.

The first cost function g_1 is defined as

$$min.\, g_1 = C_1 + C_T \tag{5.16}$$
$$\text{s.t.}\, \boldsymbol{u_s}^{k+1} \in \{\boldsymbol{V_{C0}}, \boldsymbol{V_{C1}}, \ldots \boldsymbol{V_{C6}}, \boldsymbol{V_{C7}}\}$$

g_1 consists of two parts, i.e., C_1 and C_T. The objective of C_1 is to enhance the dynamic response, which is defined as

$$C_1 = \left|T_{V_{Ci}}^{k+2} - T_r\right| \text{ (i = 0,1, ... 7)} \tag{5.17}$$

Although the dynamic response can be enhanced by C_1, there is no restriction on the predicted value of electromagnetic torque $T_{V_{Ci}}^{k+2}$. Thus, the electromagnetic torque could exceed the rated limit during transients, such as start-up, speed-up and speed-down. Such undesired overshoot of electromagnetic torque may damage the whole PMSM system. A compensation factor C_T is therefore introduced in the cost function g_1 to refine the selected voltage vectors. With the consideration of one-step delay, compensation factor C_T is defined as

$$C_T = \begin{cases} \infty & \left|T_{V_{Ci}}^{k+2}\right| > T_r \\ 0 & \left|T_{V_{Ci}}^{k+2}\right| \leq T_r \end{cases} \tag{5.18}$$

The compensation factor C_T has two values, i.e. ∞ and 0. When the electromagnetic torque $T_{V_{Ci}}^{k+2}$ is greater than the rated electromagnetic torque T_r, compensation factor C_T is equal to ∞. This means that the corresponding voltage vector V_i will not be selected as it will cause large torque oscillations. In contrast , when the electromagnetic torque $T_{V_{Ci}}^{k+2}$ is smaller than the rated electromagnetic torque T_r , compensation factor C_T becomes 0, which indicates that the corresponding voltage vector V_i is of higher selection priority, and it could be selected provided it also leads to a small value of C_1.

At the first selection stage, three combinations of voltage vectors ($\boldsymbol{V_{Cs_1}}, \boldsymbol{V_{Cs_2}}, \boldsymbol{V_{Cs_3}}$) that can generate three smallest values of the cost function g_1 will be preselected, awaiting to be evaluated again at the second selection stage. Since three combinations of voltage vectors have been preselected by the first cost function g_1 to guarantee a good dynamic response, there is still selection freedom remaining for the second cost function g_2 to regulate the speed and flux.

At the second selection stage, the second cost function g_2 is defined as

$$min.\, g_2 = C_2 + C_T \tag{5.19}$$
$$\text{s.t.}\, \boldsymbol{u_s}^{k+1} \in \{\boldsymbol{V_{Cs_1}}, \boldsymbol{V_{Cs_2}}, \boldsymbol{V_{Cs_3}}\}$$

g_2 consists of two parts. The first part C_2 is defines as

$$C_2 = \left|\omega_{V_{Cs_i}}^{k+2} - \omega^*\right| + \left|\varphi_{V_{Cs_i}}^{k+2} - \varphi^*\right| \text{ (i = 1,2,3)} \tag{5.20}$$

where $\varphi_{V_{Cs_i}}^{k+2} = \sqrt{\left(\varphi_{d\_V_{Cs_i}}^{k+2}\right)^2 + \left(\varphi_{q\_V_{Cs_i}}^{k+2}\right)^2}$. In C_2, the first term aims to track the rotor speed reference, as well as to minimize the speed ripple. The stator flux is regulated by the second term in C_2. The reference of stator flux is obtained based on the maximum torque per ampere (MPTA) principle to enhance the efficiency. If the stator flux $\varphi_{V_{Cs_i}}^{k+2}$ can track the reference, smaller ripple of stator flux results in lower stator current's total harmonic distortion (THD), which contributes to more sinusoidal current waveform.

It is necessary to integrate C_T into g_2 to avoid the selection of undesired voltage vector combination. As three combinations of voltage vectors are forced to be preselected by the first cost function g_1, some of them may include the compensation factor C_T with ∞, and these combinations of voltage vectors should be excluded from the final selection. Without C_T in the second cost function g_2, undesired combination of voltage vector could be selected as the optimal one, which may damage the PMSM. Adding C_T can further enhance the stability of the proposed duty-ratio-based MPDSC. Consequently, with the refinement of cost function g_2, an optimal combination of voltage vector $\boldsymbol{V_{Copt}}$ is finally selected and applied to the PMSM. The corresponding active voltage vector and duty ratio are $\boldsymbol{V_{opt}}$ and $d_{V_{opt}}^{k+1}$ respectively. They will be employed to conduct the system status prediction at next time instant, using equations from (5.1) to (5.7).

5.3 Numerical Simulation

In this section, the proposed MPDSC strategy is validated by numerical simulation in MATLAB/Simulink. The parameters of PMSM and control system shown in Table 2.1 are used in the simulation.

5.3.1 Steady State Response

At a rotor speed of 500 rpm, the steady-state response of the proposed duty-ratio-based MPDSC is presented in Fig. 5.3. It can be seen that, by using the proposed duty-ratio-based MPDSC, the PMSM generates a very small ripple in both rotor speed and electromagnetic torque, and the speed offset is extremely small. Besides, the stator current is sinusoidal. However, it should be noted that there exists a small offset of electromagnetic torque. This is because the electromagnetic torque is indirectly manipulated in speed control in the second cost function (5.19). In other words, it is reasonable since the minimization of torque offset is not the control objective of the proposed duty-ratio-based MPDSC. More numerical analysis and comparison are demonstrated in next subsection.

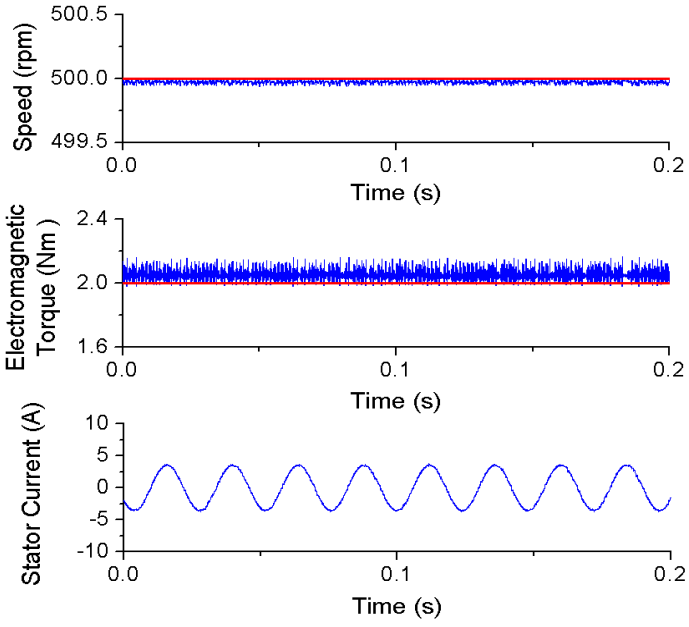

Fig. 5.3. Steady state response of proposed MPDSC when speed is 500rpm.

5.3.2 Dynamic Response on Speed Change

In this subsection, the effectiveness of the proposed duty-ratio-based MPDSC are validated by the comparisons of different methods, i.e., conventional MPDSC and conventional direct torque control (DTC).

For conventional MPDSC, the basic control logic is similar to the proposed duty-ratio-based MPDSC. However, it uses a single cost function g_c. Moreover, only one voltage vector will be selected and applied during every control period [138-140, 166].

With respect to conventional DTC, the control diagram is shown in Fig. 5.4. A PI speed-to-torque loop is employed to convert speed reference to torque reference. After the manipulation of hysteresis loop for electromagnetic torque and stator flux, the optimal voltage vector is selected from a predefined switching table [56, 57].

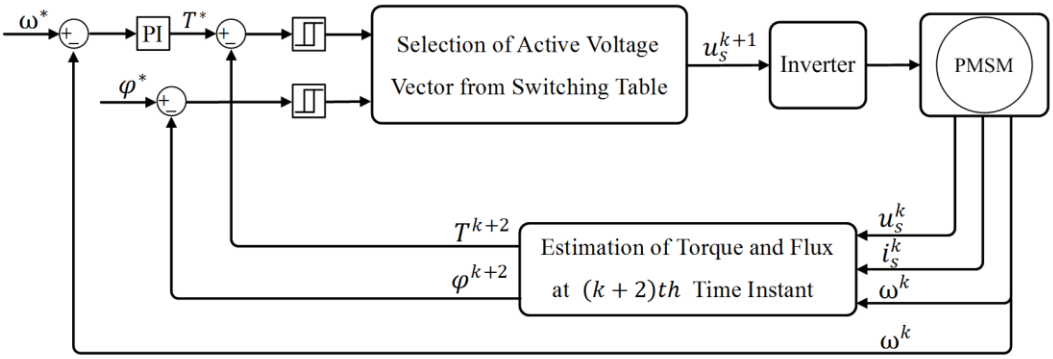

Fig. 5.4. Control diagram of conventional DTC

When the speed changes from 500 rpm to 1000 rpm at the time of 0.1s, Fig. 5.5-5.7 shows the dynamic response of the proposed duty-ratio-based MPDSC, conventional MPDSC and conventional DTC, respectively. For these three methods, it is seen that the proposed duty-ratio-based MPDSC shows the best control performance in terms of speed, electromagnetic torque and stator current. Further discussions are as follows.

First of all, the proposed duty-ratio-based MPDSC performs the best speed control performance, where both the speed offset and speed ripple are at the smallest values among three methods, as shown in Fig. 5.5. The speed offset and speed ripple of the proposed duty-ratio-based MPDSC are only 0.0055% and 0.0121rpm respectively. In Fig. 5.6, conventional MPDSC performs a slightly larger speed offset (0.0757%), and a much larger speed ripple (0.1701rpm) than the proposed method. The conventional DTC shown in Fig. 5.7 exhibits the largest speed offset (1.3741%) and speed ripple (0.2782rpm) among three control methods. If there is no variation of operation condition, the speed ripple of three control methods will not change over time. The speed offsets of conventional MPDSC and conventional DTC will be increasingly smaller owing to the effect of PI adaptor. Nevertheless, the proposed MPDSC can always reach the reference speed by taking the least time. In other words, the proposed MPDSC behaves the fastest dynamic response of speed.

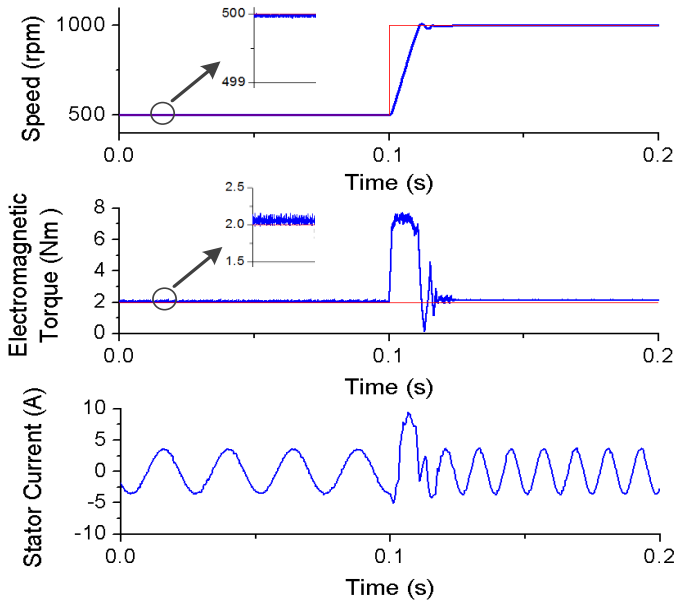

Fig. 5.5. Dynamic response of proposed MPDSC when speed changes from 500 rpm to 1000 rpm

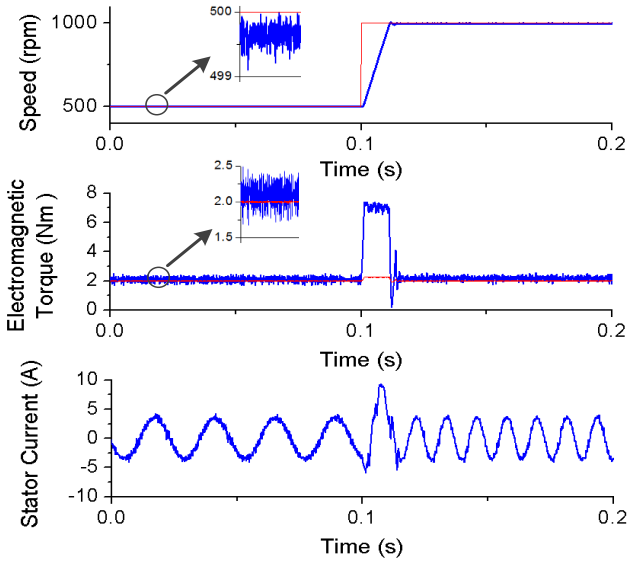

Fig. 5.6. Dynamic response of the conventional MPDSC when speed changes from 500 rpm to 1000 rpm.

Besides, the proposed method also has the smallest torque ripple (0.0423Nm) over the other control methods (conventional MPDSC: 0.1438Nm and conventional DTC: 0.2274Nm). Moreover, the stator current of the proposed method is more sinusoidal, which indicates that it has lowest THD among three control methods. The comparison validates the effectiveness and superiority of the proposed duty-ratio-based MPDSC.

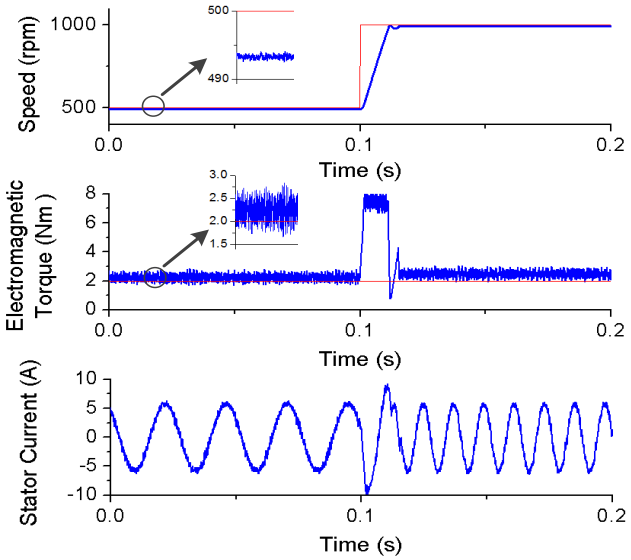

Fig. 5.7. Dynamic response of conventional DTC when speed changes from 500 rpm to 1000 rpm (P=3, I=0.5).

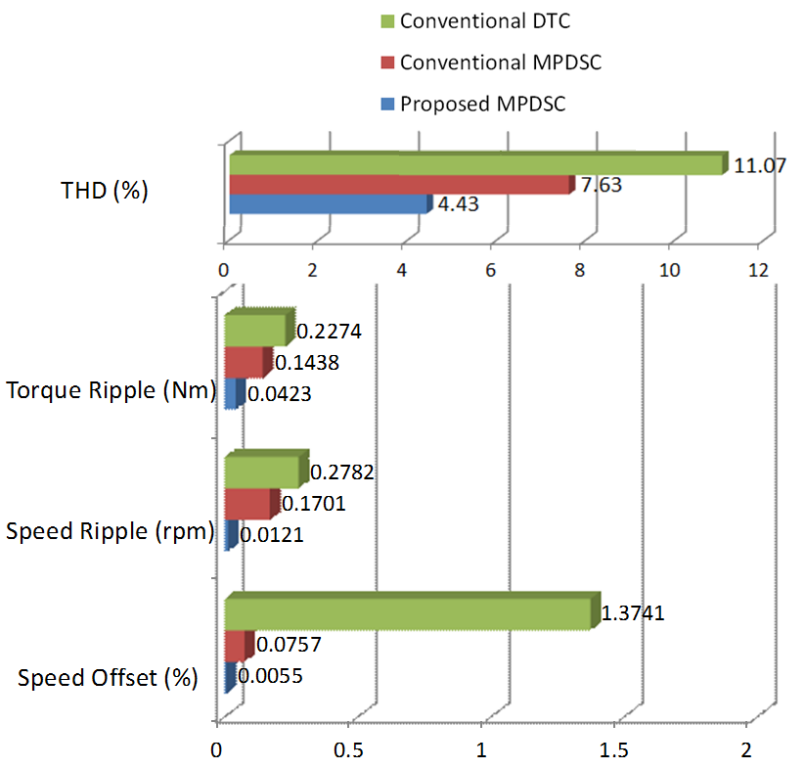

Fig. 5.8. The comparison of proposed MPDSC, conventional MPDSC and conventional DTC.

To give a more straightforward comparison among three control methods, the THD, the torque ripple, the speed ripple, and the speed offset are summarized in Fig. 5.8. It directly demonstrates that the proposed duty-ratio-based MPDSC has the best control performance in terms of THD, torque ripple, speed ripple, and speed offset at 4.43%, 0.0423Nm, 0.0121rpm and 0.0055%, respectively.

5.4 Hardware-in-the-Loop Test

The proposed strategy is further validated in a HIL testing platform, as is shown in Fig. 5.9. The experimental setup consists of a laptop, an OPAL-RT OP5700 simulator, a DSP with F28335 chip, and an oscilloscope. The laptop is used to develop the proposed MPDSC code, and download it to the DSP. Apart from the MPDSC code, the rest of PMSM system is implemented using RT-LAB. The PMSM, the DC bus and the inverter are modelled and run in the OP5700 simulator. DSP gathers the machine information from the OP5700 simulation

through the DSP input interface. The PWM gate driving signals, generated by the DSP, will output to the OP5700 simulator to control the PMSM.

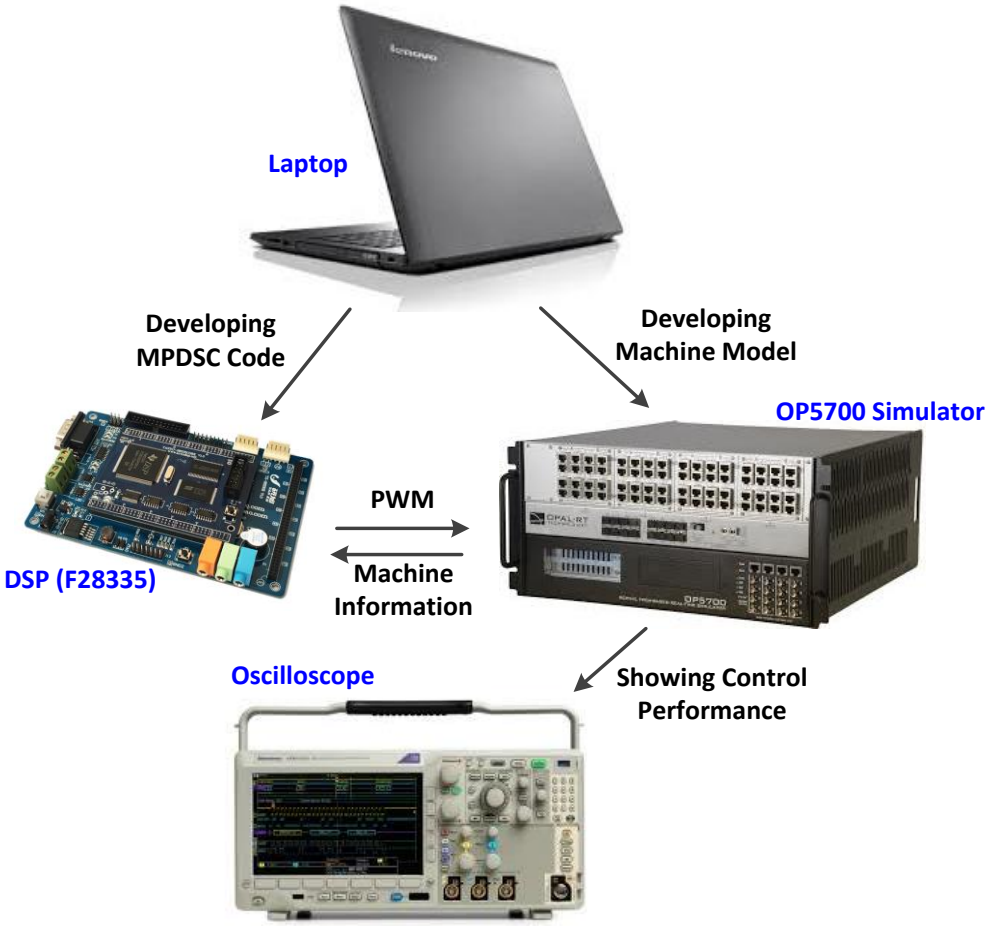

Fig. 5.9. HIL testbed for the verification of duty-ratio-based MPDSC strategy.

In this test, the sampling time of DSP is 100 μs. The PMSM parameters and control data listed in Table 2.1 are adopted in this HIL test accordingly. Fig. 5.10 shows the stead-state performance. Fig. 5.11 presents dynamic response with a step-up change in speed from 500 rpm to 1000 rpm. On the other hand, the dynamic responses of load torque are shown in Fig. 5.13 with a step-up change from 2 Nm to 4 Nm. The test results verify the effectiveness of the proposed two-vector-based MPDSC.

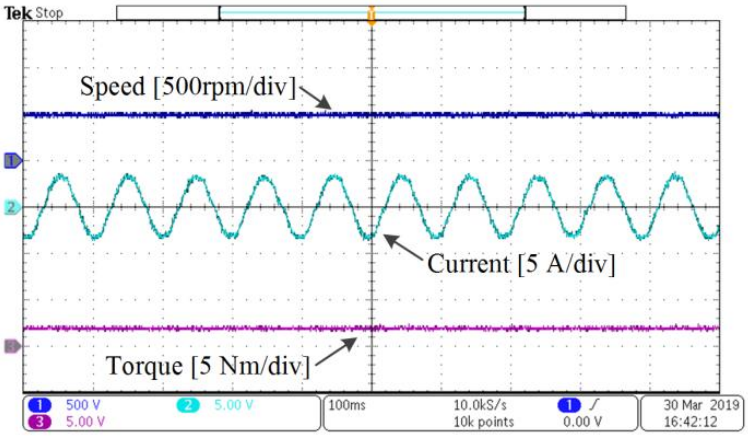

Fig. 5.10. HIL experimental results: steady state response of proposed MPDSC strategy with the speed at 500rpm.

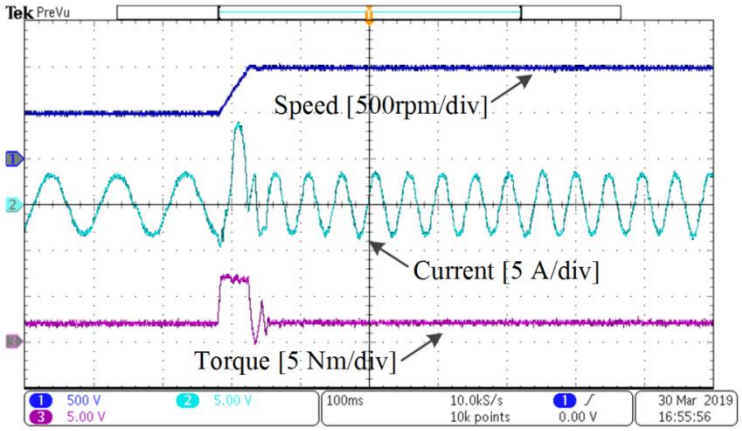

Fig. 5.11. HIL test results: dynamic response of proposed MPDSC strategy with a step change in speed from 500 rpm to 1000 rpm.

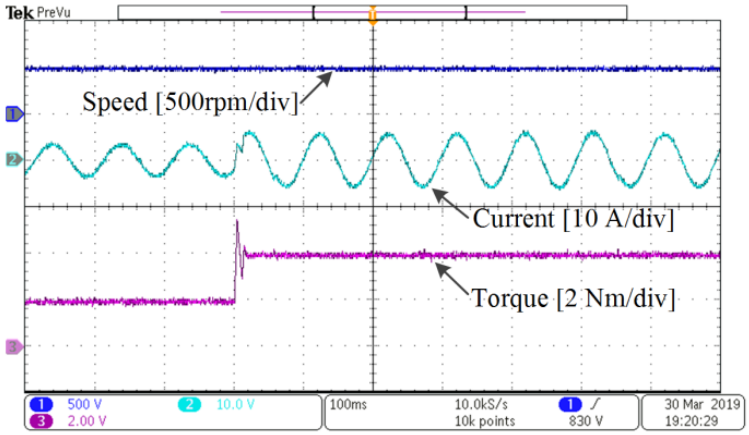

Fig. 5.12. HIL test results: dynamic response of proposed MPDSC strategy with a step-up change in load torque from 2 Nm to 4 Nm.

As is indicated in Fig. 5.13, the computational time is measured for different procedures. The total computational time is 85μs. The completeness of ADC process requires about 4μs, and the load torque observer takes around 5μs to estimate the load torque. Besides, the execution of the proposed MPDSC code consumes about 76μs. As the sampling period is 100μs, the proposed MPDSC can execute completely in the designed control period.

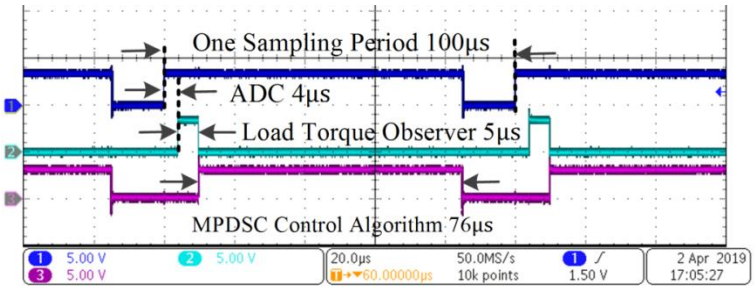

Fig. 5.13. Computational time of proposed MPDSC in digital implementation using DSP.

5.5 Summary

In this chapter, an improved finite-set MPDSC has been proposed to enhance the control performance in terms of speed offset, speed ripple and torque ripple. The feasibility and superiority of the proposed MPDSC has been well validated by MATLAB simulations and HIL tests. Eight duty ratios are integrated with eight voltage vectors to form eight combinations of voltage vectors. An optimal combination of voltage vectors is finally selected through two cost functions acting sequentially. Comparison by simulations presents that the proposed MPDSC performs an excellent control performance: the THD, the torque ripple, the speed ripple, and the speed offset are 4.43%, 0.0423Nm, 0.0121rpm and 0.0055% respectively. HIL tests also verified the effectiveness of the proposed MPDSC. Finally, it can be affirmed that this strategy performs better than classical DTC, and the MPDSC presented in Chapter IV, during steady state as well as transient operation.

Chapter VI

Conclusions and Future Work

6.1 Conclusions

Presently, electric motors, such as induction motors (IMs), permanent magnet synchronous motors (PMSMs) and switched reluctance motors (SRM), sustain the development of modern industry. These electric motors have their strengths and weaknesses respectively. It is still promising to propose novel and enhanced electric motors by using different but effective principles. Moreover, machine control methods are essential to make full use of electric motors and drive circuits, to achieve satisfactory control performance. Therefore, this thesis devises a new coreless and magnetless electric motor, and explores machine control methods to enhance the steady and dynamic response of speed. More specifically, the primary contributions and conclusions of this thesis are summarized as follows:

i) Magnetic Resonant Coupling Motor

This thesis firstly presents a novel magnetic resonant coupling motor (MRCM) constructed without any ferrous or permanent magnet core. As an elementary and essential part of the proposed MRCM, a pole pair is analyzed elaborately in terms of the selection of resonant topology, the force magnitude and direction, and the frequency splitting phenomenon. Besides, the underlying operation principle has been developed from the perspective of a pole pair. Following the proposed design procedures, the feasibility of the proposed MRCM is fully validated using computer simulations in MATLAB, PSIM and ANSYS Maxwell. A rough comparison with the conventional induction motor

was provided to further highlight the relative merits of the proposed MRCM. Simulation results obtained so far are stimulating and the proposed MRCM could well be a promising start for a new generation of future electric motor. Further research shall focus on the optimization of the motor structure and pole ratio as well as the realization of sophisticated position tracking and frequency control. Furthermore, it is possible to enhance the proposed MRCM by employing suitable cores material with high permeability.

ii) Single-Vector-Based MPDSC with Compensation Factors for PMSM Drives

A single-vector-based MPDSC with compensation factors has been proposed and developed, and the effectiveness of the proposed MPDSC strategy has been verified by simulations and HIL experiments. The proposed MPDSC strategy eliminated the PI unit, presenting an excellent speed tracking capability with very small speed offset. To reduce the manufacturing cost, an on-line load torque observer is firstly developed to track the variation of load torque. Then, a torque suppression factor is incorporated into the cost function to suppress large torque oscillations and overshoots during the start-up, speed-down and speed-up. Besides, the myopic prediction is introduced and analyzed. The correction of myopic prediction can enhance both the dynamic and steady state response, especially at low sampling frequency. Comparison study shows that the proposed MPDSC strategy has an overall better performance than the conventional DTC. Simulations and HIL experiments have verified the feasibility and effectiveness of the proposed MPDSC strategy.

iii) *Duty-Ratio-Based MPDSC with Two Cost Functions for PMSM Drives*

A duty-ratio-based MPDSC with two cost functions has been proposed to enhance the control performance in terms of speed offset, speed ripple and torque ripple. The feasibility and superiority of the proposed MPDSC has been well validated by MATLAB simulations and HIL tests. Eight duty ratios are integrated with eight voltage vectors to form eight combinations of voltage

vectors. An optimal combination of voltage vectors is selected through two cost functions acting sequentially. Comprehensive comparison proves that the proposed method performs an excellent control performance: the THD, the torque ripple, the speed ripple, and the speed offset are 4.43%, 0.0423Nm, 0.0121rpm and 0.0055% respectively. It can be affirmed that this strategy performs better performance than classical DTC and the MPDSC presented in Chapter IV, during steady state as well as transient operation.

6.2 Future Work

The fundamental theory of the proposed MRCM has been illustrated in this report, and effective MPDSC methods have been devised to achieve a better control performance on speed. Nevertheless, the current research could be further consolidated with the incorporation of the following research orientations in the future.

For MRCM:

The proposed MRCM is a new concept of electric motor constructed without any plastic or permanent magnet cores. Besides the advantages presented before, the proposed MRCM has its disadvantages, which are illustrated as follows.

(1) Many mathematical expressions of the proposed MRCM are still needed to be supplemented and perfected: an accurate mathematical expression for electromagnetic torque of proposed MRCM; and an exact mathematical expression of splitting frequencies deduced with the consideration of the resistance.

(2) The proposed MRCM utilizes the reinforced plastic as the core and shaft material. The permeability of the reinforced plastic is around 1, which cannot enhance the torque. It is possible to select the high permeability material as the core to achieve the enhancement of the force. Particular attention should be paid on the selection of magnetic properties to reduce

eddy loss and hysteresis loss in high excitation frequency. If cores with high permeability are used, it is essential to design the magnetic path of proposed MRCM. However, as the force is developed in an elementary pole pair, the mutual inductance among adjacent stator or rotor poles should be suppressed to guarantee the effective and efficient force generation in a pole pair. It is possible to shield the undesired mutual inductance by using some shielding materials. Future research may devise a novel configuration to enhance the MRCM with high permeability cores.

(3) The control of the proposed MRCM is very demanding, since the excitation frequency has to be varied corresponding to the different angular displacement. To perform a good performance in terms of efficiency and output torque, it is essential to design a suitable and advanced control strategy, as well as to redesign a motor structure to ease the requirement on control.

(4) Due to the coreless and magnetless design, the efficiency is not very high. Over the whole design process, it did not take the efficiency into consideration. To enhance the efficiency, well-design control strategy and motor structure are required, after the use of cores with high permeability.

(5) It is possible to make the proposed MRCM in a smaller size for the application which requires a very small rotating force. In this case, it may not need the varying excitation frequency, but fixed lower and higher frequencies (comparing to the natural resonant frequency) to generate attraction and repulsion forces. However, the excitation frequencies could be up to mega, or even giga hertz, which is a critical challenge considering the manufacture cost and control device.

For MPDSC:

The proposed MPDSC is a PI-free control strategy, where no PI adapters are employed in the whole control logic. The error of the control is corrected by the

cost function and suppressed by compensation factors. However, there are still many aspects are required to be enhanced:

(1) Although the MPC has gained remarkable research progress, the challenge of strong dependence on system model still needs to be addressed. Most MPC methods, including the proposed MPDSC methods, depend on an accurate mathematical model of the controlled system, to achieve precise parameter estimation for the compensation of one step delay, and to achieve an effective and satisfactory control. Some methods have been proposed to enhance MPC's robustness against parameter variation. Using observers is an effective method to mitigate the parameter dependence. However, the observer is to estimate certain parameters, an observer model has to include some machine parameters. Moreover, the stability of observers should be ensured through carefully pole assignment. Apart from observers, some model-free MPC methods can be used to avoid using model parameters [117, 167, 168]. These methods utilize measured currents to implement the prediction of future machine behavior, in which the dependence of MPC on model parameter is transferred to the dependence on the accuracy of the current measurement. Therefore, the first future research orientation is to tackle the problem of parameter dependence in MPC, with satisfactory control performance on speed, torque and current. Model-free MPC could be a research hotspot to enhance the robustness of MPDSC.

(2) Although MPC is a straightforward control algorithm to cope with multiple objective and nonlinearity, it requires heavier computation burden than DTC and FOC. Additionally, after the integration of multiple step prediction and multiple coordinate conversion, the computational burden of MPC algorithm would increase exponentially. Moreover, when multiple voltage vectors are employed in one control period, like the duty-ratio-based MPDSC in Chapter V, duty ratio should be calculated by some

criterions. This process would demand a long time calculation. Consequently, MPCs with heavy computation burden have to operate in powerful digital microprocessors, which increase the cost of control system. As is shown in Fig. 4.25 and 5.13, the proposed MPDSC methods spend more time in running the control code than DTC and MPC. Some methods to reduce the complexity of MPDSC algorithm shall be investigated in the future.

(3) MPC methods select the optimal voltage vector or the combination of voltage vector through the cost function. The cost function usually consists of a few control variables, whose units are in different magnitude. A weighting factor is therefore used to balance the weight of different control variables. Tuning the weighting factor through trial and error method, to achieve a satisfactory control performance is a tedious time consuming task. In order to eliminate the impact of weighting factor on the control performance, [110] proposes a method to use a flux-ripple-related variable weighting factor to replace the tuning process. In order to eliminate the impact of weighting factor on the control performance, [111] evaluates the electromagnetic torque and stator flux separately, and select the optimal voltage vector based on a ranking approach. A voltage vector is derived to replace the electromagnetic torque and stator flux in [112] to eliminate the weighting factor. In [114-116], the torque and stator flux are converted to an equivalent vector of the stator flux to avoid the use of weighting factor. It is demanding to eliminate the use of weighting factor, and more simple and effective method could be proposed in the future research.

(4) As the main control objective of MPDSC is to reduce the ripple and offset on speed, the control performance on torque is not optimized. An offset on torque can be observed in the simulation and HIL test results. Such torque offset could result from the inaccuracy of the discrete-time parameter prediction, or some inappropriate configuration in the proposed MPDSC.

More investigation should be conducted to deal with the torque offset in the future research.

Reference

[1] Z. Q. Zhu and D. Howe, "Electrical machines and drives for electric, hybrid, and fuel cell vehicles," *Proc. IEEE,* vol. 95, no. 4, pp. 746-765, Apr. 2007.

[2] H. C. Stanley, "An analysis of the induction machine," *Transactions of the American Institute of Electrical Engineers,* vol. 57, no. 12, pp. 751-757, May 1938.

[3] F. W. Merrill, "Permanent magnet excited synchronous motors," *Electrical Engineering,* vol. 74, no. 2, pp. 143-143, Feb. 1955.

[4] P. J. Lawrenson, J. M. Stephenson, P. T. Blenkinsop, J. Corda, and N. N. Fulton, "Variable-speed switched reluctance motors," *IEE PROC-B,* vol. 127, no. 4, pp. 253-265, Jul. 1980.

[5] W. Zhao, K. T. Chau, M. Cheng, J. Ji, and X. Zhu, "Remedial Brushless AC Operation of Fault-Tolerant Doubly Salient Permanent-Magnet Motor Drives," *IEEE Trans. Ind. Electron.,* vol. 57, no. 6, pp. 2134-2141, Jun. 2010.

[6] Y. Du, C. Zhang, X. Zhu, F. Xiao, Y. Sun, Y. Zuo, *et al.*, "Principle and Analysis of Doubly Salient PM Motor With Π-Shaped Stator Iron Core Segments," *IEEE Trans. Ind. Electron.*, vol. 66, no. 3, pp. 1962-1972, Mar. 2019.

[7] H. Yang, H. Lin, Z. Q. Zhu, S. Lyu, and Y. Liu, "Design and Analysis of Novel Asymmetric-Stator-Pole Flux Reversal PM Machine," *IEEE Trans. Ind. Electron.*, vol. 67, no. 1, pp. 101-114, Jan. 2020.

[8] P. Su, W. Hua, M. Hu, Z. Chen, M. Cheng, and W. Wang, "Analysis of PM Eddy Current Loss in Rotor-PM and Stator-PM Flux-switching Machines by Air-gap Field Modulation Theory," *IEEE Trans. Ind. Electron.*, vol. 67, no. 3, pp. 1824-1835, Mar. 2020.

[9] E. Bostanci, M. Moallem, A. Parsapour, and B. Fahimi, "Opportunities and challenges of switched reluctance motor drives for electric propulsion: a comparative study," *IEEE Trans. Transport. Electrific.*, vol. 3, no. 1, pp. 58-75, Mar. 2017.

[10] K. Vijayakumar, R. Karthikeyan, S. Paramasivam, R. Arumugam, and K. N. Srinivas, "Switched reluctance motor modeling, design, simulation, and analysis: a comprehensive review," *IEEE Trans. Magn.*, vol. 44, no. 12, pp. 4605-4617, Dec. 2008.

[11] J. Liu, K. W. Chan, C. Y. Chung, N. H. L. Chan, M. Liu, and W. Xu, "Single-stage wireless-power-transfer resonant converter with boost bridgeless power-factor-correction rectifier," *IEEE Trans. Ind. Electron.*, vol. 65, no. 3, pp. 2145-2155, Mar. 2018.

[12] Y. Li, R. Mai, L. Lu, T. Lin, Y. Liu, and Z. He, "Analysis and transmitter currents decomposition based control for multiple overlapped transmitters based WPT systems considering cross couplings," *IEEE Trans. Power Electron.*, vol. 33, no. 2, pp. 1829-1842, Feb. 2018.

[13] Y. Li, R. Mai, L. Lu, and Z. He, "Active and reactive currents decomposition-based control of angle and magnitude of current for a parallel multiinverter IPT system," *IEEE Trans. Power Electron.*, vol. 32, no. 2, pp. 1602-1614, Feb. 2017.

[14] N. Tesla, "Apparatus for transmitting electrical energy," ed. U.S. Patent 1119732 A, May 1907.

[15] A. Kurs, A. Karalis, R. Moffatt, J. D. Joannopoulos, P. Fisher, and M. Soljačić, "Wireless power transfer via strongly coupled magnetic resonances," *Sci. Express,* vol. 317, no. 5834, pp. 83-86, Jun. 2007.

[16] W. Shi, J. Deng, Z. Wang, and X. Cheng, "The start-up dynamic analysis and one cycle control-PD control combined strategy for primary-side controlled wireless power transfer system," *IEEE Access*, vol. 6, pp. 14439-14450, Mar. 2018.

[17] Y. Tang, Y. Chen, U. K. Madawala, D. J. Thrimawithana, and H. Ma, "A new controller for bidirectional wireless power transfer systems," *IEEE Trans. Power Electron.,* vol. 33, no. 10, pp. 9076-9087, Dec. 2017.

[18] C. Cheng, Z. Zhou, W. Li, C. Zhu, Z. Deng, and C. C. Mi, "A multi-load wireless power transfer system with series-parallel-series compensation," *IEEE Trans. Power Electron.,* vol. 34, no. 8, pp. 7126-7130, Jan. 2019.

[19] Y. Zhang, T. Kan, Z. Yan, and C. C. Mi, "Frequency and voltage tuning of series–series compensated wireless power transfer system to sustain rated power under various conditions," *IEEE J. Emerg. Sel. Top. Power Electron.,* vol. 7, no. 2, pp. 1311-1317, Sep. 2019.

[20] T. A. Khan, A. Yazdan, and R. W. Heath, "Optimization of Power Transfer Efficiency and Energy Efficiency for Wireless-Powered Systems With Massive MIMO," *IEEE Transactions on Wireless Communications*, vol. 17, no. 11, pp. 7159-7172, Nov. 2018.

[21] T. Orekan, P. Zhang, and C. Shih, "Analysis, design, and maximum power-efficiency tracking for undersea wireless power transfer," *IEEE J. Emerg. Sel. Top. Power Electron.*, vol. 6, no. 2, pp. 843-854, Jun. 2018.

[22] W. Zhong and S. Y. R. Hui, "Maximum energy efficiency operation of series-series resonant wireless power transfer systems using on-off keying modulation," *IEEE Trans. Power Electron.*, vol. 33, no. 4, pp. 3595-3603, May 2017.

[23] Y. Li, J. Hu, X. Li, R. Mai, Z. Li, M. Liu, *et al.*, "Efficiency analysis and optimization control for input-parallel output-series wireless power transfer systems," *IEEE Trans. Power Electron.*, pp. 1-1, May 2019.

[24] Q. Deng, J. Liu, D. Czarkowski, W. Hu, and H. Zhou, "An inductive power transfer system supplied by a multiphase parallel inverter," *IEEE Trans. Ind. Electron.*, vol. 64, no. 9, pp. 7039-7048, Sep. 2017.

[25] X. Li, J. Hu, Y. Li, H. Wang, M. Liu, and P. Deng, "A decoupled power and data parallel transmission method with four-quadrant misalignment tolerance for wireless power transfer systems," *IEEE Trans. Power Electron.*, pp. 1-1, Jun. 2019.

[26] X. Li, C. Tang, X. Dai, P. Deng, and Y. Su, "An inductive and capacitive combined parallel transmission of power and data for wireless power transfer systems," *IEEE Trans. Power Electron.*, vol. 33, no. 6, pp. 4980-4991, Jun. 2018.

[27] P. Si, A. P. Hu, S. Malpas, and D. Budgett, "A frequency control method for regulating wireless power to implantable devices," *IEEE Trans. Biomed. Circuits Syst.*, vol. 2, no. 1, pp. 22-29, Mar. 2008.

[28] K. Agarwal, R. Jegadeesan, Y. X. Guo, and N. V. Thakor, "Wireless power transfer strategies for implantable bioelectronics," *IEEE Rev. Biomed. Eng.*, vol. 10, pp. 136-161, Mar. 2017.

[29] D. Ahn and S. Hong, "Wireless power transmission with self-regulated output voltage for biomedical implant," *IEEE Trans. Ind. Electron.*, vol. 61, no. 5, pp. 2225-2235, Oct. 2014.

[30] K. W. Klontz, D. M. Divan, D. W. Novotny, and R. D. Lorenz, "Contactless power delivery system for mining applications," *IEEE Trans. Ind. Appl.*, vol. 31, no. 1, pp. 27-35, Jan./Feb. 1995.

[31] H. B. J. Kuipers, S. Bakker, and H. Rijnaarts, "Near field resonant inductive coupling to power electronic devices dispersed in water," *Sens. Actuators A, Phys.,*, vol. 178, pp. 217–222, May 2012.

[32] J. Y. Lee and B. M. Han, "A bidirectional wireless power transfer EV charger using self-Resonant PWM," *IEEE Trans. Power Electron.*, vol. 30, no. 4, pp. 1784-1787, Apr. 2015.

[33] D. H. Tran, V. B. Vu, and W. Choi, "Design of a high-efficiency wireless power transfer system with intermediate coils for the on-board chargers of electric vehicles," *IEEE Trans. Power Electron.*, vol. 33, no. 1, pp. 175-187, Jan. 2018.

[34] Y. Nagatsuka, N. Ehara, Y. Kaneko, S. Abe, and T. Yasuda, "Compact contactless power transfer system for electric vehicles," in *Proc. Int. Power Electron. Conf., Sapporo, Japan*, 2010, pp. 807-813.

[35] W. Zhang, S. Wong, C. K. Tse, and Q. Chen, "Analysis and comparison of secondary series- and parallel-compensated inductive power transfer systems operating for optimal efficiency and load-independent voltage-

transfer ratio," *IEEE Trans. Power Electron.*, vol. 29, no. 6, pp. 2979-2990, Jun. 2014.

[36] X. Qu, H. Han, S. Wong, C. K. Tse, and W. Chen, "Hybrid IPT topologies with constant current or constant voltage output for battery charging applications," *IEEE Trans. Power Electron.*, vol. 30, no. 11, pp. 6329-6337, Nov. 2015.

[37] R. Mai, Y. Chen, Y. Li, Y. Zhang, G. Cao, and Z. He, "Inductive power transfer for massive electric bicycles charging based on hybrid topology switching with a single inverter," *IEEE Trans. Power Electron.*, vol. 32, no. 8, pp. 5897-5906, Aug. 2017.

[38] Y. Li, J. Hu, M. Liu, Y. Chen, K. W. Chan, Z. He, *et al.*, "Reconfigurable intermediate resonant circuit based WPT system with load-independent constant output current and voltage for charging battery," *IEEE Trans. Power Electron.*, vol. 34, no. 3, pp. 1988-1992, Mar. 2019.

[39] W. Chwei-Sen, G. A. Covic, and O. H. Stielau, "Power transfer capability and bifurcation phenomena of loosely coupled inductive power transfer systems," *IEEE Trans. Ind. Electron.*, vol. 51, no. 1, pp. 148-157, Feb. 2004.

[40] Y. Zhang and Z. Zhao, "Frequency splitting analysis of two-coil resonant wireless power transfer," *IEEE Antennas Wireless Propag. Lett.*, vol. 13, pp. 400-402, Mar. 2014.

[41] H. Runhong, Z. Bo, Q. Dongyuan, and Z. Yuqiu, "Frequency splitting phenomena of magnetic resonant coupling wireless power transfer," *IEEE Trans. Magn.*, vol. 50, no. 11, pp. 1-4, Nov. 2014.

[42] D. Ahn and S. Hong, "A study on magnetic field repeater in wireless power transfer," *IEEE Trans. Ind. Electron.*, vol. 60, no. 1, pp. 360-371, Sep. 2013.

[43] A. P. Sample, D. A. Meyer, and J. R. Smith, "Analysis, experimental results, and range adaptation of magnetically coupled resonators for wireless power transfer," *IEEE Trans. Ind. Electron.*, vol. 58, no. 2, pp. 544-554, Feb. 2011.

[44] Y. Zhang, Z. Zhao, and K. Chen, "Frequency-splitting analysis of four-coil resonant wireless power transfer," *IEEE Trans. Ind. Appl.*, vol. 50, no. 4, pp. 2436-2445, Aug. 2014.

[45] W. Q. Niu, J. X. Chu, W. Gu, and A. D. Shen, "Exact analysis of frequency splitting phenomena of contactless power transfer systems," *IEEE Trans. Circuits Syst. I, Reg. Papers*, vol. 60, no. 6, pp. 1670-1677, Jun. 2013.

[46] L. Hongchang, L. Jie, W. Kangping, C. Wenjie, and Y. Xu, "A maximum efficiency point tracking control scheme for wireless power transfer systems using magnetic resonant coupling," *IEEE Trans. Power Electron.*, vol. 30, no. 7, pp. 3998-4008, Jul. 2015.

[47] S. Huang, Z. Li, and K. Lu, "Frequency splitting suppression method for four-coil wireless power transfer system," *IET Power Electron.*, vol. 9, no. 15, pp. 2859-2864, Dec. 2016.

[48] Y. L. Lyu, F. Y. Meng, G. H. Yang, B. J. Che, Q. Wu, L. Sun, *et al.*, "A method of using nonidentical resonant coils for frequency splitting elimination in wireless power transfer," *IEEE Trans. Power Electron.*, vol. 30, no. 11, pp. 6097-6107, Jul. 2015.

[49] H. Nguyen, J. I. Agbinya, and J. Devlin, "FPGA-based implementation of multiple modes in near field inductive communication using frequency splitting and MIMO configuration," *IEEE Trans. Circuits Syst. I, Reg. Papers,* vol. 62, no. 1, pp. 302-310, Jan. 2015.

[50] J. Kim, G. Wei, M. Kim, H. Ryo, P. Ri, and C. Zhu, "A splitting frequencies-based wireless power and information simultaneous transfer method," *IEEE Trans. Circuits Syst. I, Reg. Papers,* vol. 65, no. 12, pp. 4434-4445, Dec. 2018.

[51] R. Narayanamoorthi, A. V. Juliet, and B. Chokkalingam, "Frequency splitting-based wireless power transfer and simultaneous propulsion generation to multiple micro-robots," *IEEE Sensors Journal,* vol. 18, no. 13, pp. 5566-5575, Jul. 2018.

[52] F. Blaschke, "The principle of field orientation as applied to the new transvector closed-loop system for rotating-field machines," *Siemens Rev.,* vol. 34, no. 3, pp. 217-220, May 1972.

[53] A. Pal, S. Das, and A. K. Chattopadhyay, "An improved rotor flux space vector based MRAS for field-oriented control of induction motor drives," *IEEE Trans. Power Electron.,* vol. 33, no. 6, pp. 5131-5141, Jun. 2018.

[54] G. Jo and J. Choi, "Gopinath model-based voltage model flux observer design for field-oriented control of induction motors," *IEEE Trans. Power Electron.,* pp. 1-1, May 2018.

[55] M. Tousizadeh, H. S. Che, J. Selvaraj, N. A. Rahim, and B. T. Ooi, "Fault-tolerant field oriented control of three-phase induction motor based on unified feed-forward method," *IEEE Trans. Power Electron.*, pp. 1-1, Nov. 2018.

[56] I. Takahashi and T. Noguchi, "A new quick-response and high-efficiency control strategy of an induction motor," *IEEE Trans. Ind. Appl.,* vol. IA-22, no. 5, pp. 820-827, Sep./Oct. 1986.

[57] M. Depenbrock, "Direct self-control (DSC) of inverter-fed induction machine," *IEEE Trans. Power Electron.,* vol. 3, no. 4, pp. 420-429, Oct. 1988.

[58] G. S. Buja and M. P. Kazmierkowski, "Direct torque control of PWM inverter-fed AC motors - a survey," *IEEE Trans. Ind. Electron.,* vol. 51, no. 4, pp. 744-757, Aug. 2004.

[59] L. Zhong, M. F. Rahman, W. Y. Hu, and K. W. Lim, "Analysis of direct torque control in permanent magnet synchronous motor drives," *IEEE Trans. Power Electron.,* vol. 12, no. 3, pp. 528-536, May 1997.

[60] L. Zhong, M. F. Rahman, W. Y. Hu, K. W. Lim, and M. A. Rahman, "A direct torque controller for permanent magnet synchronous motor drives," *IEEE Trans. Energy Convers.,* vol. 14, no. 3, pp. 637-642, Sep. 1999.

[61] A. A. Naassani, E. Monmasson, and J. Louis, "Synthesis of direct torque and rotor flux control algorithms by means of sliding-mode theory," *IEEE Transactions on Industrial Electronics,* vol. 52, no. 3, pp. 785-799, 2005.

[62] L. Joong-Hui, K. Chang-Gyun, and Y. Myung-Joong, "A dead-beat type digital controller for the direct torque control of an induction motor," *IEEE Trans. Power Electron.,* vol. 17, no. 5, pp. 739-746, Sep. 2002.

[63] T. Lixin, Z. Limin, M. F. Rahman, and Y. Hu, "A novel direct torque controlled interior permanent magnet synchronous machine drive with low ripple in flux and torque and fixed switching frequency," *IEEE Transactions on Power Electronics,* vol. 19, no. 2, pp. 346-354, 2004.

[64] Z. Yongchang, Z. Zhengming, L. Ting, and Y. Liqiang, "Sensorless 3-level inverter-fed induction motor drive based on indirect torque control," in *in Proc. IEEE 6th Int. Power Electron. Motion Control Conf.*, 2009, pp. 589-593.

[65] T. G. Habetler, F. Profumo, M. Pastorelli, and L. M. Tolbert, "Direct torque control of induction machines using space vector modulation," *IEEE Trans. Ind. Appl.*, vol. 28, no. 5, pp. 1045-1053, Oct. 1992.

[66] B. H. Kenny and R. D. Lorenz, "Stator- and rotor-flux-based deadbeat direct torque control of induction machines," *IEEE Trans. Ind. Appl.*, vol. 39, no. 4, pp. 1093-1101, Jul./Aug. 2003.

[67] L. Yen-Shin and C. Jian-Ho, "A new approach to direct torque control of induction motor drives for constant inverter switching frequency and torque ripple reduction," *IEEE Trans. Energy Convers.*, vol. 16, no. 3, pp. 220-227, Sep. 2001.

[68] C. Lascu and A. M. Trzynadlowski, "Combining the principles of sliding mode, direct torque control, and space-vector modulation in a high-performance sensorless AC drive," *IEEE Trans. Ind. Appl.*, vol. 40, no. 1, pp. 170-177, Jan./Feb. 2004.

[69] Y. Zhang, J. Zhu, W. Xu, J. Hu, D. G. Dorrell, and Z. Zhao, "Speed sensorless stator flux oriented control of three-level inverter-fed induction motor drive based on fuzzy logic and sliding mode control," in *in Proc. 36th IEEE IECON*, 2010, pp. 2932-2937.

[70] F. Niu, K. Li, and Y. Wang, "Direct torque control for permanent-magnet synchronous machines based on duty ratio modulation," *IEEE Trans. Ind. Electron.*, vol. 62, no. 10, pp. 6160-6170, Oct. 2015.

[71] Y. Zhang and J. Zhu, "Direct torque control of permanent magnet synchronous motor with reduced torque ripple and commutation frequency," *IEEE Trans. Power Electron.*, vol. 26, no. 1, pp. 235-248, Jan. 2011.

[72] K. Jun-Koo and S. Seung-Ki, "New direct torque control of induction motor for minimum torque ripple and constant switching frequency," *IEEE Trans. Ind. Appl.*, vol. 35, no. 5, pp. 1076-1082, Sep./Oct. 1999.

[73] K. Shyu, J. Lin, V. Pham, M. Yang, and T. Wang, "Global minimum torque ripple design for direct torque control of induction motor drives," *IEEE Trans. Ind. Electron.*, vol. 57, no. 9, pp. 3148-3156, Sep. 2010.

[74] F. Niu, B. Wang, A. S. Babel, K. Li, and E. G. Strangas, "Comparative evaluation of direct torque control strategies for permanent magnet synchronous machines," *IEEE Trans. Power Electron.*, vol. 31, no. 2, pp. 1408-1424, Feb. 2016.

[75] M. Pacas and J. Weber, "Predictive direct torque control for the PM synchronous machine," *IEEE Transactions on Industrial Electronics*, vol. 52, no. 5, pp. 1350-1356, 2005.

[76] E. Flach, R. Hoffmann, and P. Mutschler, "Direct mean torque control of an induction motor," in *Proc. EPE*, 1997, pp. 3.672-3.677.

[77] L. Kyo-Beum, S. Joong-Ho, C. Ick, and Y. Ji-Yoon, "Torque ripple reduction in DTC of induction motor driven by three-level inverter with low switching frequency," *IEEE Trans. Power Electron.*, vol. 17, no. 2, pp. 255-264, Mar. 2002.

[78] Y. Zhang and J. Zhu, "A novel duty cycle control strategy to reduce both torque and flux ripples for DTC of permanent magnet synchronous motor

drives with switching frequency reduction," *IEEE Trans. Power Electron.*, vol. 26, no. 10, pp. 3055-3067, Oct. 2011.

[79] M. A. M. Cheema, J. E. Fletcher, D. Xiao, and M. F. Rahman, "A direct thrust control scheme for linear permanent magnet synchronous motor based on online duty ratio control," *IEEE Trans. Power Electron.*, vol. 31, no. 6, pp. 4416-4428, Jun. 2016.

[80] Z. Zhang and X. Liu, "A duty ratio control strategy to reduce both torque and flux ripples of DTC for permanent magnet synchronous machines," *IEEE Access*, vol. 7, pp. 11820-11828, Jan. 2019.

[81] L. Romeral, A. Arias, E. Aldabas, and M. G. Jayne, "Novel direct torque control (DTC) scheme with fuzzy adaptive torque-ripple reduction," *IEEE Trans. Ind. Electron.*, vol. 50, no. 3, pp. 487-492, Jun. 2003.

[82] H. Chaoui, M. Khayamy, and A. A. Aljarboua, "Adaptive interval type-2 fuzzy logic control for PMSM drives with a modified reference frame," *IEEE Trans. Ind. Electron.*, vol. 64, no. 5, pp. 3786-3797, May 2017.

[83] G. Feng, C. Lai, and N. C. Kar, "A closed-loop fuzzy-logic-based current controller for PMSM torque ripple minimization using the magnitude of speed harmonic as the feedback control signal," *IEEE Trans. Ind. Electron.*, vol. 64, no. 4, pp. 2642-2653, Apr. 2017.

[84] D. Flieller, N. K. Nguyen, P. Wira, G. Sturtzer, D. O. Abdeslam, and J. Merckl é, "A self-learning solution for torque ripple reduction for nonsinusoidal permanent-magnet motor drives based on artificial neural networks," *IEEE Trans. Ind. Electron.*, vol. 61, no. 2, pp. 655-666, Feb. 2014.

[85] J. Yu, P. Shi, W. Dong, B. Chen, and C. Lin, "Neural network-based adaptive dynamic surface control for permanent magnet synchronous motors," *IEEE Trans. Neural Netw. Learn. Syst.*, vol. 26, no. 3, pp. 640-645, Mar. 2015.

[86] J. Liu, H. Li, and Y. Deng, "Torque ripple minimization of PMSM based on robust ILC via adaptive sliding mode control," *IEEE Trans. Power Electron.*, vol. 33, no. 4, pp. 3655-3671, Apr. 2018.

[87] V. Repecho, D. Biel, and A. Arias, "Fixed switching period discrete-time sliding mode current control of a PMSM," *IEEE Trans. Ind. Electron.*, vol. 65, no. 3, pp. 2039-2048, Mar. 2018.

[88] X. Zhang, L. Sun, K. Zhao, and L. Sun, "Nonlinear speed control for PMSM system using sliding-mode control and disturbance compensation techniques," *IEEE Trans. Power Electron.*, vol. 28, no. 3, pp. 1358-1365, Mar. 2013.

[89] J. R. Domínguez, A. Navarrete, M. A. Meza, A. G. Loukianov, and J. Cañedo, "Digital sliding-mode sensorless control for surface-mounted PMSM," *IEEE Trans. Ind. Informat.*, vol. 10, no. 1, pp. 137-151, Feb. 2014.

[90] T. Geyer, G. Papafotiou, and M. Morari, "Model predictive direct torque control-part I: concept, algorithm, and analysis," *IEEE Trans. Ind. Electron.*, vol. 56, no. 6, pp. 1894-1905, Jun. 2009.

[91] M. Preindl and S. Bolognani, "Model predictive direct torque control with finite control set for PMSM drive systems, part 1: maximum torque per ampere operation," *IEEE Trans. Ind. Informat.*, vol. 9, no. 4, pp. 1912-1921, Nov. 2013.

[92] M. Preindl and S. Bolognani, "Model predictive direct torque control with finite control set for PMSM drive systems, part 2: field weakening operation," *IEEE Trans. Ind. Informat.*, vol. 9, no. 2, pp. 648-657, May 2013.

[93] Y. Zhang and W. Xie, "Low complexity model predictive control-single vector-based approach," *IEEE Trans. Power Electron.*, vol. 29, no. 10, pp. 5532-5541, Oct. 2014.

[94] Y. Zhang, D. Xu, J. Liu, S. Gao, and W. Xu, "Performance improvement of model-predictive current control of permanent magnet synchronous motor drives," *IEEE Trans. Ind. Appl.*, vol. 53, no. 4, pp. 3683-3695, Aug. 2017.

[95] M. Yang, X. Lang, J. Long, and D. Xu, "Flux immunity robust predictive current control with incremental model and extended state observer for PMSM drive," *IEEE Trans. Power Electron.*, vol. 32, no. 12, pp. 9267-9279, Dec. 2017.

[96] M. Siami, D. A. Khaburi, and J. Rodriguez, "Simplified finite control set-model predictive control for matrix converter-fed PMSM drives," *IEEE Trans. Power Electron.*, vol. 33, no. 3, pp. 2438-2446, Mar. 2018.

[97] S. Kouro, P. Cortes, R. Vargas, U. Ammann, and J. Rodriguez, "Model predictive control—a simple and powerful method to control power converters," *IEEE Trans. Ind. Electron.*, vol. 56, no. 6, pp. 1826-1838, Jun. 2009.

[98] Y. Shan, J. Hu, Z. Li, and J. M. Guerrero, "A model predictive control for renewable energy based AC microgrids without any PID regulators," *IEEE Trans. Power Electron.*, vol. 33, no. 11, pp. 9122-9126, Nov. 2018.

[99] P. Falkowski and A. Sikorski, "Finite control set model predictive control for grid-connected AC–DC converters with LCL filter," *IEEE Trans. Ind. Electron.,* vol. 65, no. 4, pp. 2844-2852, Apr. 2018.

[100] Y. Zhang, Y. Peng, and H. Yang, "Performance improvement of two-vectors-based model predictive control of PWM rectifier," *IEEE Trans. Power Electron.,* vol. 31, no. 8, pp. 6016-6030, Aug. 2016.

[101] O. Sandre-Hernandez, J. Rangel-Magdaleno, and R. Morales-Caporal, "A Comparison on Finite-Set Model Predictive Torque Control Schemes for PMSMs," *IEEE Trans. Power Electron.,* vol. 33, no. 10, pp. 8838-8847, Oct. 2018.

[102] Y. Wang, X. Wang, W. Xie, F. Wang, M. Dou, R. M. Kennel, *et al.*, "Deadbeat model-predictive torque control with discrete space-vector modulation for PMSM drives," *IEEE Trans. Ind. Electron.,* vol. 64, no. 5, pp. 3537-3547, May 2017.

[103] T. Geyer, "Algebraic tuning guidelines for model predictive torque and flux control," *IEEE Trans. Ind. Appl.,* vol. 54, no. 5, pp. 4464-4475, Sep./Oct. 2018.

[104] P. Karamanakos and T. Geyer, "Model predictive torque and flux control minimizing current distortions," *IEEE Trans. Power Electron.,* vol. 34, no. 3, pp. 2007-2012, Mar. 2019.

[105] Y. Zhang and H. Yang, "Model predictive torque control of induction motor drives with optimal duty cycle control," *IEEE Trans. Power Electron.,* vol. 29, no. 12, pp. 6593-6603, Dec. 2014.

[106] W. Xie, X. Wang, F. Wang, W. Xu, R. M. Kennel, D. Gerling, *et al.*, "Finite-control-set model predictive torque control with a deadbeat solution

for PMSM drives," *IEEE Trans. Ind. Electron.*, vol. 62, no. 9, pp. 5402-5410, Sep. 2015.

[107] F. Wang, S. A. Davari, Z. Chen, Z. Zhang, D. A. Khaburi, J. Rodr ́guez, *et al.*, "Finite control set model predictive torque control of induction machine with a robust adaptive observer," *IEEE Trans. Ind. Electron.*, vol. 64, no. 4, pp. 2631-2641, Apr. 2017.

[108] M. Liu, J. Hu, and K. W. Chan, "Improved model predictive control of permanent magnet synchronous motor with duty ratio optimization and cost function correction," in *Int. Conf. Electr. Mach. Syst.*, Oct. 2017, pp. 1-5.

[109] P. R. U. Guazzelli, W. C. d. A. Pereira, C. M. R. d. Oliveira, A. G. d. Castro, and M. L. d. Aguiar, "Weighting factors optimization of predictive torque control of induction motor by multiobjective genetic algorithm," *IEEE Trans. Power Electron.*, vol. 34, no. 7, pp. 6628-6638, Jul. 2019.

[110] W. Xu, J. Zou, Y. Liu, and J. Zhu, "Weighting Factor Less Model Predictive Thrust Control for Linear Induction Machine," *IEEE Trans. Power Electron.*, pp. 1-1, Jan. 2019.

[111] C. A. Rojas, J. Rodriguez, F. Villarroel, J. R. Espinoza, C. A. Silva, and M. Trincado, "Predictive torque and flux control without weighting factors," *IEEE Trans. Ind. Electron.*, vol. 60, no. 2, pp. 681-690, Feb. 2013.

[112] X. Zhang and B. Hou, "Double vectors model predictive torque control without weighting factor based on voltage tracking error," *IEEE Trans. Power Electron.*, vol. 33, no. 3, pp. 2368-2380, Mar. 2018.

[113] R. E. K. Meesala, V. P. K. Kunisetti, and V. K. Thippiripati, "Enhanced predictive torque control for open end winding induction motor drive

without weighting factor assignment," *IEEE Trans. Power Electron.*, vol. 34, no. 1, pp. 503-513, Jan. 2019.

[114] X. Wu, W. Song, and C. Xue, "Low-complexity model predictive torque control method without weighting factor for five-phase PMSM based on hysteresis comparators," *IEEE Trans. Emerg. Sel. Topics Power Electron.*, vol. 6, no. 4, pp. 1650-1661, Dec. 2018.

[115] Y. Zhang and H. Yang, "Two-vector-based model predictive torque control without weighting factors for induction motor drives," *IEEE Trans. Power Electron.*, vol. 31, no. 2, pp. 1381-1390, Feb. 2016.

[116] Y. Zhang and H. Yang, "Model-predictive flux control of induction motor drives with switching instant optimization," *IEEE Trans. Energy Convers.*, vol. 30, no. 3, pp. 1113-1122, Sep. 2015.

[117] C. Lin, J. Yu, Y. Lai, and H. Yu, "Improved model-free predictive current control for synchronous reluctance motor drives," *IEEE Trans. Ind. Electron.*, vol. 63, no. 6, pp. 3942-3953, Jun. 2016.

[118] X. Zhang, L. Zhang, and Y. Zhang, "Model predictive current control for PMSM drives with parameter robustness improvement," *IEEE Trans. Power Electron.*, vol. 34, no. 2, pp. 1645-1657, Feb. 2019.

[119] R. S. Dastjerdi, M. A. Abbasian, H. Saghafi, and M. H. Vafaie, "Performance improvement of permanent-magnet synchronous motor using a new deadbeat-direct current controller," *IEEE Trans. Power Electron.*, vol. 34, no. 4, pp. 3530-3543, Apr. 2019.

[120] D. Su, C. Zhang, and Y. Dong, "Finite-state model predictive current control for surface-mounted permanent magnet synchronous motors based on current locus," *IEEE Access*, vol. 5, pp. 27366-27375, Dec. 2017.

[121] Y. Zhou, H. Li, R. Liu, and J. Mao, "Continuous voltage vector model-free predictive current control of surface mounted permanent magnet synchronous motor," *IEEE Trans. Energy Convers.*, vol. 34, no. 2, pp. 899-908, Aug. 2019.

[122] F. Morel, X. Lin-Shi, J. M. Retif, B. Allard, and C. Buttay, "A Comparative Study of Predictive Current Control Schemes for a Permanent-Magnet Synchronous Machine Drive," *IEEE Trans. Ind. Electron.*, vol. 56, no. 7, pp. 2715-2728, Jul. 2009.

[123] S. A. Davari, D. A. Khaburi, and R. Kennel, "An improved fcs–mpc algorithm for an induction motor with an imposed optimized weighting factor," *IEEE Trans. Power Electron.*, vol. 27, no. 3, pp. 1540-1551, Mar. 2012.

[124] Y. Zhang, G. Suyu, and L. Jiali, "An improved model predictive control for permanent magnet synchronous motor drives," in *in Proc. IEEE 8th Int. Power Electron. Motion Control Conf.*, 2016, pp. 1877-1883.

[125] Y. Zhang, D. Xu, and L. Huang, "Generalized multiple-vector-based model predictive control for PMSM drives," *IEEE Trans. Ind. Electron.*, vol. 65, no. 12, pp. 9356-9366, Dec. 2018.

[126] C. Zhang, G. Wu, F. Rong, J. Feng, L. Jia, J. He, *et al.*, "Robust fault-tolerant predictive current control for permanent magnet synchronous motors considering demagnetization fault," *IEEE Trans. Ind. Electron.*, vol. 65, no. 7, pp. 5324-5334, Jul. 2018.

[127] M. Sato, G. Yamamoto, D. Gunji, T. Imura, and H. Fujimoto, "Development of wireless in-wheel motor using magnetic resonance

coupling," *IEEE Trans. Power Electron.,* vol. 31, no. 7, pp. 5270-5278, Jul. 2016.

[128] A. Abdolkhani, A. P. Hu, and N. K. C. Nair, "A double stator through-hole type contactless slipring for rotary wireless power transfer applications," *IEEE Trans. Energy Convers.,* vol. 29, no. 2, pp. 426-434, Jun. 2014.

[129] A. Abdolkhani and A. P. Hu, "A contactless slipring system based on axially traveling magnetic field," *IEEE Trans. Emerg. Sel. Topics Power Electron.,* vol. 3, no. 1, pp. 280-287, Mar. 2015.

[130] A. Abdolkhani, A. P. Hu, G. A. Covic, and M. Moridnejad, "Through-hole contactless slipring system based on rotating magnetic field for rotary applications," *IEEE Trans. Ind. Appl.,* vol. 50, no. 6, pp. 3644-3655, Nov./Dec. 2014.

[131] K. Song, B. Ma, G. Yang, J. Jiang, R. Wei, H. Zhang, *et al.*, "A rotation-lightweight wireless power transfer system for solar wing driving," *IEEE Trans. Power Electron.,* vol. 34, no. 9, pp. 8816-8830, Sep. 2019.

[132] M. Y. Li, X. Y. Chen, Q. Huang, G. N. Bai, J. H. Liang, and L. N. Wang, "Conceptual design and characteristic analysis of a rotary-type superconducting wireless power transfer system using ReBCO primary at 50 Hz," *IEEE Trans. Appl. Supercond.,* vol. 29, no. 2, pp. 1-5, Mar. 2019.

[133] P. Kakosimos and H. Abu-Rub, "Deadbeat predictive control for PMSM drives with 3-L NPC inverter accounting for saturation effects," *IEEE Trans. Emerg. Sel. Topics Power Electron.,* vol. 6, no. 4, pp. 1671-1680, Dec. 2018.

[134] Y. Luo and C. Liu, "A simplified model predictive control for a dual three-phase PMSM with reduced harmonic currents," *IEEE Trans. Ind. Electron.*, vol. 65, no. 11, pp. 9079-9089, Nov. 2018.

[135] Y. Luo and C. Liu, "A flux constrained predictive control for a six-phase PMSM motor with lower complexity," *IEEE Trans. Ind. Electron.*, vol. 66, no. 7, pp. 5081-5093, Jul. 2019.

[136] C. Sun, D. Sun, Z. Zheng, and H. Nian, "Simplified model predictive control for dual inverter-fed open-winding permanent magnet synchronous motor," *IEEE Trans. Energy Convers.*, vol. 33, no. 4, pp. 1846-1854, Dec. 2018.

[137] Z. Zhou, C. Xia, Y. Yan, Z. Wang, and T. Shi, "Disturbances attenuation of permanent magnet synchronous motor drives using cascaded predictive-integral-resonant controllers," *IEEE Trans. Power Electron.*, vol. 33, no. 2, pp. 1514-1527, Feb. 2018.

[138] M. Preindl and S. Bolognani, "Model predictive direct speed control with finite control set of PMSM drive systems," *IEEE Trans. Power Electron.*, vol. 28, no. 2, pp. 1007-1015, Feb. 2013.

[139] V. Šmídl, J. Š, L. Adam, and Z. Peroutka, "Direct speed control of a PMSM drive using SDRE and convex constrained optimization," *IEEE Trans. Ind. Electron.*, vol. 65, no. 1, pp. 532-542, Jan. 2018.

[140] P. Kakosimos and H. Abu-Rub, "Predictive speed control with short prediction horizon for permanent magnet synchronous motor drives," *IEEE Trans. Power Electron.*, vol. 33, no. 3, pp. 2740-2750, Mar. 2018.

[141] Z. Zhou, C. Xia, Y. Yan, Z. Wang, and T. Shi, "Torque ripple minimization of predictive torque control for PMSM with extended control set," *IEEE Trans. Ind. Electron.,* vol. 64, no. 9, pp. 6930-6939, Sep. 2017.

[142] T. Wang, C. Liu, G. Lei, Y. Guo, and J. Zhu, "Model predictive direct torque control of permanent magnet synchronous motors with extended set of voltage space vectors," *IET Electr. Power App.,* vol. 11, no. 8, pp. 1376-1382, Jun. 2017.

[143] Y. Zhang, Y. Bai, and H. Yang, "A universal multiple-vector-based model predictive vontrol of induction motor drives," *IEEE Trans. Power Electron.,* vol. 33, no. 8, pp. 6957-6969, Aug. 2018.

[144] M. R. Nikzad, B. Asaei, and S. O. Ahmadi, "Discrete duty-cycle-control method for direct torque control of induction motor drives with model predictive solution," *IEEE Trans. Power Electron.,* vol. 33, no. 3, pp. 2317-2329, Mar. 2018.

[145] L. Yan, M. Dou, Z. Hua, H. Zhang, and J. Yang, "Optimal duty cycle model predictive current control of high-altitude ventilator induction motor with extended minimum stator current operation," *IEEE Trans. Power Electron.,* vol. 33, no. 8, pp. 7240-7251, Aug. 2018.

[146] Y. Zhang, J. Liu, G. Yuan, Z. Li, and H. Lou, "An improved model predictive control with duty cycle control for PMSM drives," in *Proc. Int. Conf. Elect. Mach. (ICEM)*, Nov. 2016, pp. 1-5.

[147] X. Zhang, B. Hou, and Y. Mei, "Deadbeat predictive current control of permanent-magnet synchronous motors with stator current and disturbance observer," *IEEE Trans. Power Electron.,* vol. 32, no. 5, pp. 3818-3834, May 2017.

[148] G. Li, J. Hu, Y. Li, and J. Zhu, "An improved model predictive direct torque control strategy for reducing harmonic currents and torque ripples of five-phase permanent magnet synchronous motors," *IEEE Trans. Ind. Electron.,* vol. 66, no. 8, pp. 5820-5829, Aug. 2019.

[149] M. Norambuena, J. Rodriguez, Z. Zhang, F. Wang, C. Garcia, and R. Kennel, "A very simple strategy for high-quality performance of AC machines using model predictive control," *IEEE Trans. Power Electron.,* vol. 34, no. 1, pp. 794-800, Jan. 2019.

[150] M. Onsal, Y. Demir, and M. Aydin, "A new nine-phase permanent magnet synchronous motor with consequent pole rotor for high-power traction applications," *IEEE Trans. Magn.,* vol. 53, no. 11, pp. 1-6, Nov. 2017.

[151] Y. Burkhardt, A. Spagnolo, P. Lucas, M. Zavesky, and P. Brockerhoff, "Design and analysis of a highly integrated 9-phase drivetrain for EV applications," in *Proc. Int. Conf. Elect. Mach. (ICEM)*, Sep. 2014, pp. 450-456.

[152] L. Zhang, Y. Fan, C. Li, and C. Liu, "Design and analysis of a new six-phase fault-tolerant hybrid-excitation motor for electric vehicles," *IEEE Trans. Magn.,* vol. 51, no. 11, pp. 1-4, Nov. 2015.

[153] L. Zhang, Y. Fan, R. D. Lorenz, R. Cui, C. Li, and M. Cheng, "Design and analysis of a new five-phase brushless hybrid-excitation fault-tolerant motor for electric vehicles," *IEEE Trans. Ind. Appl.,* vol. 53, no. 4, pp. 3428-3437, Jul./Aug. 2017.

[154] X. Zhu, X. Wang, C. Zhang, L. Wang, and W. Wu, "Design and analysis of a spoke-type hybrid permanent magnet motor for electric vehicles," *IEEE Trans. Magn.,* vol. 53, no. 11, pp. 1-4, Nov. 2017.

[155] K. Kiyota and A. Chiba, "Design of switched reluctance motor competitive to 60-kW IPMSM in third-generation hybrid electric vehicle," *IEEE Trans. Ind. Appl.*, vol. 48, no. 6, pp. 2303-2309, Nov./Dec. 2012.

[156] J. Zhu, K. W. E. Cheng, X. Xue, and Y. Zou, "Design of a new enhanced torque in-wheel switched reluctance motor with divided teeth for electric vehicles," *IEEE Trans. Magn.*, vol. 53, no. 11, pp. 1-4, Nov. 2017.

[157] P. Andrada, B. Blanqué, E. Martínez, and M. Torrent, "A novel type of hybrid reluctance motor drive," *IEEE Trans. Ind. Electron.*, vol. 61, no. 8, pp. 4337-4345, Aug. 2014.

[158] A. Dalal and P. Kumar, "Design, prototyping, and testing of a dual-rotor motor for electric vehicle application," *IEEE Trans. Ind. Electron.*, vol. 65, no. 9, pp. 7185-7192, Sep. 2018.

[159] A. Kurs, A. Karalis, R. Moffatt, J. D. Joannopoulos, P. Fisher, and M. Soljačić, "Wireless power transfer via strongly coupled magnetic resonances," *science*, vol. 317, no. 5834, pp. 83-86, Jul. 2007.

[160] R. Jegadeesan and Y. X. Guo, "Topology selection and efficiency improvement of inductive power links," *IEEE Trans. Antennas Propag.*, vol. 60, no. 10, pp. 4846-4854, Oct. 2012.

[161] Y. Shan, J. Hu, K. W. Chan, Q. Fu, and J. M. Guerrero, "Model predictive control of bidirectional DC-DC converters and AC/DC interlinking converters - a new control method for PV-wind-battery microgrids," *IEEE Trans. Sustain. Energy*, pp. 1-1, to be published. DOI: 10.1109/TSTE.2018.2873390.

[162] K. Ogata, *Modern control engineering*: Chapter 10: Control system design in state space, Pearon Education (US), 5th edition, 2009.

[163] T. Diekhans and R. W. D. Doncker, "A dual-side controlled inductive power transfer system optimized for large coupling factor variations and partial load," *IEEE Trans. Power Electron.*, vol. 30, no. 11, pp. 6320-6328, Nov. 2015.

[164] Y. C. Hsieh, Z. R. Lin, M. C. Chen, H. C. Hsieh, Y. C. Liu, and H. J. Chiu, "High-efficiency wireless power transfer system for electric vehicle applications," *IEEE Trans. Circuits Syst. II, Exp. Briefs*, vol. 64, no. 8, pp. 942-946, Aug. 2017.

[165] C. Zheng, J. Zhang, W. Liu, N. Zhang, and W. Hua, "A novel reduced-order load torque observer based discrete-time sliding mode control for PMSM speed servo system," in *Proc. ICEMS*, Sydney, AUS, 2017, pp. 1-6.

[166] M. Liu, K. W. Chan, J. Hu, W. Xu, and J. Rodriguez, "Model predictive direct speed control with torque oscillation reduction for pmsm drives," *IEEE Trans. Ind. Informat.*, to be published. DOI: 10.1109/TII.2019.2898004, [Online].

[167] C. K. Lin, T. H. Liu, J. t. Yu, L. C. Fu, and C. F. Hsiao, "Model-free predictive current control for interior permanent-magnet synchronous motor drives based on current difference detection technique," *IEEE Trans. Ind. Electron.*, vol. 61, no. 2, pp. 667-681, Feb. 2014.

[168] P. G. Carlet, F. Tinazzi, S. Bolognani, and M. Zigliotto, "An effective model-free predictive current control for synchronous reluctance motor drives," *IEEE Trans. Ind. Appl.*, vol. 55, no. 4, pp. 3781-3790, Apr. 2019.